

University of New Hampshire

University of New Hampshire Scholars' Repository

Master's Theses and Capstones

Student Scholarship

Fall 2021

Graphene Transistor-Based Printable Electronics for Wearable Biosensing Applications

Kaitlyn Laliberte

University of New Hampshire, Durham

Follow this and additional works at: <https://scholars.unh.edu/thesis>

Recommended Citation

Laliberte, Kaitlyn, "Graphene Transistor-Based Printable Electronics for Wearable Biosensing Applications" (2021). *Master's Theses and Capstones*. 1513.

<https://scholars.unh.edu/thesis/1513>

This Thesis is brought to you for free and open access by the Student Scholarship at University of New Hampshire Scholars' Repository. It has been accepted for inclusion in Master's Theses and Capstones by an authorized administrator of University of New Hampshire Scholars' Repository. For more information, please contact Scholarly.Communication@unh.edu.

**GRAPHENE TRANSISTOR-BASED PRINTABLE ELECTRONICS FOR WEARABLE
BIOSENSING APPLICATIONS**

By

Kaitlyn Emma Laliberte

BS Electrical and Computer Engineering, University of New Hampshire 2020

THESIS

Submitted to the University of New Hampshire
in Partial Fulfillment of
the Requirements of the Degree of

Master of Science
in
Electrical and Computer Engineering

September 2021

This thesis has been examined and approved in partial fulfillment of the requirements for the degree of Master of Science in Electrical and Computer Engineering by:

Edward Song, Assistant Professor in Electrical and Computer Engineering

MD Shaad Mahmud, Assistant Professor in Electrical and Computer Engineering

Diliang Chen, Assistant Professor in Electrical and Computer Engineering

On August 6th, 2021

Approval signatures are on file with the University of New Hampshire Graduate School.

ACKNOWLEDGEMENTS

I would like to acknowledge the University of New Hampshire and Professor Dr. Edward Song for the opportunity to work as a research assistant in the BioMEMS laboratory. Thank you, Dr. Song, for the guidance, advice, and direction that you provided throughout my time at the University of New Hampshire.

I would like to thank the University of New Hampshire Research Assistantship and the National Science Foundation (ECCS, Grant #: 1847152) and the NSF EPSCoR (Grant #: 175737) for funding my research while working in the BioMEMS laboratory. Thank you to all the fellow students who work in the BioMEMS laboratory for guidance, the University of Massachusetts Lowell for the silicon oxide coating substrates for my research, and Professor Dr. Md. Shaad Mahmud and his laboratory for developing the integrated current measurement system used in this research.

Thank you to my parents and family for the unconditional love and support during my time at the University of New Hampshire. Thank you to my better half, Cameron, for being by my side and encouraging me each day with love and positivity. My thesis is dedicated to my dad who is the greatest electrical engineer I have ever met and motivates me to always try my best.

TABLE OF CONTENTS

ACKNOWLEDGEMENTS	iii
LIST OF TABLES	vi
LIST OF FIGURES	vii
LIST OF ABBREVIATIONS	x
ABSTRACT	xii
CHAPTER 1: INTRODUCTION.....	1
1.1. OVERVIEW.....	1
1.2. GFET AS A BIOSENSOR.....	2
1.3. MOTIVATION.....	2
1.4. THESIS OBJECTIVES	3
1.5. THESIS OUTLINE	4
CHAPTER 2: THEORETICAL BACKGROUND	5
2.1. OVERVIEW.....	5
2.2. BIOSENSORS.....	5
2.3. GRAPHENE.....	7
2.4. GRAPHENE-BASED FIELD-EFFECT TRANSISOR.....	10
2.5. INTERLEUKIN-6	12
2.6. SENSING CONCEPTS.....	13
2.6.1. LIQUID-GATED FET	14
2.6.2. APTAMER-BASED SENSING.....	14
2.6.3. FUNCTIONALIZATION	16
2.6.4. DEBYE LENGTH.....	16
2.6.5. DIRAC VOLTAGE.....	17
CHAPTER 3: MATERIALS AND METHODS	22
3.1. OVERVIEW.....	22
3.2. DEVICE FABRICATION.....	22
3.2.1. KICAD	22
3.2.2. VOLTERA V-ONE PCB PRINTER.....	24

3.2.3. PRINTING RELIABILITY.....	25
3.2.4. EASY TRANSFER GRAPHENE.....	26
CHAPTER 4: CHARACTERIZING GFET.....	30
4.1. OVERVIEW.....	30
4.2. REQUIRED MATERIALS.....	30
4.3. SILICON OXIDE COATING.....	31
4.4. SUBSTRATE SELECTION.....	33
4.5. INK CHOICE.....	37
4.6. MECHANICAL STRESS.....	40
4.7. GFET FUNCTIONALIZATION.....	42
CHAPTER 5: DETECTING BIOMARKER.....	45
5.1. OVERVIEW.....	45
5.2. SENSING THEORY.....	45
5.3. STATIC SENSING.....	46
5.3.1. BUFFER LIQUID GATE VS ANALYTE LIQUID GATE.....	49
5.3.2. SELECTIVITY AND LIMIT OF DETECTION.....	51
5.3.3. SENSING UNDER MECHANICAL STRESS.....	54
5.4. REAL-TIME SENSING.....	57
5.5. IMPLEMENTATION OF INTEGRATED CURRENT MEASUREMENT PLATFORM.....	61
5.6. CHARACTERIZATION TECHNIQUES AND MEASUREMENT SETUP.....	64
CHAPTER 6: CONCLUSION.....	66
FUTURE WORK.....	66
REFERENCES.....	70
APPENDIX.....	77

LIST OF TABLES

Table 3.1: Summary of labels for final GFET device.	23
Table 3.2: Electrode widths and distances tested in KiCAD design and printed with Voltera.	26
Table 5.1: Average shift in Dirac voltage for IL-6 static sensing with $0.01 \times$ PBS as liquid gate and $V_{DS} = 100$ mV.	48
Table 5.2: Average shift in Dirac voltage for TNF- α selectivity static sensing with $0.01 \times$ PBS as liquid gate and $V_{DS} = 100$ mV.	52

LIST OF FIGURES

Figure 2.1: (A) Schematic of GFET device on an SiO ₂ coated Si substrate (back-gated); (B) Zero-bandgap structure of graphene resulting in an ambipolar characteristic curve. Reproduced from [42].	9
Figure 2.2: Iterative SELEX method and process of aptamer selection. Reproduced from [53].	15
Figure 2.3: V-shaped transfer characteristic curve (I_D vs V_{GS}) with Dirac voltage before and after target binding.	18
Figure 2.4: (A) Schematic of electrolyte liquid-gated GFET (top-gated); (B) Electrostatic gating effect demonstrated with capacitors formed at the graphene-solution and gate-solution interfaces. Reproduced from [42].	19
Figure 2.5: Charge transfer doping effect demonstrated in GFET. Reproduced from [42].	20
Figure 3.1: Final KiCAD design featuring 7 electrodes; electrodes 1 – 6 as drain/source and electrode 7 as gate with line width 350 μ m and line spacing 250 μ m edge to edge.	23
Figure 3.2: Voltera V-One PCB printer used for rapid fabrication of GFET electrodes.	24
Figure 3.3: Voltera V-One printer settings options	25
Figure 3.4: 1 cm \times 1 cm easy transfer monolayer graphene from Graphenea on a polymer film.	27
Figure 3.5: Graphene transfer process using fishing technique. Reproduced from [5].	28
Figure 3.6: (A) Fabrication steps for the GFET device; (B) Voltera V-ONE printed graphene-based FET on Si/SiO ₂ wafer using KiCAD design. Easy transfer monolayer graphene transferred across drain and source electrodes.	29
Figure 4.1: SiO ₂ coating impacts on (a) device transfer characteristic curve; (b) device transconductance in both the hole and electron branches; (c,d) surface morphology of bare substrate and 50 nm SiO ₂ coated substrate. Reproduced from [6] with permission from the Royal Society of Chemistry.	32
Figure 4.2: Transfer characteristic curve of GFET device fabricated on (a) Kapton substrate with 50 nm SiO ₂ coating versus bare Kapton film; (b) SiO ₂ coating provides consistency to transfer characteristic curve measurements.	33
Figure 4.3: Flexible film substrates (A) Kapton substrate; and (B) Mylar substrate.	34

Figure 4.4: Polydimethylsiloxane (PDMS) polymer substrate.....	35
Figure 4.5: Transfer characteristic curve with $V_{DS} = 100\text{mV}$ for Si/SiO ₂ wafer (baseline), SiO ₂ coated Mylar, SiO ₂ coated Kapton, and SiO ₂ coated PDMS.	36
Figure 4.6: KiCAD stretchability file containing ten 1 mm wide traces.....	38
Figure 4.7: Dycotec stretchable silver conductive ink versus Voltera Flex silver conductive ink.	39
Figure 4.8: GFET design with all parameters finalized. Substrate: 50 nm SiO ₂ coated Kapton; Ink: Dycotec flexible and stretchable silver conductive ink.	40
Figure 4.9: (A) Transfer characteristic curve of GFET on flat substrate and bent around radii of 1.5 cm, 2.25 cm, and 4.25 cm; (B) Change in Dirac voltage with respect to the bending radius of the substrate. Error bars created with $N = 5$ devices.	41
Figure 4.10: Transfer characteristic curves during functionalization displaying p-type doping after introduction of PBASE and n-type doping after introduction of aptamers.	43
Figure 4.11: IL-6 sensing process performed on Kapton GFET without PBASE and aptamers. (A) GFET transfer characteristic curves with $V_{DS} = 50\text{ mV}$; (B) The corresponding calibration curve.	44
Figure 5.1: Conceptual drawing detailing how protein introduction impacts the sensor behavior, specifically the transfer characteristic curve and resulting Dirac voltage.	45
Figure 5.2: IL-6 static sensing with $0.01 \times \text{PBS}$ as liquid gate and $V_{DS} = 100\text{ mV}$. (A) Normalized transfer characteristic curves showing a right shift in Dirac voltage with respect to concentration; (B) Concentration calibration curve showing the changes in Dirac voltage as a function of concentration with resulting Hill-Langmuir line of best fit ($R^2 = 99.27\%$).	47
Figure 5.3: IL-6 static sensing with analyte as liquid gate and $V_{DS} = 10\text{ mV}$. (A) Normalized transfer characteristic curves showing a right shift in Dirac voltage with respect to concentration; (B) Concentration calibration curve showing change in Dirac voltage as a function of concentration with resulting Hill-Langmuir line of best fit ($R^2 = 98.37\%$).	50
Figure 5.4: (A) IL-6 calibration curve showing change in Dirac voltage as a function of concentration. The black represents experimental data points where there the graphene is rinsed before sensing (liquid gate: $0.01 \times \text{PBS}$ buffer) and the purple represents experimental data points where there the graphene is not rinsed before sensing (liquid gate: specified concentration of IL-6 solution); (B) Side by side comparison of rinse (buffer liquid gate) versus no rinse (analyte liquid gate) shift in Dirac voltage as a function of concentration.....	50
Figure 5.5: TNF- α selectivity static sensing with $0.01 \times \text{PBS}$ as liquid gate and $V_{DS} = 100\text{ mV}$. (A) Normalized transfer characteristic curves showing concentration independent change in Dirac	

voltage; (B) Calibration curve showing IL-6 change in Dirac voltage as a function of concentration with resulting Hill-Langmuir line of best fit and TNF- α change in Dirac voltage as a function of concentration.52

Figure 5.6: (A) k-GFET IL-6 static sensing results while substrate is bent at radius of 2.25 cm and $V_{DS} = 10$ mV; (B) Normalized transfer characteristic curves showing a right shift in Dirac voltage with respect to concentration; (C) Concentration calibration curve showing change in Dirac voltage as a function of concentration.55

Figure 5.7: (A) Calibration curve with IL-6 sensing done with k-GFET on flat substrate (purple) and on bent substrate (orange); (B) Side by side comparison of flat versus bending shift in Dirac voltage as a function of concentration.56

Figure 5.8: Microfluidic channel used in real-time sensing with dimensions of 600 μ M width and 100 μ M height.58

Figure 5.9: Ideal I_{DS} versus time graph with increasing protein concentration injections.59

Figure 5.10: Real-time measurements. (A) I_{DS} versus time with various IL-6 injections; (B) Change in I_{DS} with respect to concentration.60

Figure 5.11: The k-GFET sensor shown with the integrated current measurement platform developed by Prof. Md Shaad Mahmud's group.61

Figure 5.12: Comparison of integrated microcontroller measurements versus external current meter. (A) I_{DS} versus V_{GS} transfer characteristic curve; (B) Dirac voltage location with $N = 3$ reps per device.63

Figure 6.1: Full sweep from LabVIEW showing full backward sweep and two-part forward sweep.68

LIST OF ABBREVIATIONS

AFE	analog front end
CAD	computer aided design
CVD	chemical vapor deposition
DMF	dimethyl formamide
EDL	electrical double layer
FET	field-effect transistor
GFET	graphene field-effect transistor
I_{DS}	drain-to-source current
I_G	gate current
IL-6	Interleukin-6
k-GFET	GFET fabricated on Kapton substrate
K_d	dissociation constant
K_d^{-1}	Debye length
LoD	limit of detection
$MgCl_2$	magnesium chloride
NHS	N-hydroxysuccinimide
PBASE	1-pyrenebutyric acid N-hydroxy succinimide ester
PBS	phosphate buffered saline
PCB	printed circuit board
PDMS	polydimethylsiloxane
pDNA	probe deoxyribonucleic acid

PNA	peptide nucleic acid
POCT	point-of-care testing
QCM	quartz crystal microbalance
SELEX	systematic evolution of ligands by exponential enrichment
SiO ₂	silicon oxide
TNF- α	tumor necrosis factor alpha
V _{DS}	drain-to-source voltage
V _{DIRAC}	Dirac voltage
V _{GS}	gate-to-source voltage

ABSTRACT

Graphene field-effect transistor (GFET) is becoming an increasingly popular biosensing platform for monitoring health conditions through biomarker detection. Moreover, the graphene's 2-dimensional geometry makes it ideal for implementing flexible or wearable electronic devices. By using a GFET platform as a biosensor, users can easily monitor numerous health conditions. A sweat-based biosensor can non-invasively monitor levels of proteins in the body and alert the user to possible issues such as a steep increase or decrease in a particular protein. By creating a platform that can be used as a wearable biosensor, it allows for rapid results and a cheaper way to provide clinical quality data about one's health conditions.

This thesis presents a novel approach for creating a low cost, reliable and selective, wearable biosensor for real-time observation and tracking of the levels of the protein biomarker Interleukin-6 (IL-6). A printable graphene transistor-based biosensor is created by using a PCB printer on a flexible Kapton substrate. The conductive channel of the GFET is created using a chemical vapor deposition (CVD)-grown graphene layer. By functionalizing (or modifying) the graphene surface with biorecognition elements such as antibodies or aptamers in the channel of the device, the GFET can operate as a biosensor. When various levels of IL-6 were introduced into the GFET device, the target proteins bind to the aptamers causing a change in the charge carrier concentration. The device is able to monitor in real-time the levels of IL-6 by observing the drain-to-source current of the GFET which correlates to the IL-6 concentration being measured. The device implemented contains an integrated current meter which is one of the building blocks for creating a wearable electronic biosensor.

CHAPTER 1: INTRODUCTION

1.1. OVERVIEW

The development of cheaper, more reliable, and rapid-result biosensors and devices cover a wide range of research topics in the health and bioelectronics fields. There are many types of biosensors including optical, electrochemical, electrical, piezoelectric, thermal and Field-Effect Transistor (FET)-based sensors. While each of these sensors have benefits and drawbacks, the FET-based biosensors are growing more popular as they offer many advantages such as highly sensitive measurements, portable instrumentation, easy operation, and low cost [6], [28], [40], [54]. More specifically, Graphene-based FETs have proven to make highly effective biosensors with extremely high sensitivity, flexibility, and rapid results. Graphene is a two-dimensional material, as it is a single atomic layer of graphite, which lends itself to being highly mechanically flexible, [37]-[38], [54] which is beneficial in terms of creating a wearable biosensor.

The fabrication of a wearable device creates many requirements to be met in terms of mechanical characteristics as well as the standard electrical characteristics necessary for a biosensor. Beginning with the substrate, the device must be bendable and able to conform to the skin; however, it should be rigid enough not to tear while still allowing for full mobility. These requirements have created the need for further investigation into electrode fabrication. The electrodes must be easily integrated with a variety of substrates during the fabrication process. The electrodes must also be bendable as they will be affixed to the substrate. After fabricating the electrodes on the selected substrate, the GFET also must meet a plethora of sensing requirements in order to successfully operate as a biosensor. The GFET will have to be able to detect a biomarker, which in this application will be the protein Interleukin-6 (IL-6). In addition, the device

must show a concentration-dependent response to the IL-6, otherwise there is no correlation between the device and biomarker. The device must also be selective to our target biomolecule exclusively while not responsive to other possible interfering species. Finally, the biosensor must be able to operate in real-time as a wearable device that is portable and gives both rapid and reliable detection results.

1.2. GFET AS A BIOSENSOR

Graphene-based FETs are highly advantageous for creating simple yet reliable biosensors and thus are increasing in popularity as a sensing platform. Graphene-based FETs have been used in a wide variety of sensing applications for an assortment of biomarkers. For example, GFETs have been used to detect proteins [4], [6], [80-83], DNAs [1], glucose [54], etc. GFETs function as biosensors effectively because biomarker and protein levels are able to be tracked through the device characteristics. By using GFET platforms as biosensors, point-of-care testing (POCT), which is highly sought-after, can be accomplished. POCT is when medical care is provided in more patient-g geared locations such as their homes or even bedside as opposed to a medical facility [8], [9]. POCT requires devices that provide sophisticated results and accuracy while being low cost, simple to operate, and that reduce the time to obtain the results [13]. Moreover, GFETs have proven to provide a platform that can do just that and therefore are a competitive option for POCT applications.

1.3. MOTIVATION

Many people around the globe suffer from diseases and sicknesses which need to be closely monitored and often tracked continuously in order to keep them under control. The pandemic that people are dealing with world-wide right now is just one of many examples of how important fast and reliable testing and detection of an illness can be. At the moment, certain tests can take days

for patients to receive results and COVID-19 can spread incredibly quickly. Therefore, in order to contain the spread of the virus, rapid and trustworthy testing is needed. Diseases such as tuberculosis, which is the leading infectious disease killer in the world, further demonstrate the need for rapid and reliable detection of disease biomarkers. According to the CDC, in 2018, ten million people suffered from tuberculosis but over three million of those cases went undiagnosed [14]. Breast cancer is yet another life-threatening disease that requires early-action testing and diagnosis for effective treatment. Early detection of breast cancer has proven to allow for increased available treatment options, increased survival, and improved quality of life [15]. While there are currently individual tests that detect each of these different diseases, it is necessary to further increase the reliability, speed, and accessibility to testing of all diseases.

Biosensors are becoming an increasingly popular device to be used in order to help monitor, track, and treat a plethora of diseases, sicknesses, and conditions. GFET sensors can be produced for low cost, meaning they can be mass produced and thus could become widely available as a new way to monitor one's health. In addition, sensors mounted on the skin have the ability to provide quality data to the user about a wide variety of biomarkers without the patient ever having to visit a doctor's office. Thus, in the future, GFET devices could be used as low cost, rapid, wearable biosensors that will allow for the user to have more flexibility in their day-to-day life, all while knowing that any conditions they may have are continuously being monitored.

1.4. THESIS OBJECTIVES

The goal of this thesis is to develop an in-house PCB printed graphene-based field-effect transistor biosensor with high sensitivity for Interleukin-6. The transistor is to be used as a wearable device and thus it should be flexible as well as be a stand-alone device. The specific objectives of this work are the following:

1. Develop a printable graphene field-effect transistor (GFET)-based biosensor on a flexible platform.
2. Demonstrate the detection of a biomarker, specifically Interleukin-6 (IL-6), using the printable GFET-based platform modified with aptamers as target-binding receptors.
3. Characterize the limit of detection and selectivity of the graphene-based sensor.
4. Demonstrate the real-time detection of the biomarker.
5. Characterize the GFET transfer (current-voltage) characteristic curve while the substrate is under mechanical stress.
6. Implementation of an integrated current measurement system for the device characterizations (in collaboration with Prof. Md. Shaad Mahmud's group).

1.5. THESIS OUTLINE

Chapter 2 gives background information on biosensors and electrolyte-gated GFET devices. The chapter also details sensing principles such as Dirac voltage, Debye length, and functionalization and immobilization of the device using PBASE and aptamers respectively. Chapter 3 outlines the exact materials, methods and procedures that were followed during the research process. The fabrication of the flexible and printable GFET is detailed from printing to graphene deposition. Chapter 4 discusses the optimization of the device as well as the process of functionalizing the graphene surface to be used as a selective biosensor. Chapter 5 describes the detection of the target biomarker IL-6 with the GFET biosensor in both a static and real-time measurement mode. This chapter also analyzes the device in terms of selectivity and reliability under mechanical stress. Chapter 6 details the integration of an internal microcontroller that is used to measure and record the current responses. Chapter 7 provides the conclusion and future outlook of this research.

CHAPTER 2: THEORETICAL BACKGROUND

2.1. OVERVIEW

Biosensors and health monitors are used to observe biomarkers and conditions occurring in the body. Humans rely on health monitoring systems for a plethora of information including disease diagnosis and progression. Sensors that can be worn on the body and continuously monitor these conditions could provide earlier notice to the user that there are issues which need to be addressed. Sensors depend on sensitivity, reliability, and rapid timing to remain as a key system for monitoring. Graphene-based FET devices are known for supporting highly sensitive and reliable devices which is why their use for sensors is a wide topic of research. In this chapter, the basic working principle of a graphene FET, its application as a biosensing platform and the theoretical background on aptamer-based target recognition and detection are discussed.

2.2. BIOSENSORS

A biosensor is a device which monitors for biomarkers and health conditions. A biosensor can be defined as an analytical device that incorporates a biological material such as microorganism, antibody, cell receptor, etc. and interprets the biomarker quantity into a proportional, measurable signal [87]. Biosensors similar to the one used in this application utilize a biological element along with a physicochemical transducer which converts a bio-recognition event into a proportional electronic signal [25]. Furthermore, a biosensor is comprised of two main parts, a bioreceptor and a transducer [25]. The first portion of the sensor is the bioreceptor where the target biomolecule either interact or bind with a receptor causing physical changes in the structures of the bioreceptor [25]. The second portion of the sensor is the transducer which

characterizes the changes occurring physically and creates measurable signals that are proportional to the concentration of the target molecules bound to the receptors [25]. Biosensors come in many different forms including optical, thermal, piezoelectric, quartz crystal microbalance (QCM), and electrochemical [25]. The sensors are classified based on the transducer type that is being used in order to convert the target recognition event into a readable signal.

Current state of the art of graphene-based biosensors includes extensive work on rigid substrates and often using lithography, etching and lift-off techniques to fabricate such devices. Many research groups have presented working graphene-based electronics, specifically as nano sensors [4], [10], [82]. As the name suggests, nano sensors get their name from both their physical size and the quantities of targets they are able to detect [84]. Nano sensors' dimensions are typically in the nanometer range while their limit of detection can be in the nanomolar range or even lower [4], [10], [84]. These nano sensors have provided clear results supporting that they can accurately measure changes in concentration of biomarkers such as proteins or DNA. In previous work, the FET is typically fabricated on a silicon oxide (SiO_2) coated silicon wafer substrate using standard nanofabrication techniques as mentioned above. Biosensors that detect DNAs or proteins are also widely used, where DNA sensing uses peptide nucleic acid (PNA) probes as the receptor to bind to the graphene and protein sensing uses specific aptamers [1], [4]. These devices show not only a range of targets that can be sensed, but also demonstrate the highly sensitive and selective nature of the GFET-based sensing platform.

In more recent work, the progression of GFETs on a variety of substrates has been at the forefront of development. Other techniques for fabrication have also been used such as inkjet printing [41]. By creating devices on bendable and stretchable substrates, it is more feasible to consider this platform for a wearable sensor in the future. Works on mylar are very common as it

is an extremely thin and transparent film which is a good choice for wearables. Mylar can also easily be mounted onto PDMS or adhesive tape allowing for a more stretchable design to be implemented [10], [40]. As a direct result of creating a device on a bendable substrate come challenges in terms of device inconsistencies upon several mechanical stresses such as bending, twisting, and stretching. These challenges are where the most recent field of research tends to focus.

This thesis is novel as it presents a fully printable GFET platform that is implemented as a wearable device. Currently, this printable platform is one of a kind as it is fabricated using 2D printed electronics through a PCB printer and silver conductive ink. The GFET is fabricated on a Dupont™ Kapton® flexible film using a conductive and stretchable silver ink (Dycotec Materials, Ltd., UK). The device has proven to have sensitive and selective results, can be 2D printed on a bendable substrate thus reducing cost and production time, and shows positive results under mechanical stresses. In addition to the advantages that this platform already offers, it can easily be integrated into wearable electronic devices for sensor input control and data acquisition.

2.3. GRAPHENE

Graphene has been at the forefront of research since 2004 when graphene was first isolated by Geim and Novoselov of University of Manchester, UK and has only become increasingly popular since their research was awarded a Nobel prize in 2010 [71], [72]. Graphene is a two-dimensional material of sp^2 hybridized carbon atoms in a hexagonal structure [72], [74]. Geim and Novoselov coined the term ‘Scotch Tape method’ as this was the method used to first discover the material [72]. As it is only a single atomic layer thick, it comes as no surprise that graphene is the thinnest material ever discovered [72]. Graphene is referred to as the building block for all graphitic carbon materials such as carbon nanotubes, graphite, and many others [72]. In addition

to being the building blocks of many materials, its carbon makeup also means that it conducts heat and electricity extremely well [73]. It is also the strongest material ever discovered, while at the same time the hardest and one of the most pliable [73]. After the ‘Scotch Tape method’ of discovering graphene, methods such as mechanical cleaving, chemical exfoliation, chemical synthesis, and thermal chemical vapor deposition were created in order to synthesize graphene [74].

Often referred to as a “wonder material”, graphene is a one-atom-thick layer of carbon atoms and is extremely diverse, making its possible applications wide-ranging. Graphene has many properties that make it advantageous for biosensing such as great conductivity, biocompatibility, and it is easy to functionalize [44]. Graphene is a versatile material with excellent properties, both mechanically and electrically, for creating a wearable biosensor. Graphene is made up of carbon atoms which are bonded tightly through in-plane σ bonds [26]. The bonds are created in a hexagonal shape and a network of delocalized electrons in the π -orbitals are responsible for graphene being electrically conductive among other features which make it a multipurpose material [26]. This particular network shape is responsible for the resulting electronic properties graphene possesses such as a zero-bandgap. Zero-bandgap structure means that at the charge neutrality point, holes and electrons can seamlessly be converted back and forth [42]. Thus, with zero-bandgap, the characteristic curve of graphene is continuous and ambipolar as shown in Figure 2.1(B). Figure 2.1(A) shows the V_{DS} applied to the device as well and the V_{GS} . The V_{GS} determines if current will flow between the source and drain terminals [85]. Figure 2.1(B) displays how the Fermi energy level relates to the V_{GS} . When the V_{GS} is lower than the Dirac voltage of the device, the Fermi energy level is in the conduction band and therefore the current is due to hole conduction [42]. Conversely, when the V_{GS} is greater than the Dirac voltage, the Fermi energy level is in the

valence band and therefore the current is due to electron conduction. At V_{GS} equal to the Dirac voltage, the device functions at the intrinsic Fermi level meaning that neither hole conduction nor electron conduction is dominant. Graphene also has an extremely high intrinsic carrier mobility and high conductivity which make it ideal for a conduction channel [2]. Graphene allows for the development of sensors with unprecedented sensitivity, fewer molecular defects, and superior conductivity [3]. Graphene-based electronics and FETs have proven to have high stability and electron mobility all while being relatively low cost to fabricate, thus making it highly in-demand for new electronics and sensors. A further, more extensive review of graphene's electrical properties is done in [43].

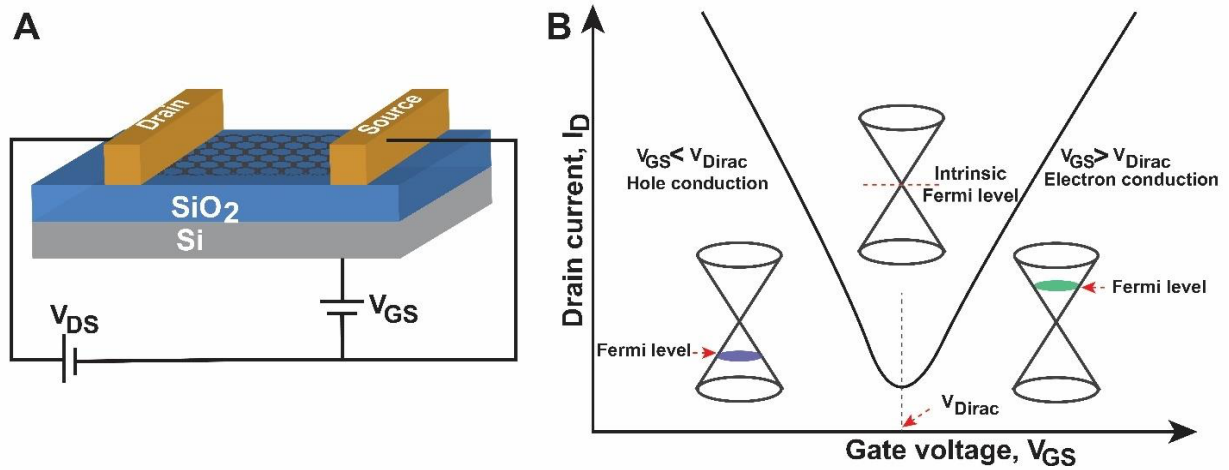


Figure 2.1: (A) Schematic of GFET device on an SiO₂ coated Si substrate (back-gated); (B) Zero-bandgap structure of graphene resulting in an ambipolar characteristic curve. Reproduced from [42].

In addition to a slew of valuable electrical properties, graphene also exhibits tremendous mechanical properties for creating a wearable biosensor. Graphene is one single atomic layer of graphite and therefore is a 2D, not 3D material. Graphene is the thinnest and strongest material ever discovered with an ultimate tensile strength of 130 gigapascals which is over 300 times stronger than structural steel [3]. Graphene is one atomic layer thick and therefore has unmatched mechanical flexibility along with optical transmittance [37], [38]. Graphene is the thinnest known

material which results in an extremely low bending stiffness as bending stiffness is proportional to the thickness cubed [57]. In addition to its two-dimensional structure being advantageous in terms of flexibility, it also lends itself to being extremely light weight at only 0.77 milligrams per square meter [3]. Graphene also has a Young's modulus of about 0.5 to 1 TPa, spring constant of about 1-5 N/M, and high material elasticity [2]. With such diverse electrical and mechanical properties, graphene is highly attractive for creating a biosensor.

2.4. GRAPHENE-BASED FIELD-EFFECT TRANSISOR

Field-effect transistors (FETs) are devices which utilize a source, gate, and drain terminal and use a conduction channel and electric field to control the flow of current in a device [28]. In graphene-based field-effect transistors (GFETs), graphene is used as the semimetal in the conduction channel. Graphene is a semimetal as opposed to a semiconductor because a semimetal is defined as a zero-bandgap semiconductor [86]. GFETs are considered an emerging technology in sensing applications because when a charged molecule adsorbs onto the graphene surface, it causes a change in the electric field which in turn causes a change in the gate potential of the device [42]. As a result, this causes a direct change in the channel conductance and subsequent change in the drain-source current [42]. This concept can be utilized to implement a sensor in which drain-source current changes proportionally to the amount of a particular molecule that is introduced and thus creating a GFET-based biosensor.

For a GFET, the conductive channel is created using graphene which is in contact with the drain and source electrodes, all of which is on an insulated substrate. The channel is then modified using a bioreceptor or specific modifier so that when the target proteins are introduced, the charge carriers in the conductive channel will be modulated due to the change in the electric field. An ionic buffer solution is then dropped onto the conductive graphene channel. When a gate-to-source

voltage (V_{GS}) is applied to the device, the electrical double layer (EDL) forms between the graphene channel and buffer solution [12]. The electrical double layer results in charges in the channel as well as a high gate capacitance which causes the electrostatic gating effect [42]. By altering the channel with outside biomolecules, there will be a change in the transfer characteristic curve, i.e., the drain-to-source current (I_{DS}) as a function of the gate-to-source voltage (V_{GS}) [29]. The transfer characteristic curve equation is given as follows [67]:

$$I_{DS} = \mu \frac{W}{L} C_{tot} V_D (V_G - V_{th})$$

Where μ is the carrier mobility, $\frac{W}{L}$ is the width to length ratio of the graphene conduction channel, and C_{tot} is the total gate capacitance of the dielectric. The gate capacitance is the total of the capacitance from the electrical double layer [68] as well as the quantum capacitance of the graphene [69]. V_D is the drain voltage, V_G is the gate voltage, and V_{th} is the threshold voltage. 1-pyrenebutyric acid N-hydroxy succinimide ester (PBASE) linkers are used to functionalize the graphene by permanently bonding to the surface through π -stacking and allow for other modifiers, such as aptamers, to be added which can interact with proteins [16]. Aptamer-based sensing is highly effective as aptamers have high affinity and selectivity for their targets [30]. Aptamers have proven to be successful in biosensing as they can bind to a variety of targets including proteins, peptides and amino acids [30]. Aptamers are immobilized onto the PBASE linkers and a droplet of liquid buffer is then placed across the drain, source, and gate electrodes. This electrolyte buffer is the medium through which the gate voltage is applied, thus this type of device architecture is called a liquid-gated GFET device. When the proteins are introduced to the system, they begin to interact with the aptamers. As the aptamers bind with the proteins, the aptamers are expected to undergo a significant conformation change [30]. Due to the changing shape of the aptamers and the proteins folding, there are measurable changes in I_{DS} which can be used as the sensor's readout.

2.5. INTERLEUKIN-6

Interleukin-6 (IL-6) is a pleiotropic cytokine that is produced in response to a plethora of processes including tissue damage, infections, cancer, and auto immune diseases [11], [45]. Interleukin-6 is also a biomarker for ailments such as collagen vascular disease, alcoholic cirrhosis, and kidney disease [19]. IL-6 is a protein which can be produced by both normal and harmful biological process. For instance, it is produced by the body during infections and kidney disease, but it is also produced by normal cell types that are involved in processes such as reproduction, metabolism, neural development, bone remodeling, and angiogenesis [46], [47]. Interleukin-6 is an important protein to sense and monitor as increased levels of IL-6 can require medical attention for many of the issues and illnesses listed above. Early detection of any one of these diseases or illnesses is key as it opens up the door for many more options during treatment.

Elevated levels of IL-6 have been linked to the severe acute respiratory syndrome coronavirus 2 (SARS-CoV-2). Contracting SARS-CoV-2 has proven to release a “cytokine storm” of hyper-inflammatory responses and causes the release of not only Interleukin-6, but Interleukin-1, Interleukin-8 and tumor necrosis factor alpha (TNF- α) [21]. Interleukin-6 levels are proven to increase with respect to disease stage for SARS-CoV-2 and directly relate to respiratory failure [21]. Furthermore, identification of IL-6 levels allowed for early identification of survivors versus non-survivors [21]. Additionally, IL-6 levels have proven to be lower for patients with SARS-CoV-2 who were in stage IIb and would soon recover into stage IIa in comparison with those who were in stage IIb and would progress further into stage III [21]. Moreover, the levels of Interleukin-6 in the body not only provide important information about the current state of an illness, but also the likely course that the illness or disease will take next.

IL-6 is a pro-inflammatory cytokine, meaning it is involved in processes where inflammation is present. Inflammation is a key sign of cancer growth and progression making it vital to keep track of and manage [11]. In 2014 it was reported that gastric cancer was the fourth most common cancer, with 951,000 cases and 723,000 resulting deaths [48]. High levels of IL-6 have been proven to lower the overall survival rate in patients with gastrointestinal (GI) cancer [11]. Studies have also proven that IL-6 can be used to estimate a patient's chance of recovery, reoccurrence of the disease, as well as a patient's response to therapy [49], [50]. By identifying and tracking levels of IL-6 early on in a patient's diagnosis, it can allow both doctor and patient to have a deeper understanding of the disease stage, future course of the disease, appropriate therapy and treatments, and much more. Early diagnosis and treatment can be critical for many patients regardless of ailment. Metastatic dissemination is the main process during the growth of a human cancer tumor and is the main cause of death from cancer [51]. Early diagnosis allows for local control, less invasive surgeries, and reduced the need for chemotherapy [51]. Diagnosing a disease or cancer early also results in less time for a tumor to grow and therefore, at initial treatment there are more options [51]. Quantification of IL-6 levels is extremely important for disease control and survival.

2.6. SENSING CONCEPTS

This section discusses specific terminology and concepts that are critical to understanding the goals of the project. These terms and concepts specifically relate to graphene-based field-effect transistors and their applications in the field of wearable sensors, such as liquid gate, aptamers, Debye length, and Dirac voltage. This chapter gives an overview of GFET operation and explains the basics of sensing including a brief introduction to the Hill-Langmuir equation.

2.6.1. LIQUID-GATED FET

In the application of a wearable biosensor, using a liquid-gated FET is extremely practical. As briefly mentioned in Section 2.5, a liquid-gated FET uses a droplet of a conducting liquid in the sensing channel to apply the gate-source voltage to the device. Therefore, a liquid gate is very convenient in a wearable application, as body fluid such as sweat can easily be used as the liquid across the drain and source where the gate voltage is applied. By using sweat as the means of sensing, a non-invasive biosensor can be created, thus allowing for a more comfortable while still accurate biomonitoring device. In addition to the ease of using a liquid-gated device in the wearable application, in aptamer-based sensing techniques liquid-gating is necessary. The device used in this research is a top-liquid-gated GFET meaning that the gate voltage will be applied from the ‘top’ of the channel to the liquid gate.

2.6.2. APTAMER-BASED SENSING

Aptamer-based sensing is highly advantageous when it comes to biosensors. Aptamers are single stranded DNA or RNA ligands which can be synthesized to bind selectively to a number of targets [30], [31]. Aptamers offer many benefits such as high specificity and affinity for the target [30]. The aptamers can also be synthesized with extremely high reproducibility and purity, and they display properties ideal for biosensing upon target binding [30]. Most aptamers are selected using systematic evolution of ligands by exponential enrichment (SELEX) to choose aptamers from liquid biopsy specimens [35], [52]. The SELEX method always begins by introducing the desired target to a random library that contains between 10^{12} and 10^{16} single-stranded oligonucleotides [35], [53]. Next, oligonucleotides which bind with the target are separated out and amplified by PCR in an iterative process, each time becoming more selective to the target [35],

[53]. Finally, the remaining aptamers can be sequenced and identified [53]. This iterative process is outlined pictorially in Figure 2.2 below.

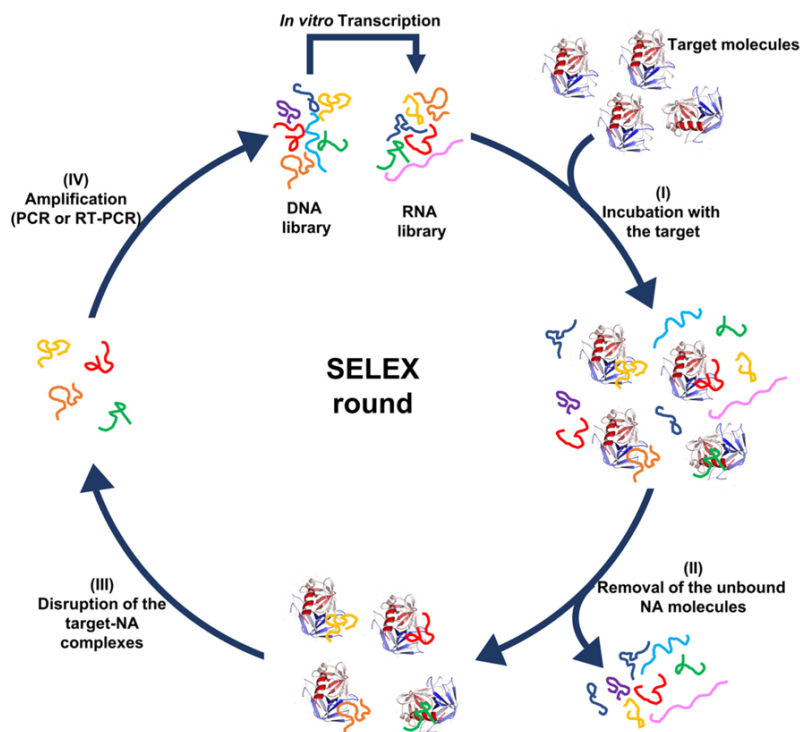


Figure 2.2: Iterative SELEX method and process of aptamer selection. Reproduced from [53].

When aptamers and targets bind together, the aptamer's physical structure changes significantly as it folds in on the protein [30], [32]. With this being said, the aptamer's new shape causes a measurable change in the charge carrier concentration in the conductive channel [10]. This change in charge carrier concentration is detected by the device as a change in the I_{DS} . Aptamers are highly selective to their designated target, meaning that their interactions are extremely limited outside of such target. The aptamers bind with high specificity as they fold into secondary and tertiary structures during target interactions [35]. Even extremely small changes in the target molecule can result in a lack of aptamer binding [30], [33]-[34]. This is a beneficial trait for a receptor when creating a biosensor as only the selected target should be able to interact with the aptamer and cause a change in the aptamer structure. Aptamers also allow for extremely

sensitive devices with dissociation constants (K_d) in the nanomolar to picomolar range [30], [33]. Aptamer-based sensors or “aptasensors” [35], are advantageous and have many benefits over using antibodies. Aptamers are more stable than antibodies as they are more robust in extreme conditions such as high temperature or harsh pH levels [35]. Also, it is possible to create aptamers that can target any molecule from a small molecule to a protein to an entire cell [31], [35], which is not the case for antibodies. Lastly, aptamers are more adaptable to changes due to their more simple chemical structures [35].

2.6.3. FUNCTIONALIZATION

Although graphene itself has not proven to be able to directly sense proteins or create links with aptamers through covalent bonding, it has shown that its π bonds have a willingness to interact through adsorption of other materials by way of π - π , π -H, π -cation, π -anion, and π -metal interactions [26]. Functionalization of the nano sensor includes the incubation of PBASE and aptamers onto the graphene surface. Single stranded probe DNAs (pDNAs) are linked to the graphene surface via the bifunctional linker 1-pyrenebutyric acid N-hydroxy succinimide ester (PBASE). PBASE and graphene form strong connections through π -stacking [16]. After immobilization of the PBASE, the aptamers can then be attached. The aptamers are introduced to the PBASE and allowed to incubate. During incubation, the aptamers and the PBASE covalently link together via N-hydroxy succinimide (NHS) crosslinking [20].

2.6.4. DEBYE LENGTH

Debye length is the distance in a semiconductor over which the local electric field influences the distribution of free charge carriers [28]. The Debye length plays an integral role in the fundamentals of the graphene-based field-effect transistor and biosensors in general. The

Debye length describes how far away from the conducting channel of a device the surface charge density can be affected [28]. The Debye length is important to understand because it is necessary that the aptamer and protein binding is occurring within the Debye length of the device. Thus, if the length of the aptamer is too long, the binding process between the target protein and the aptamer will not occur inside of the Debye screening length, and therefore will not have an effect on the surface charge density in the conduction channel. The Debye length is identified as one of the leading issues facing biosensors and FET-based devices [28]. For an electrolyte buffer solution, the Debye screening length is as follows [39]:

$$k_D^{-1} = \sqrt{\frac{\epsilon kT}{e^2 \sum_i Z_i^2 n_i^B}}$$

where k and T are the Boltzmann's constant and temperature respectively, e is the charge of a proton, ϵ is the permittivity of the solvent, Z_i is the charge concentration of ion species i and n_i^B is the bulk concentration of ion species of i , extending the sum over all ions in the solution [39].

2.6.5. DIRAC VOLTAGE

Graphene-based field-effect transistors exhibit ambipolar behavior meaning that both electrons and holes can be the majority charge carrier depending on the gate-to-source voltage for the device. Resultingly, the current-voltage characteristics of a GFET device are V-shaped with a clear location in which the number of electrons and holes are even, known as the charge neutrality point or Dirac Voltage. This is detailed in Figure 2.3 below where two transfer characteristic curves are shown: one before target binding and the other after target binding.

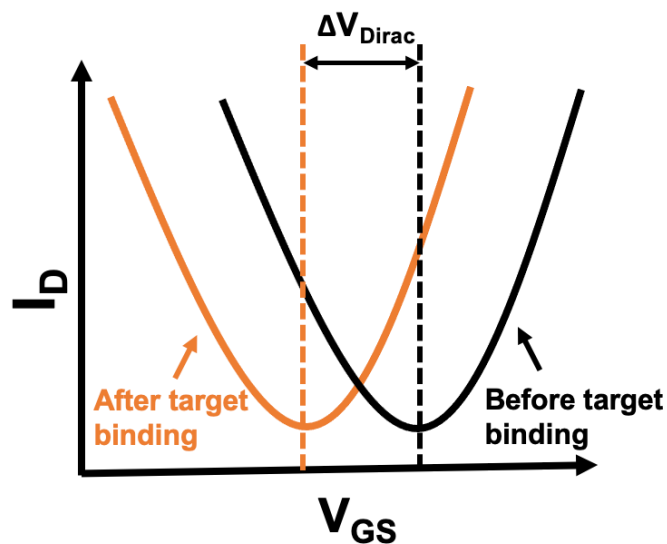


Figure 2.3: V-shaped transfer characteristic curve (I_D vs V_{GS}) with Dirac voltage before and after target binding.

The left branch of the transfer characteristic curve is when the density of holes is increasing, and the right branch of the characteristic curve is when the density of electrons is increasing [77]. The point where the charge neutrality is even corresponds to the minimum drain-to-source current and the gate voltage that corresponding to the minimum current, is referred to as the Dirac Voltage [78]. The Dirac voltage is important as it is where the shifts in transfer characteristic curve are measured about. As different concentrations of target analyte are introduced to a device, the Dirac voltage should shift to the left or right depending on the charge of the target. This movement in transfer characteristic curve should be proportional to the concentration of the target that was introduced. The change in Dirac voltage versus concentration of the target analyte should follow the Hill-Langmuir equation. The Hill-Langmuir equation describes the relationship between the concentration of a target analyte and the number of receptors, or in this case aptamers, that have bound to a target [22]. The Hill-Langmuir equation is used as a benchmark to describe the rate at which ligands will bind with receptors and is outlined as follows [22]:

$$\Delta V_D = A \frac{[c/K_a]^n}{1 + [c/K_a]^n} + Z$$

A = Maximum response with all binding sites occupied

c = Concentration of all the applied target

K_a = Apparent dissociation constant that produces half occupation of receptors

n = Hill coefficient

Z = Parameter offset

2.6.6. SENSING MECHANISMS

There are two different sensing mechanisms which have a direct impact on the Dirac voltage and how it shifts. These two mechanisms are the electrostatic gating effect and the charge transfer doping effect. While both are similar, one causes positively charged biomolecules to shift the Dirac voltage in the positive direction while the other causes positive charges to create a shift in the negative direction, and opposite for negative charges in both cases. The overall resulting behavior is a combination of these two processes and therefore the more dominant process will ultimately decide how positive and negative charges influence the Dirac voltage.

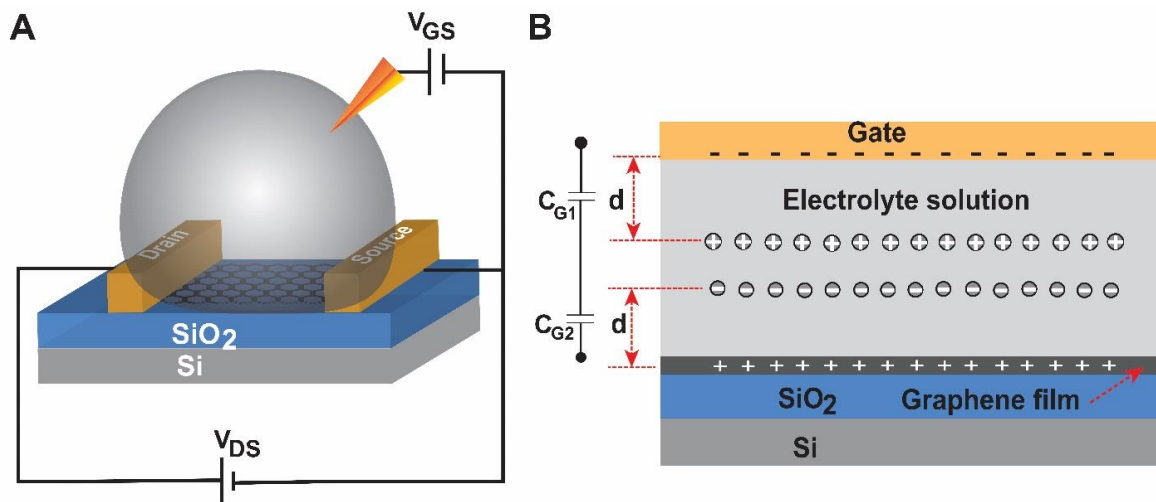


Figure 2.4: (A) Schematic of electrolyte liquid-gated GFET (top-gated); (B) Electrostatic gating effect demonstrated with capacitors formed at the graphene-solution and gate-solution interfaces. Reproduced from [42].

The electrostatic gating effect is when the concentration of the adsorbed charged molecules is so high that the intermolecular distance is less than the Debye length [42]. Subsequently, the adsorbed molecules act as one of the two plates of the electrical double layer (EDL) formed on the graphene-electrolyte interface as shown in Figure 2.4(B). Therefore, any additional charged molecules which are adsorbed onto the graphene will modulate this charge density in the EDLs resulting in a change in the channel current [42]. Therefore, if the adsorbed molecules are positively charged, the Dirac voltage will shift in the negative direction and result in having to apply a voltage that is less positive to compensate for the additional charge stored in the EDL [42], [75], [76]. In a similar way, if the molecules that are adsorbed into the graphene are negatively charged, the resulting Dirac voltage will shift in the positive direction and therefore a more positive charge will need to be applied due to the negative charges in the EDL [42], [75], [76].

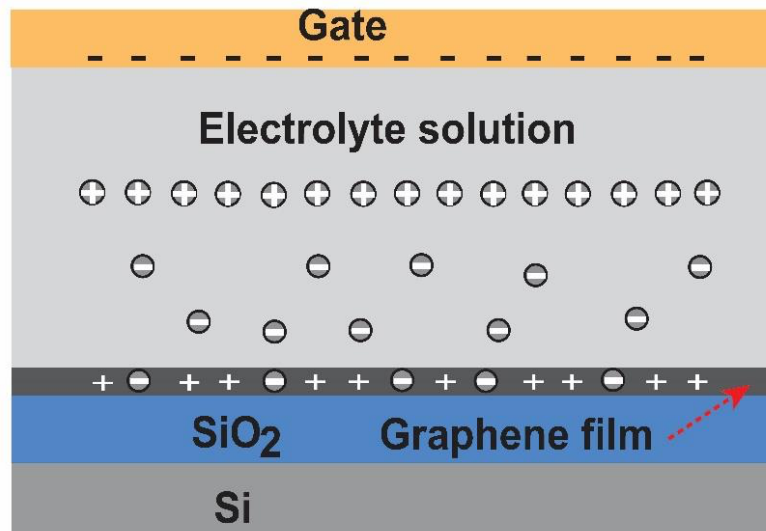


Figure 2.5: Charge transfer doping effect demonstrated in GFET. Reproduced from [42].

The charge transfer doping effect is a result of direct charge transfer from the adsorbed molecules to the graphene surface [42]. This happens specifically when the biomolecules introduced are at low concentration or are weakly charged as detailed in Figure 2.5 [42]. This causes the adsorption density to be small and therefore the distance between the adsorbed

molecules is larger than the Debye length of the channel [42]. Furthermore, the charge transfer is then dominant between the adsorbed molecules and the channel itself [42]. Therefore, if adsorbed molecules are positively charged, the Dirac point will shift in the positive direction or if negative charges are introduced the Dirac voltage will shift in the negative direction [42], [75].

CHAPTER 3: MATERIALS AND METHODS

3.1. OVERVIEW

This chapter discusses in-depth the device fabrication procedure for creating the printable and flexible graphene-based field-effect transistor (GFET) platform. This chapter also includes an overview of how KiCAD is used to create the design, using the Voltera V-One PCB printer to print the design, and easy transfer graphene which is used as the conductive channel between the source and drain electrodes. Reliability throughout the fabrication process is also discussed. This chapter includes all necessary steps and procedures to fabricate the GFET.

3.2. DEVICE FABRICATION

3.2.1. KICAD

The fabrication process of the wearable GFET begins with the initial design that is created using KiCAD which is an open-source computer aided design software. The KiCAD schematic includes the layout for all drain, source, and gate electrodes. The KiCAD software allows for variation in trace width, layer, shape, and a variety of other tools. The final design features six drain/source electrodes and one gate electrode as shown in Figure 3.1. Table 3.1 details the layout of the GFET design specifically which electrodes are the drain, source, and gate for each of the five GFET devices created in the pattern.

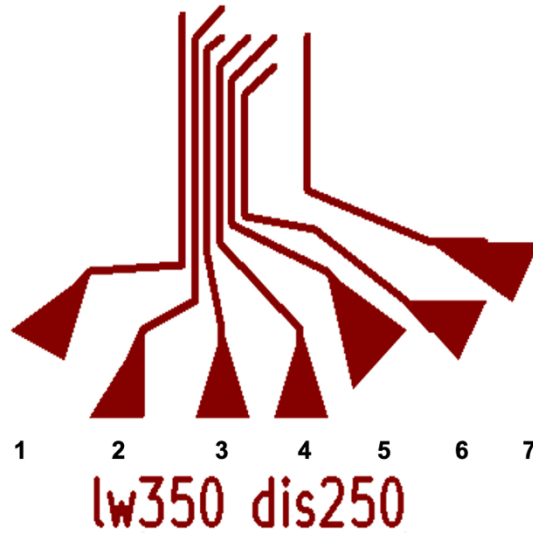


Figure 3.1: Final KiCAD design featuring 7 electrodes; electrodes 1 – 6 as drain/source and electrode 7 as gate with line width 350 μ m and line spacing 250 μ m edge to edge.

Trace width and trace spacing were two factors that were critical to optimize for the printable device. It is important to balance these two elements as the smallest feature size possible is needed while also keeping the widest possible electrode in order to reduce the trace resistance. Upon completion of the KiCAD design, multiple files are generated with each of the different printing layers, which can then be uploaded into the Voltera software for the next fabrication step.

Table 3.1: Summary of labels for final GFET device.

Device #	Source/Drain electrode	Gate
GFET-1	1/2	7
GFET-2	2/3	7
GFET-3	3/4	7
GFET-4	4/5	7
GFET-5	5/6	7

3.2.2. VOLTERA V-ONE PCB PRINTER

The goal during fabrication of the GFET biosensor was to create a low cost, time effective and adaptable procedure that would allow for easy replication and production of many devices. Most often in fabrication of microdevices and biosensors, techniques such as lithography, etching, and liftoff are used [1], [6], [40]. These procedures are quite costly and can take a large amount of time to carry out. It can also be quite a rigid process as in order to change even the smallest of characteristics requires a lot of work, for example creating a new mask each time a minor change needs to be made. In this application, to fabricate the electrodes for the GFET, a Voltera (Kitchener, Canada) V-One PCB printer was used. The Voltera V-One PCB printer, shown in Figure 3.2, is a multi-functional circuit printer that is especially good for higher viscosity inks and can print on a wide variety of substrates.

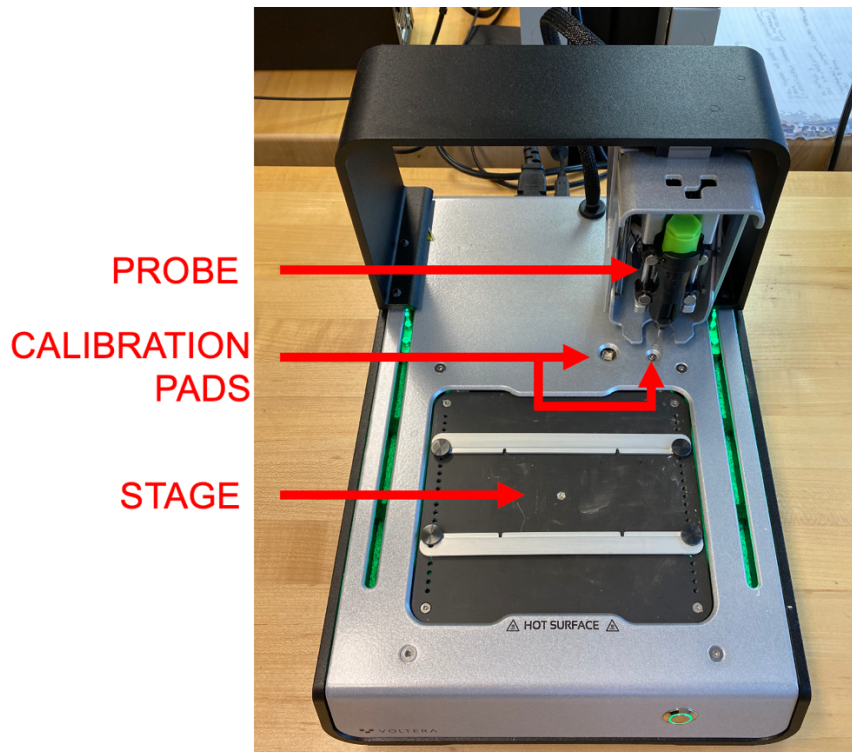


Figure 3.2: Voltera V-One PCB printer used for rapid fabrication of GFET electrodes.

The printer allows the user to upload a CAD file and then simply prints the CAD file pattern onto the substrate of the user's choice. Moreover, this results in an extremely fast and adaptive process as changes to features such as line width, substrate, ink or even large changes to the design can be swapped in seconds and reflected to the device during printing within minutes. The Voltera V-One printer prints patterns extremely quickly. Although the printing time is directly proportional to the size of the design, number of lines and shaped to be printed, most designs are printed in under 3 minutes with the whole printing process taking a total of about 25 minutes, including 15 minutes for heating to dry the ink. The Voltera allows for the user to control a variety of settings and printing conditions such as printing speed, height, flow rate and many others as shown in Figure 3.3. Such flexibility in printing conditions does create room for human error and therefore a KiCAD pattern that can be implemented to the Voltera without concern of electrode shorts and design issues must be created.

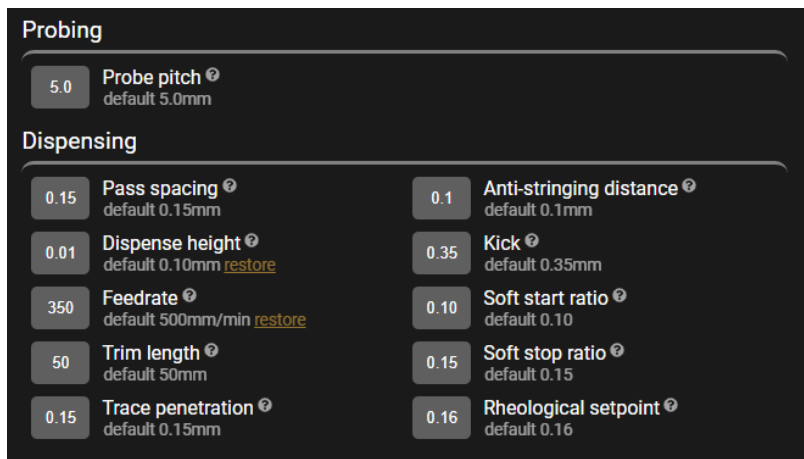


Figure 3.3: Voltera V-One printer settings options.

3.2.3. PRINTING RELIABILITY

As mentioned previously, ensuring that the feature size of the device is as small as possible is extremely important while also maximizing the width of the traces. In order to ensure reliable printing where none of the electrodes short together during the printing process, a variety of both

trace width and trace distance are assessed. Table 3.2 below shows the combinations of electrode widths and distances, measured from edge to edge, that were tested. All design specifications were printed using the Voltera V-One, utilizing the 100-micron nozzle heads and standard printing conditions specified from Voltera. While the first few options were not viable as the Voltera V-One could not print this close consistently without the electrodes shorting together, the distances above 250 μm proved to work well. After analysis, a 350 μm electrode width with an electrode distance of 250 μm gave the most consistent results with the largest electrode width yet smallest distance between electrodes.

Table 3.2: Electrode widths and distances tested in KiCAD design and printed with Voltera.

Electrode Width (μm)	Electrode Distance (μm) (edge to edge)
100	100
100	150
150	150
250	250
250	500
250	700
*350	*250
350	500
450	500

*Final design parameters

Once the design is finalized and printed, the substrate is heated at 100 degrees Celsius for 15 minutes in order for the ink to cure. At this point the initial design is completed and the electrodes are ready for graphene.

3.2.4. EASY TRANSFER GRAPHENE

A field-effect transistor needs a conducting material placed between the drain and source electrodes in order to function. A GFET utilizes a graphene film to create this channel. Graphene

transfer is done using chemical vapor deposition (CVD)-grown graphene from Graphenea Inc. (San Sebastián, Spain). These graphene sheets are known as easy transfer monolayer graphene which are created on a polymer film and covered with a sacrificial layer as shown below in Figure 3.4 [23].



Figure 3.4: 1 cm \times 1 cm easy transfer monolayer graphene from Graphenea on a polymer film.

A unique fishing technique is employed in order to ensure a higher success rate in placing the graphene more precisely across the drain and source electrodes. The traditional fishing method consists of placing the sacrificial layer/graphene/polymer substrate onto the surface of deionized water slowly. The backing is then slowly peeled away using tweezers, leaving just the sacrificial layer/graphene. Finally, using the substrate below the water, catch the sacrificial layer/graphene perfectly across the electrodes. This entire process is outlined in Figure 3.5, courtesy of Graphenea.

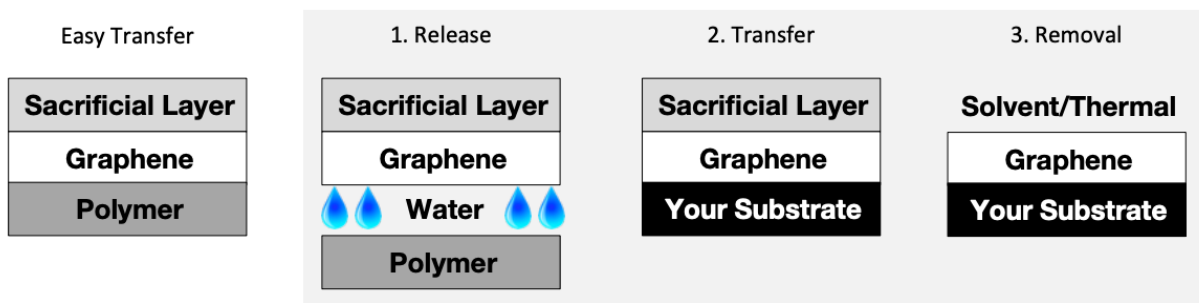


Figure 3.5: Graphene transfer process using fishing technique. Reproduced from [5].

This method was slightly modified to increase consistency when placing the graphene across the electrodes. Instead of taking the bulky substrate and placing it under the graphene and trying to quickly lift and catch the graphene, a modified process was used. By using a pipette and placing approximately enough deionized water to cover the device on the substrate, this removes a large amount of uncertainty of where the graphene will land. The sacrificial layer/graphene/polymer substrate are then placed into this much smaller droplet and the polymer substrate is then slowly removed. Next, the water is slowly removed using the pipette and along the way the sacrificial layer/graphene is directed until it is in the desired location. Once the sacrificial layer/graphene are across the electrodes, the device is allowed to air dry for one hour and then heated at 250 °C for one hour. After the heating process, the sacrificial layer is then removed by submerging the sacrificial layer/graphene/new substrate in acetone for one hour, ethanol for one hour, and deionized water for one hour. After completing all fabrication steps including design, printing, and graphene transfer shown in Figure 3.6(A), the device will look as shown in Figure 3.6(B).

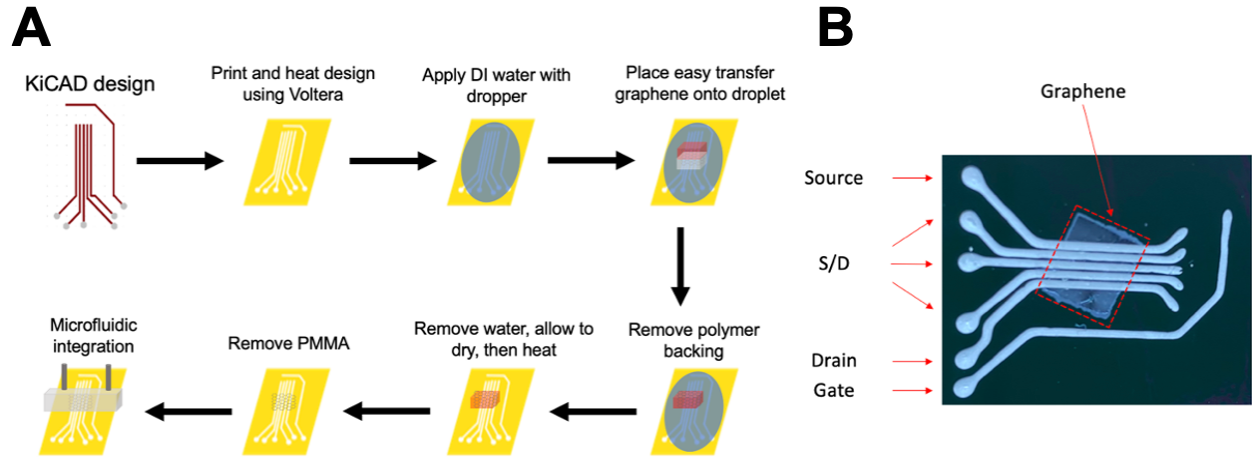


Figure 3.6: (A) Fabrication steps for the GFET device; (B) Voltera V-ONE printed graphene-based FET on Si/SiO₂ wafer using KiCAD design. Easy transfer monolayer graphene transferred across drain and source electrodes.

CHAPTER 4: CHARACTERIZING GFET

4.1. OVERVIEW

This chapter discusses the process of finalizing all parameters of the GFET biosensor design. A characterization of multiple substrates choices is presented as well as a comparison of multiple inks that can be used in conjunction with the Voltera V-One printer. After finalization of the design parameters, this chapter also presents the methods of preparing the device for biosensing. Preparation includes functionalization of the graphene surface and immobilization of aptamers on the graphene as well.

4.2. REQUIRED MATERIALS

For GFET characterization and sensing the following materials are needed:

- 0.01 × PBS buffer: 200 μ L of 10 × PBS is combined with 199.8 mL of deionized water.

This ratio is used as 0.01 × PBS has a Debye length of approximately 7.3 nm [23].

- PBASE in DMF: 10 mM solution of PBASE in DMF is created in order to functionalize the graphene. PBASE was purchased from Santa Cruz Biotechnology (TX, USA).

- Aminated aptamers: Aptamers with specific affinity to mouse IL-6 (#ATW0077, $K_D = 5.4$ nM) were purchased from Basepair Biotechnologies, Inc. (TX, USA). The aptamers were prepared following the Basepair Biotechnologies, Inc. best practices: Handling and Storage information and therefore used amine resuspension buffer and the 0.01 × PBS +1 mM $MgCl_2$ solution. 1 mM $MgCl_2$ is used in order to help the aptamers bind properly as changes in magnesium chloride have been proven to have an effect on binding affinity [23]. This solution is created using 10 μ L of 10 × PBS, 9.99 mL of deionized water and finally 1 g of $MgCl_2$.

- Interleukin-6 recombinant mouse protein: IL-6 protein was purchased from BioLegend® (San Diego, CA) and prepared into five different concentrations. The IL-6 protein is 34 μM as packaged and concentrations of 100 nM, 10 nM, 1 nM, 100 pM, and 10 pM were prepared using $0.01 \times \text{PBS}$.

4.3. SILICON OXIDE COATING

Silicon oxide coating has proven to enhance the sensing performances of GFET devices. Naturally occurring organic contaminants can cause issues with sensor sensitivity, decreased carrier mobility and unwanted doping of the substrate [6]. By using an SiO_2 coating on the substrate, it helps prevent many of these issues by improving the substrate surface. First of all, the coating provides protection for the graphene against unwanted doping and also provides a smoother surface for the device which allows for a higher quality fabrication of the GFET device [6]. Secondly, the coating has also been proven to have tremendous impacts on the transconductance of the device which is directly related to the sensor sensitivity. Lastly, the silicon oxide coating provides more consistency in the overall sensor performance. Zhuang et al. exemplify how the silicon oxide coating creates not only a more consistent IV characteristic curve for their device, but it also creates sharper edges and therefore higher transconductance near the Dirac voltage [6]. This is extremely beneficial as during the real-time sensing, the sharper these curves are, the more change will be observed in the current with relation to time. The device consistency, transconductance, and surface morphology results are summarized in Figure 4.1.

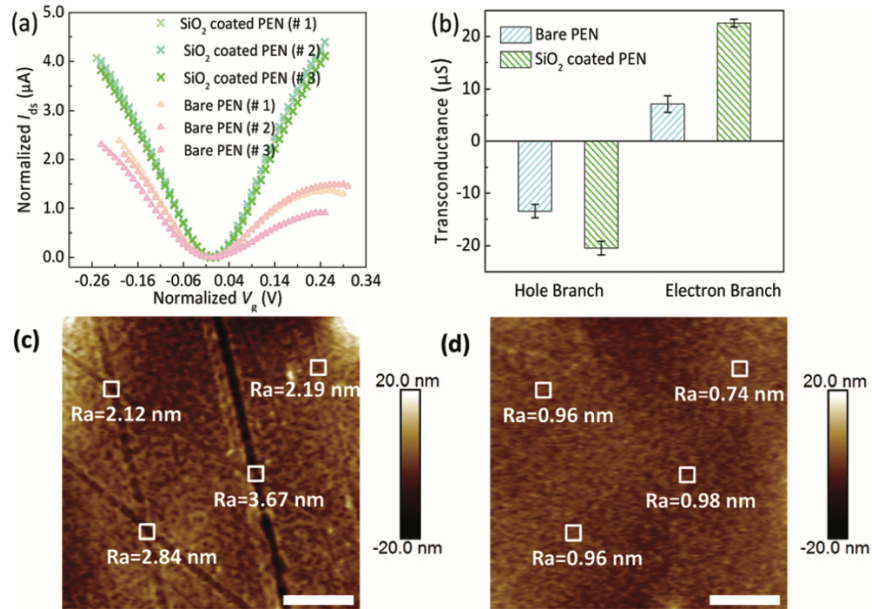


Figure 4.1: SiO₂ coating impacts on (a) device transfer characteristic curve; (b) device transconductance in both the hole and electron branches; (c,d) surface morphology of bare substrate and 50 nm SiO₂ coated substrate. Reproduced from [6] with permission from the Royal Society of Chemistry.

While finalizing the design features and parameters of the flexible biosensor, an SiO₂ coating on multiple substrate options was investigated. A 50 nm SiO₂ coating was deposited onto the bare Kapton film (12 inches × 12 inches × 1 mil) using a sputter deposition system from the Nanofabrication Laboratory at the University of Massachusetts Lowell. The goal here is to ensure that the SiO₂ coating has the same impact, specifically on the transfer characteristic curve, as outlined above in Figure 4.1. In order to ensure the reliability of the results, the effect of a 50 nm SiO₂ coating was explored on the Kapton film.

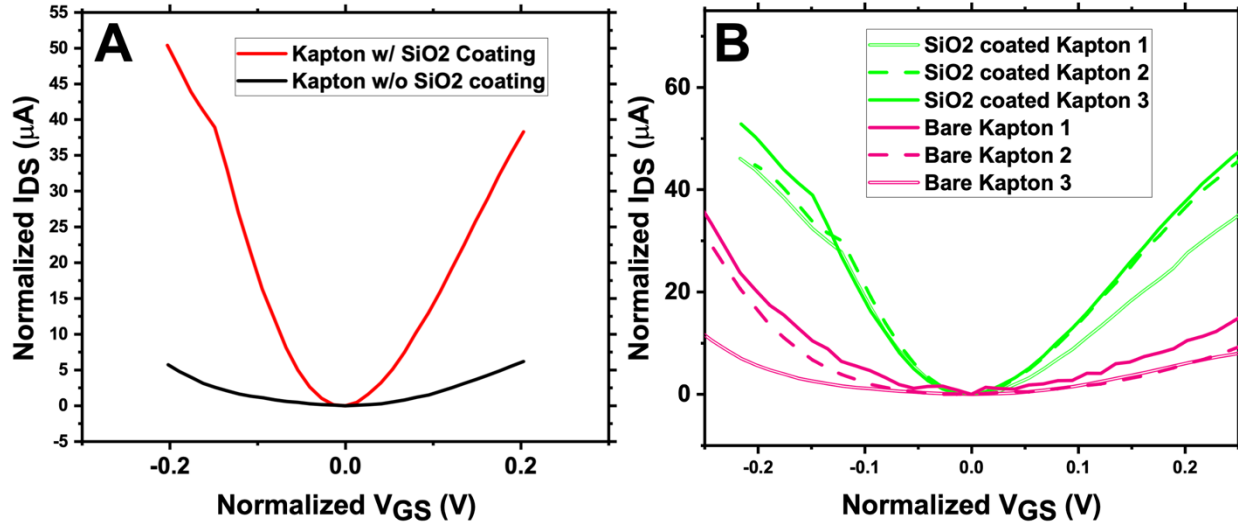


Figure 4.2: Transfer characteristic curve of GFET device fabricated on (a) Kapton substrate with 50 nm SiO₂ coating versus bare Kapton film; (b) SiO₂ coating provides consistency to transfer characteristic curve measurements.

Consistent with the results from the Lin et al. research paper, the SiO₂ coating proves to produce a significantly steeper transfer characteristic curve [6]. Figure 4.2(A) shows that the silicon oxide coating improves the device characteristics. In Figure 4.2(A) the bare Kapton curve reaches a maximum normalized current of about 7 μA while the SiO₂ coated Kapton reaches a normalized current of about 50 μA , thus vastly improving the conductivity of the device. In Figure 4.2(B) the device consistency is displayed. The SiO₂ coated Kapton GFETs (k-GFETs) display more consistent results device to device on the same substrate in comparison to devices fabricated on the bare Kapton film.

4.4. SUBSTRATE SELECTION

A wearable biosensor must be accommodating to the human body and thus needs to be able to be integrated in a wearable and flexible platform. Substrate choice is key as it will ensure the safety and subsequently the effectiveness of the biosensor. Substrates such as biaxially-oriented polyethylene terephthalate (Bo PET) also known as Mylar, polyamide film named Kapton by

DuPont, and polydimethylsiloxane (PDMS) are all substrates that could accommodate the needs of the device.

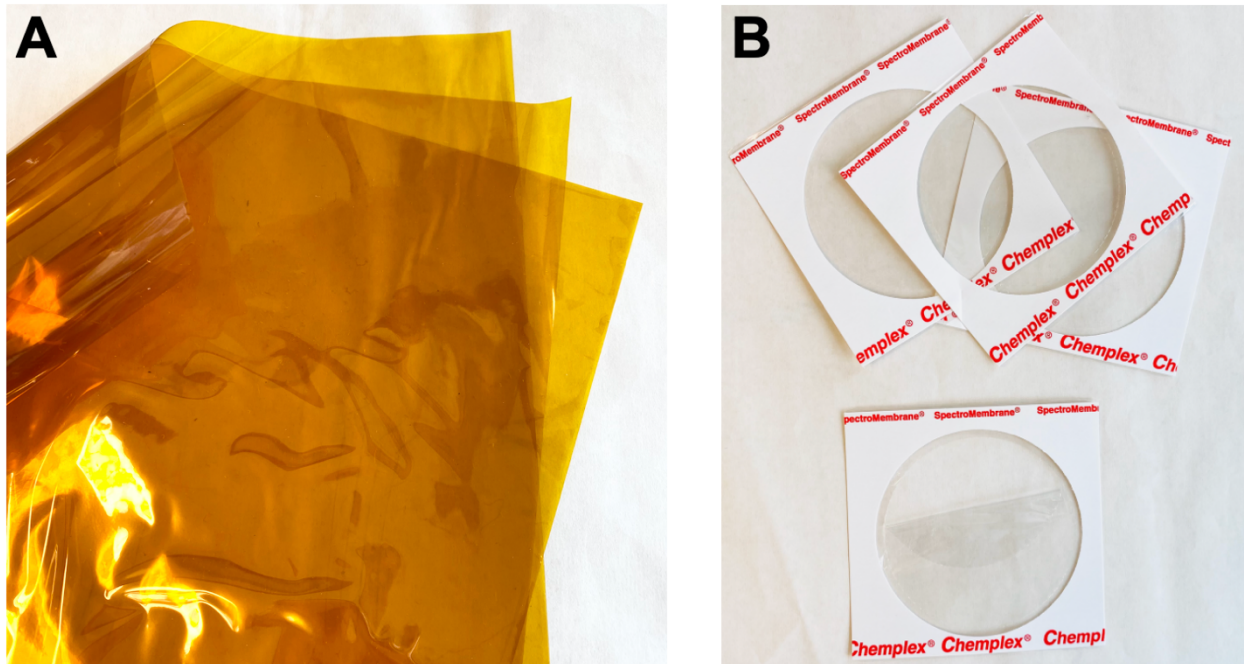


Figure 4.3: Flexible film substrates (A) Kapton substrate; and (B) Mylar substrate.

Kapton is a polyimide film which is lightweight and bendable, shown in Figure 4.3(A). The Kapton film used in this application was 0.001 inches thick which is about 25 μm . The mylar film being used was 2.5 μm and therefore about 10 times thinner. The Kapton was able to provide more structure and its rigidity helped prevent potential tears while still offering an extremely bendable device. Kapton has an extremely high melting point and thus can withstand extreme heat up to 400 $^{\circ}\text{C}$ [18]. Mylar is a polyester film that is extremely thin and lightweight and conforms well to the skin, thus giving it potential as the substrate for a wearable device (Figure 4.3(B)). Mylar is a transparent film that is commercially available for purchase at a thickness of 2.5 μm [10], [58]. It offers advantages such as a high tensile strength, electrical insulation, and stability [17]. Disadvantages of this film include a tendency to easily crumple and tare thus causing issues

for the sensor and a relatively low melting point in comparison to other films at 250 °C. Another disadvantage to using a Mylar film is that it frequently requires bonding to a rigid substrate during fabrication [10]. While both Mylar and Kapton are thin films that present themselves as possible options for a wearable sensor substrate, there are also silicone materials that could be advantageous as well.

Silicone rubbers are often used in the creation of microchannels and nanoscale devices as they are easily implemented for stamping, molding, and the surface properties are easy to modify [88]. PDMS is widely used as it is low cost, simple to fabricate, thermally stable, resistant to oxidation, clear and easily pliable as shown in Figure 4.4 [56], [59]. PDMS is a commercially available two-part silicon-based polymer. It can easily be molded to various shapes, cut, bent, and even stretched to a degree without compromising the integrity.



Figure 4.4: Polydimethylsiloxane (PDMS) polymer substrate.

The PDMS substrate provides flexibility similar to Mylar and Kapton but also provides more strength than the two previously mentioned substrates.

To select the proper substrate for device fabrication, the KiCAD design was printed onto each of the three potential substrates which had each been coated with 50 nm of SiO₂. A silicon wafer substrate with the same design was also used during the process as a baseline for comparison. Graphene was then transferred across each of the four designs and the bare graphene transfer characteristic curve of each GFET device was measured as shown below in Figure 4.5.

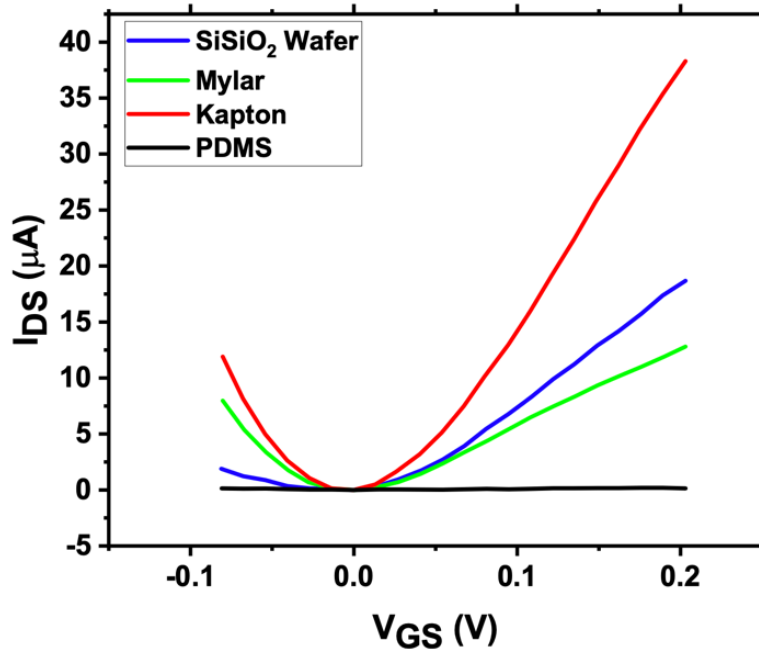


Figure 4.5: Transfer characteristic curve with $V_{DS} = 100\text{mV}$ for Si/SiO₂ wafer (baseline), SiO₂ coated Mylar, SiO₂ coated Kapton, and SiO₂ coated PDMS.

The Kapton substrate exhibits the sharpest I_{DS} versus V_{GS} characteristic curve, making it the best option for creating a wearable biosensor moving forward. Mylar displays promising results as the magnitude of the current is similar to the silicon wafer which was used as a baseline. Alternatively, the GFET device fabricated on the PDMS substrate displays almost no change in current flow regardless of the gate-to-source voltage which was applied to the device. This excludes the PDMS substrate from being a viable option as it will make it extremely difficult to identify the Dirac voltage for a GFET with a characteristic curve with such a gradual incline.

4.5. INK CHOICE

In the ideal case for a wearable, the sensor would be fabricated on a flexible and stretchable substrate and the device itself would also be able to stretch and bend. In order to understand if a fully stretchable and bendable device is feasible, a variety of inks were tested on a flexible and stretchable Eco-Flex silicone rubber substrate. Eco-Flex is a two-part silicone rubber similar to PDMS. A combination of inks was investigated including Voltera Flex Ink, Dycotec Flexible and Stretchable ink, and multiple homemade ink mixtures.

A homemade ink mixture is attractive for creating a GFET device as the base material can be controlled and thus can be used to increase flexibility and stretchability. In this application a PDMS base was used for the ink with a mixture of carbon nanotubes, carbon nanofibers, and silver flakes [60-62]. In order to create the ink, the PDMS polymer-base was first mixed with toluene as this will allow for the conducting particles to be evenly dispersed [62]. The carbon nanotubes, carbon nanofibers, and silver flakes are then added to the toluene solution which is then placed into a bath sonicator for 5 minutes to ensure particle dispersion. After dispersion, the solution is placed onto a hot plate and heated at low temperature (70 °C) while simultaneously magnetically stirred until the toluene solution is evaporated [62]. After evaporation, the PDMS curing agent is added to the mixture and is ready to be used as an ink. While the printable ink is an attractive option, after numerous attempts with variety in amount of carbon nanotubes, carbon nanofibers and silver flakes, the ink was never conductive enough to support a current and therefore one of the two commercially available inks would need to be used moving forward.

The ink stretchability was investigated by printing ten 1 mm wide electrodes onto the Eco-Flex substrate. This was done for each of the two commercial inks, as the custom ink was never able to support a current. After curing, the electrodes were then encapsulated in another thin Eco-

Flex layer for support. Beginning with the Voltera ink, the 10 electrodes are printed onto the substrate and the resistance of each electrode is measured and recorded. The KiCAD file for the stretchability testing is shown in Figure 4.6.

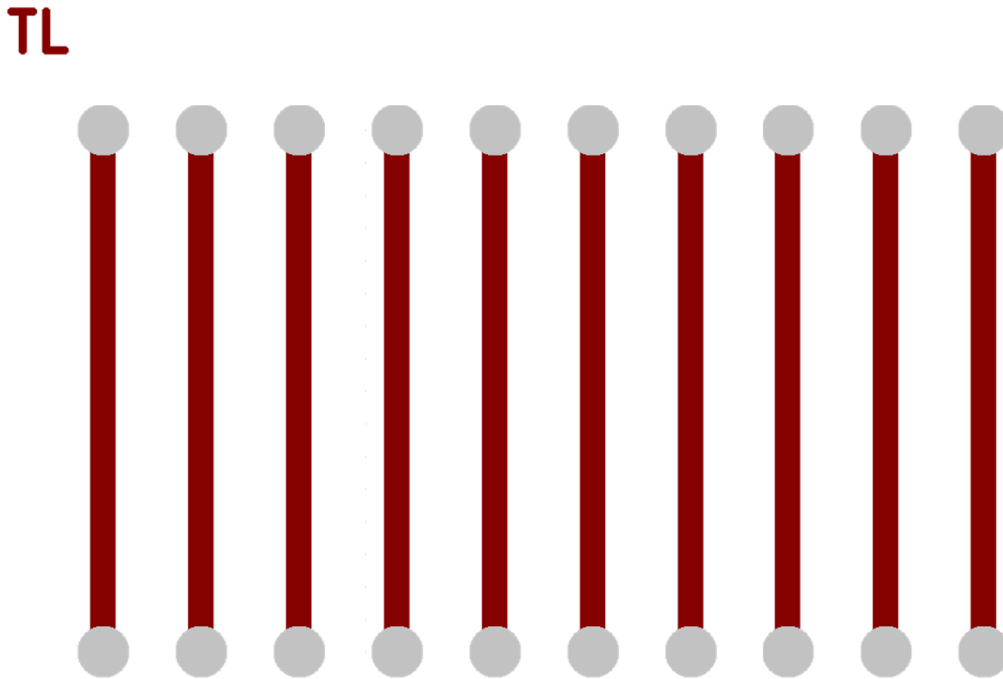


Figure 4.6: KiCAD stretchability file containing ten 1 mm wide traces.

The electrodes are then stretched at increments of 5% in order to better understand the trend of resistance versus stretching percentage (electrode length). This process is repeated until the electrode resistances are into the range of megaohms or the electrodes themselves break. The Voltera ink was highly conductive at 0% stretching and had an average trace resistance of 0.4889 ohms. After being stretched to just 5% of the original electrode length, all of the electrodes had broken as outlined in Figure 4.7. Although advertised as a flexible ink, even upon extremely small levels of handling or bending of the substrate, the Voltera ink traces broke.

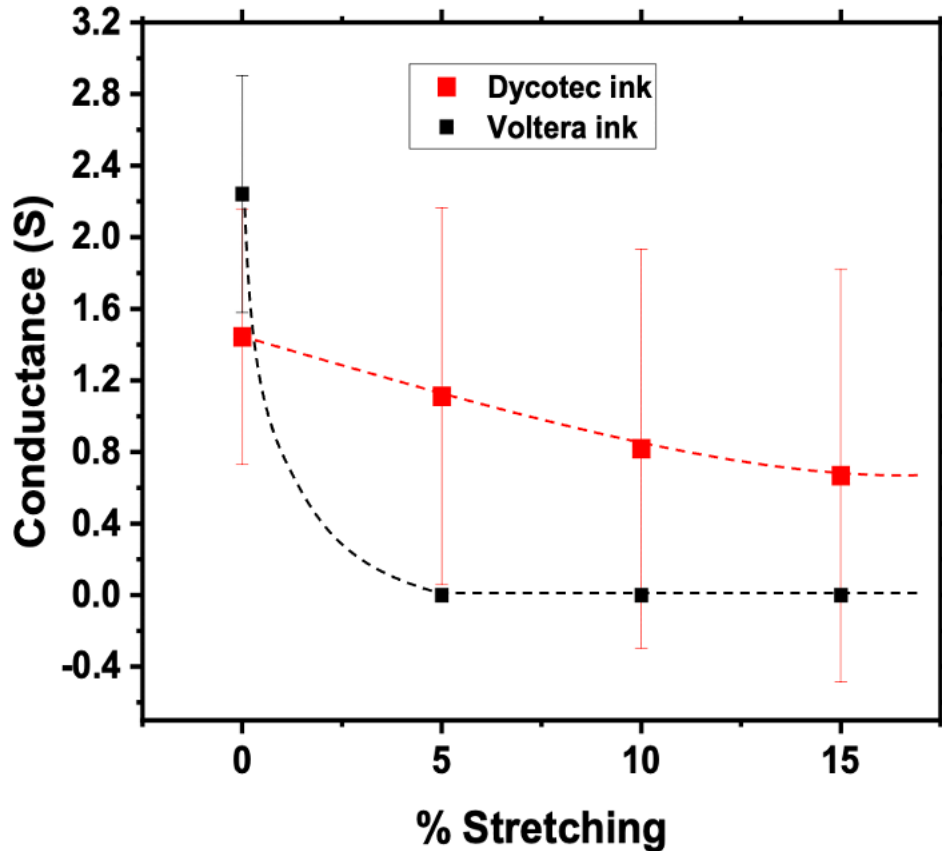


Figure 4.7: Dycotec stretchable silver conductive ink versus Voltera Flex silver conductive ink.

Following the same process as above, the Dycotec ink was examined next. During this analysis, the average resistance was 0.67 ohms at 0% stretching, and 31.8 ohms, 93.1 ohms, and 561.8 ohms at 5%, 10% and 15% respectively as shown in Figure 4.7. Above 15%, although there was data collected, the error was so large that it is not reliable as it may not be reproducible in the future. Thus, to continually select the most advantageous parameters for creation of the GFET biosensor, the device is be printed on Kapton film with a 50 nm SiO₂ coating using the Dycotec silver conductive ink as shown in Figure 4.8.

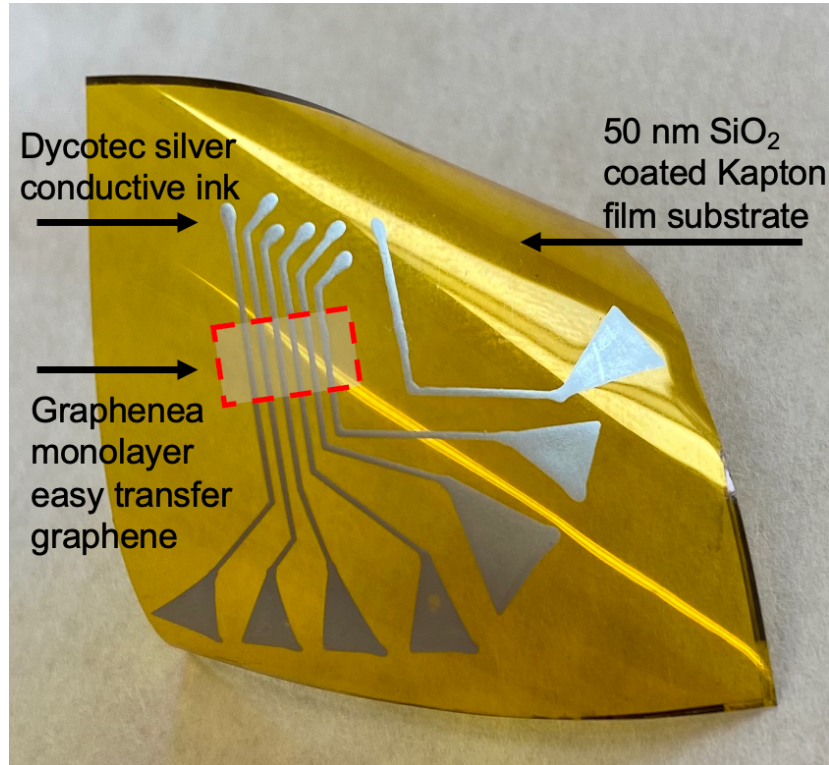


Figure 4.8: GFET design with all parameters finalized. Substrate: 50 nm SiO₂ coated Kapton; Ink: Dycotec flexible and stretchable silver conductive ink.

4.6. MECHANICAL STRESS

Making sure that biosensor operation does not change from basic, rigid implementation to wearable, bendable implementation is critical. It is only practical that device functionality is stable over various bending radii as in the GFET biosensor's true application, mechanical stresses on the substrate are unavoidable. GFET sensors have been proven to be able to withstand a wide range of mechanical stresses including bending [6], [10], [55], stretching [40], twisting, and a combination of all at once [10]. In order to understand the appropriate range of substrate bending that the GFET can withstand and should be used in, the Kapton substrate was characterized at different bending radii. The procedure for characterization was to begin with the blank device completely flat to obtain a baseline measurement for the GFET characteristic curve. After this, the GFET was bent using three different inward bending substrates with radii of 4.25 cm, 2.25 cm and

1.5 cm respectively. The GFET transfer characteristic curves were then measured once again to observe the Dirac voltage and potential shift. This process was repeated for 3 different inward bending radii as in real applications the device would be facing the skin and therefore the most likely bending would be an inward bending.

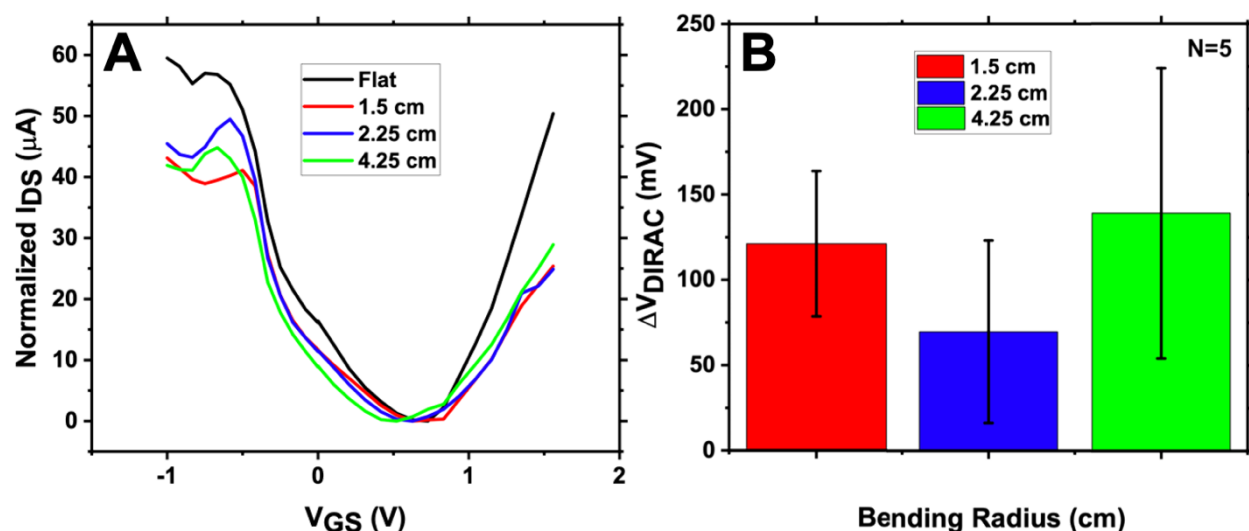


Figure 4.9: (A) Transfer characteristic curve of GFET on flat substrate and bent around radii of 1.5 cm, 2.25 cm, and 4.25 cm; (B) Change in Dirac voltage with respect to the bending radius of the substrate. Error bars created with $N = 5$ devices.

As can be seen in Figure 4.9(A), the inward bending of the substrate did cause variation in the transfer characteristic curve. Figure 4.9(B) shows the change in Dirac voltage with respect to the bending radii of the device. The error bars are created with five devices. While all bending radii show a very small shift in Dirac voltage, the 2.25 cm bending radius showed the least amount of variation in transfer characteristic curve and shift in Dirac voltage. Following this was the smallest bending radius of 1.5 cm and lastly the most variation was in the largest bending radius of 4.25 cm. A relatively random shifting in Dirac voltage with respect to bending radius is consistent with previous works [6]. A small change in Dirac voltage is consistent with other findings as well [6].

The results obtained from these analyses suggest that the biosensor can operate properly in all of the bending conditions observed in this work.

4.7. GFET FUNCTIONALIZATION

In order to prepare the graphene FET to be used as a biosensor, the target molecules need to interact with the GFET and influence the charge carriers in the conduction channel of the transistor. The first step of the functionalization process is to add PBASE to the graphene surface. PBASE is essential to the GFET device functioning properly as this linker allows for aptamers to attach to the graphene surface and therefore targets will directly be able to influence the device drain-source current.

Functionalization of the device is done by placing a 200 μL droplet of 10 mM PBASE in dimethyl formamide (DMF) onto the graphene surface at room temperature for 2 hours. The device is prepared for functionalization by mounting an Eco-Flex well (1 cm \times 0.5 cm \times 0.5 cm) across the drain and source electrodes to keep the PBASE solution on the graphene surface, as DMF is extremely volatile and could interfere with the bare silver electrodes. After the PBASE in DMF has incubated for two hours, the substrate is then washed successively with DMF, ethanol, and deionized water for 3 minutes each. This ensures that there are no loose PBASE linkers still on the substrate. Immobilization of the PBASE linker onto the graphene surface causes a p-type doping effect to the graphene and will cause the transfer characteristic curve and Dirac voltage to shift to the right due to the transfer of charges between the PBASE and graphene [63], [64]. The carbonyl group of PBASE is an electron-withdrawing group which means it can cause electron transfer to occur from the graphene to the linker, which is why there is a positive shift in Dirac voltage [65]. The last step in the GFET functionalization is the immobilization of the aptamers. The aptamers used during sensing are synthesized from BasePair Biotechnologies, Inc (TX,USA). The aptamer

target for selection is recombinant mouse Interleukin-6 (IL-6). The aptamers are single stranded DNAs with a length of 32 nucleotides and an average K_D of 5.4 nM [36]. Aminated (5') pDNA at 5 μ M in $0.01 \times$ PBS+1 mM $MgCl_2$ are introduced to the graphene in the form of a 100 μ L droplet again at room temperature for two hours. After incubation, the excess aptamer solution is then rinsed with $0.01 \times$ PBS in order to remove all leftover aptamers. Immobilization of the aptamers causes in a left shift because of n-type doping which results due to negatively charged DNA strands serving as electron donors when they interact with the graphene surface [65]. A positive shift due to PBASE attachment and a negative shift from aptamer immobilization is consistent with results from [6], [65], [82]. These results are summarized below in Figure 4.10. With the aptamers securely linked via PBASE to the graphene surface, the GFET can be used as a nano sensor.

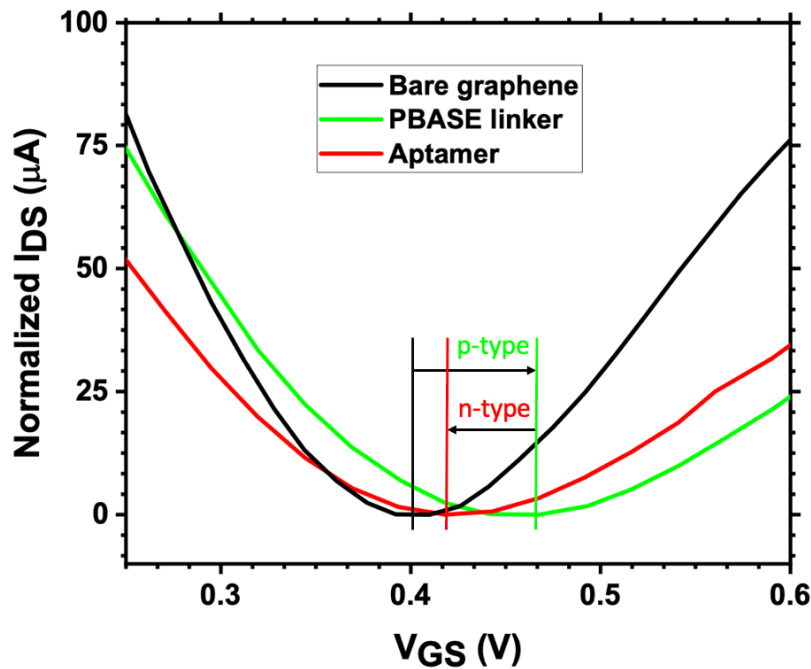


Figure 4.10: Transfer characteristic curves during functionalization displaying p-type doping after introduction of PBASE and n-type doping after introduction of aptamers.

The immobilization of aptamers onto the graphene surface is critical in order for the graphene-based FET to operate as a biosensor. Without the aptamers and PBASE linkers attached

to the graphene surface, the IL-6 proteins do not bind with the graphene surface. Without this binding there will be no shift in the drain current with respect to the gate-to-source voltage and therefore the concept which is being employed here will not hold. Figure 4.11 demonstrates the importance of using the aptamers and the linkers to achieve selective sensing on a graphene-based platform. Without the linkers and the aptamers present, there is practically zero change between the bare graphene characteristic curve and the five subsequent concentrations of Interleukin-6 that were introduced. The error bars in Figure 4.11(B) are generated with $N = 6$ devices and they represent one standard error. This indicates that without the incorporation of the linkers and target-binding aptamers; the target proteins are not able to directly influence the graphene conducting channel.

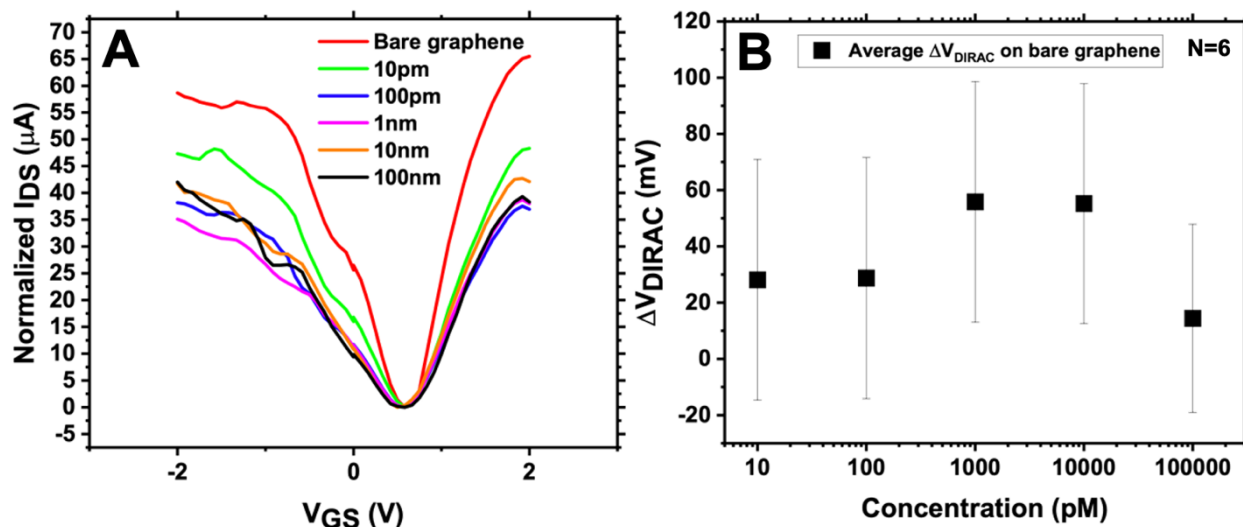


Figure 4.11: IL-6 sensing process performed on Kapton GFET without PBASE and aptamers. (A) GFET transfer characteristic curves with $V_{DS} = 50$ mV; (B) The corresponding calibration curve.

CHAPTER 5: DETECTING BIOMARKER

5.1. OVERVIEW

This chapter details the process of detecting Interleukin-6 (IL-6) using the printable graphene FET biosensor. Two different detection modes were implemented, namely the static voltage sweep method and continuous real-time sensing. The static method of sensing has multiple variations and thus both are discussed. Furthermore, the selectivity of the sensor is discussed along with the limit of detection. The impacts of mechanical stress on the substrate were also characterized during the sensing process in order to ensure consistency across all conditions.

5.2. SENSING THEORY

The goal of the graphene transistor-based biosensor is to characterize the relationship between the concentration of the target analyte IL-6 and the resulting change in Dirac voltage. The conceptual illustration shown below in Figure 5.1 outlines the working principle of the device.

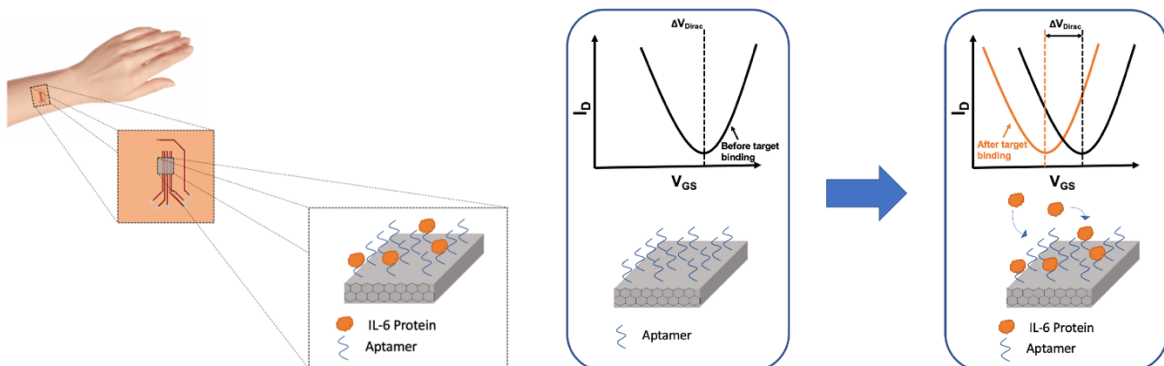


Figure 5.1: Conceptual drawing detailing how protein introduction impacts the sensor behavior, specifically the transfer characteristic curve and resulting Dirac voltage.

The rationale for developing this platform is that the flexible, Kapton-based GFET will be mounted on the user's skin and sweat will be used as the liquid gate for the device, thus creating a non-

invasive way to monitor the user's health conditions. It is anticipated that with different concentrations of target analyte being introduced to the system, multiple different characteristic curves would be generated and thus a change in Dirac voltage that is proportional to the concentration of the analyte would be observed. Finally, instead of sweeping the gate-to-source voltage, which is not feasible for real-time monitoring of the target biomarkers, the gate-to-source voltage will be fixed. By fixing the gate-source voltage, a user can simply monitor changes in the drain-to-source current over time. Therefore, any changes seen in the current are directly related to changes in the target concentration.

5.3. STATIC SENSING

Static sensing is the process of measuring the transfer characteristic curve (I_{DS} versus V_{GS}), of the GFET device for various IL-6 concentrations. The name 'static sensing' is given because during this mode of measurement, the protein is introduced in a droplet form and thus is not moving across the channel as in real-time sensing. This is different from real-time sensing because in this sensing mode it is not possible to monitor the change in the concentration continuously in real-time and gain time-dependent information from the results. The first step in static sensing is to get a baseline measurement of the GFET characteristic curve with no target analyte. This is done after PBASE functionalization and aptamer immobilization. A 180 μ L droplet of 0.01 \times PBS buffer is dropped onto the channel and the characteristic curve is then measured. This measurement is the standard for where the change in Dirac voltage will be measured from. The buffer solution is removed from the GFET channel and multiple concentrations of protein are then introduced one at a time. Beginning with 10 pM, the analyte solution is dropped in a 180 μ L droplet onto the device and incubates for ten minutes to allow the aptamers and proteins to bind together. The analyte solution is then removed and replaced with the 0.01 \times PBS buffer and the GFET transfer

characteristic curve is then measured. The graphene surface is then rinsed with $0.01 \times$ PBS buffer and the next concentration, 100 pM, is then introduced. Five different concentrations of IL-6 will be introduced to the substrate one at a time. After each incubation, the graphene surface is washed with the buffer and the transfer characteristics are measured for each of the five devices that make up the GFET. After measurement, the graphene channel is rinsed using the $0.01 \times$ PBS buffer solution and the new concentration is then dropped, replacing the old protein, and the process is repeated. After each of the six transfer characteristic curves are measured, one baseline and five concentrations, the results are combined into a single normalized graph where the current corresponding to the Dirac voltage for each curve is set to be zero as shown in Figure 5.2(A).

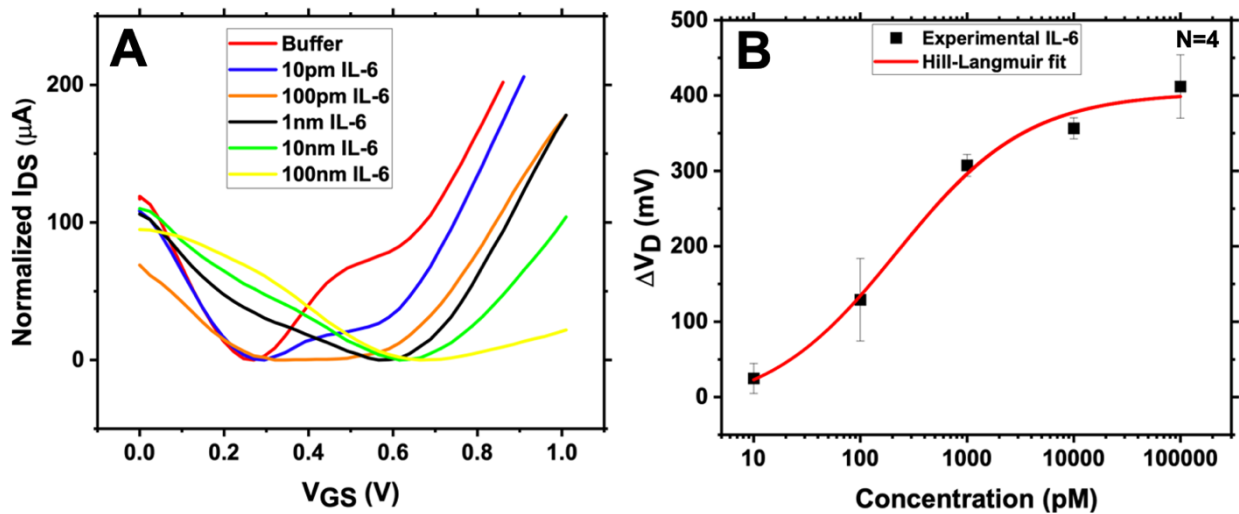


Figure 5.2: IL-6 static sensing with $0.01 \times$ PBS as liquid gate and $V_{DS} = 100$ mV. (A) Normalized transfer characteristic curves showing a right shift in Dirac voltage with respect to concentration; (B) Concentration calibration curve showing the changes in Dirac voltage as a function of concentration with resulting Hill-Langmuir line of best fit ($R^2 = 99.27\%$).

Table 5.1: Average shift in Dirac voltage for IL-6 static sensing with $0.01 \times$ PBS as liquid gate and $V_{DS} = 100$ mV.

	Average shift in Dirac voltage (mV)
10 pM	24.781250
100 pM	129.109250
1 nM	307.383500
10 nM	356.538500
100 nM	411.979000

Normalization makes it clear to see how protein concentration and binding impacts the conduction channel of the device, and specifically the Dirac voltage. Not only is there a shift in the Dirac voltage but the shift is proportional to the concentration of IL-6 protein that was introduced to the device which is displayed in Figure 5.2(B). Figure 5.2(B) is obtained by plotting the change in Dirac voltage from the buffer solution (zero concentration) to the concentration of interest, which are explicitly stated in Table 5.1. The error bars are generated with $N = 4$ devices and they represent one standard error. By simply comparing the change in Dirac voltage as a function of concentration, ideally the data should follow the Hill-Langmuir equation. When the data is plotted it is obvious that it closely follows the Hill-Langmuir equation. IL-6 at a pH of 7.4 is used in all sensing applications. At this pH, IL-6 is negatively charged, and as observed throughout this work, the Dirac voltage shifts to the right. Due to the fact that the PBASE is introduced at such high concentration during functionalization in conjunction with the positively shifting Dirac voltage, it can be concluded that in this application the electrostatic gating effect dominates over the charge transfer doping effect. The results obtained from this method of sensing strongly suggests that the concepts that are being used can be implemented for wearable

applications. If the gate-to-source voltage is fixed, it is possible to monitor the drain-to-source current over time and be able to monitor changes in current instantaneously.

5.3.1. BUFFER LIQUID GATE VS ANALYTE LIQUID GATE

There are multiple approaches for how to conduct static sensing, specifically how the liquid gate solution influences the shift in Dirac voltage. The first method is to introduce the protein to the graphene, incubating for 10 minutes, and then rinse the graphene surface briefly as discussed in Section 5.3. The buffer solution is then dropped onto the graphene and the transfer characteristic curve is measured. This method is simple and eliminates the influence of proteins that are bound nonspecifically but dissociation is present. The moment that the protein is removed from the graphene, it is no longer known if the proteins are attached to the graphene or if dissociation has begun. It is also possible that proteins were removed either during the rinsing process or end up free in the buffer solution.

To remove the uncertainty that is brought upon by the rinsing step, the second method is to apply the protein and, after incubating for 10 minutes, measure the current without rinsing the graphene surface. This process eliminates the question of proteins being washed away or dissociating during the measurement process. However, this process does introduce its own issues to the procedure. By keeping the protein on the device, the issue of nonspecific binding will be present in the measurements. Furthermore, the protein sitting on the device during the measurement process will ensure that the Dirac voltage is being influenced by both specifically and nonspecifically bound proteins. Figure 5.3 shows the results from using the same static sensing procedure as discussed in Section 5.3 but this time without the rinsing step; therefore, the liquid gate is the analyte solution. By using the IL-6 solution as the liquid gate, a much larger shift in the Dirac voltage is observed. This is to be expected because there will always be more proteins

present and therefore bound to the aptamers on the device when the target analyte is present in comparison with only a buffer. In Figure 5.3(A) there is a shift of nearly 1 V from 0 pM to 100 nM which is significantly larger than sensing with buffer as the liquid gate. The error bars represent one standard error and are generated with $N = 4$ devices.

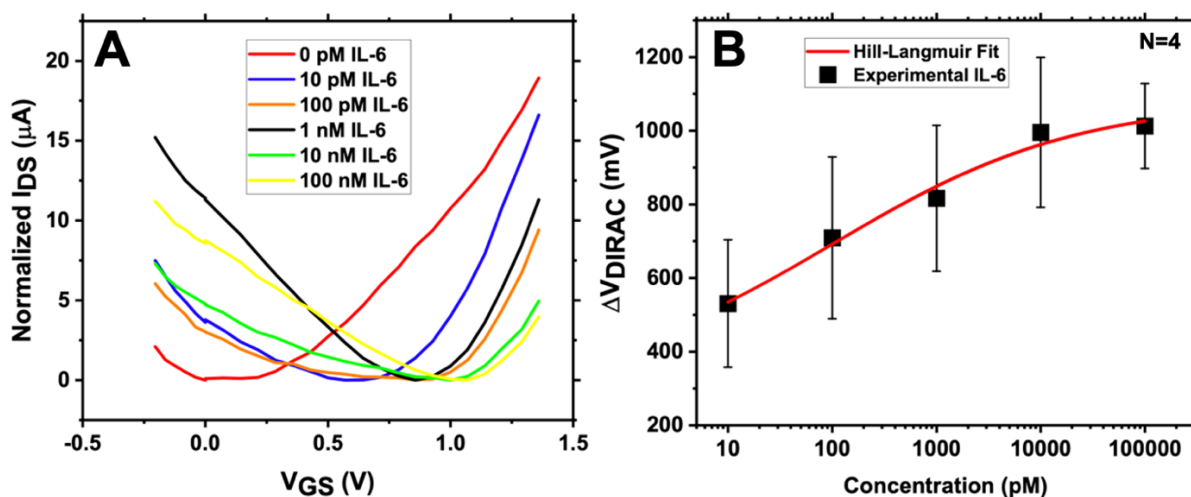
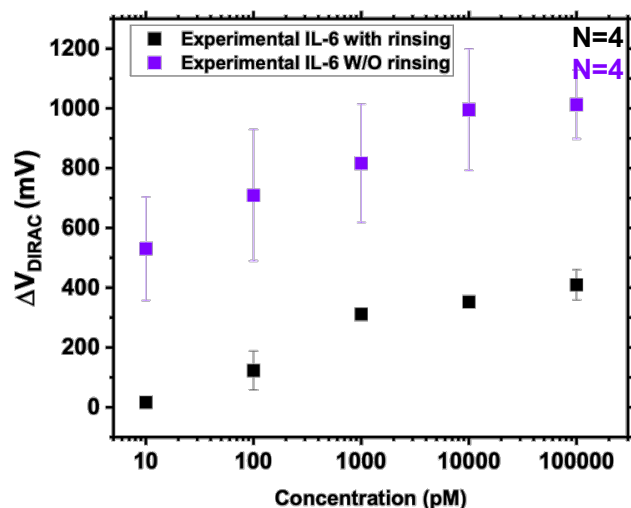


Figure 5.3: IL-6 static sensing with analyte as liquid gate and $V_{\text{DS}} = 10$ mV. (A) Normalized transfer characteristic curves showing a right shift in Dirac voltage with respect to concentration; (B) Concentration calibration curve showing change in Dirac voltage as a function of concentration with resulting Hill-Langmuir line of best fit ($R^2 = 98.37\%$).



	Average shift in Dirac voltage (mV)	
	Rinsing	No Rinsing
10 pM	24.781250	530.612250
100 pM	129.109250	709.168500
1 nM	307.383500	816.320750
10 nM	356.538500	995.505250
100 nM	411.979000	1012.73350

Figure 5.4: (A) IL-6 calibration curve showing change in Dirac voltage as a function of concentration. The black represents experimental data points where there the graphene is rinsed before sensing (liquid gate: $0.01 \times$ PBS buffer) and the purple represents experimental data points where there the graphene is not rinsed before sensing (liquid gate: specified concentration of IL-6 solution); (B) Side by side comparison of rinse (buffer liquid gate) versus no rinse (analyte liquid gate) shift in Dirac voltage as a function of concentration.

Figure 5.4(A) makes a clear comparison between the sensing with the target analyte as the liquid gate and the using a buffer solution as the liquid gate. There is a significantly larger change in Dirac voltage when the IL-6 protein is present in comparison to when there is only a buffer. Specifically shown in Figure 5.4(B), the largest change in Dirac voltage for the rinsing case did not shift as significantly as the smallest change in Dirac voltage for the non-rinsing case. Furthermore, the change for these two cases were 412 mV and 531 mV respectively. Although there is a more substantial shift in Dirac voltage when the IL-6 is used as the liquid gate, there is also much more error introduced to the experiment. The error bars for the $0.01 \times$ PBS buffer liquid gate are created with $N = 4$ devices and the error bars for the target analyte liquid gate are created with $N = 5$ devices. The error bars are significantly larger for the case when the target analyte is used which is not desirable. Moreover, there are arguments that could be made in defense for either one of the two methods presented.

5.3.2. SELECTIVITY AND LIMIT OF DETECTION

The selectivity of a biosensor ensures that the results and data obtained are specific to the target and not due to other possible interfering species. In this work, aptamers were used to enhance the selectivity of the device. Aptamers promote selectivity because they exhibit preferential binding to the target analyte compared to other molecules. This lowers the probability of false readings due to other biomolecules that could interfere with the GFET device. It is important to make sure that even the proteins that are similar in physical structure to the target IL-6 biomarker do not interact with the sensor and cause a shift in the Dirac voltage.

For selectivity testing, the protein tumor necrosis factor alpha (TNF- α) was used. TNF- α is used in this case because structurally it is very similar to Interleuken-6. As TNF- α and IL-6 are both cytokines that are actively present during proinflammatory processes, they often appear in

the body simultaneously which is an example of why selectivity of the device is important. If the device is exclusively monitoring the levels of IL-6 then the presence (or absence) of other proteins, specifically TNF- α in this case, should cause no change in the current-voltage characteristics and therefore no change in the Dirac voltage. As done above in the static sensing of IL-6, five different concentrations of TNF- α will be introduced one at a time to the device, the current-voltage characteristics will be recorded, and the Dirac voltage will be identified. By comparing the calibration curve of the IL-6 measurement with the calibration curve of the TNF- α measurements, there should be a concentration dependent shift with each IL-6 protein and for TNF- α , ideally there should be zero shift for all concentrations that are introduced.

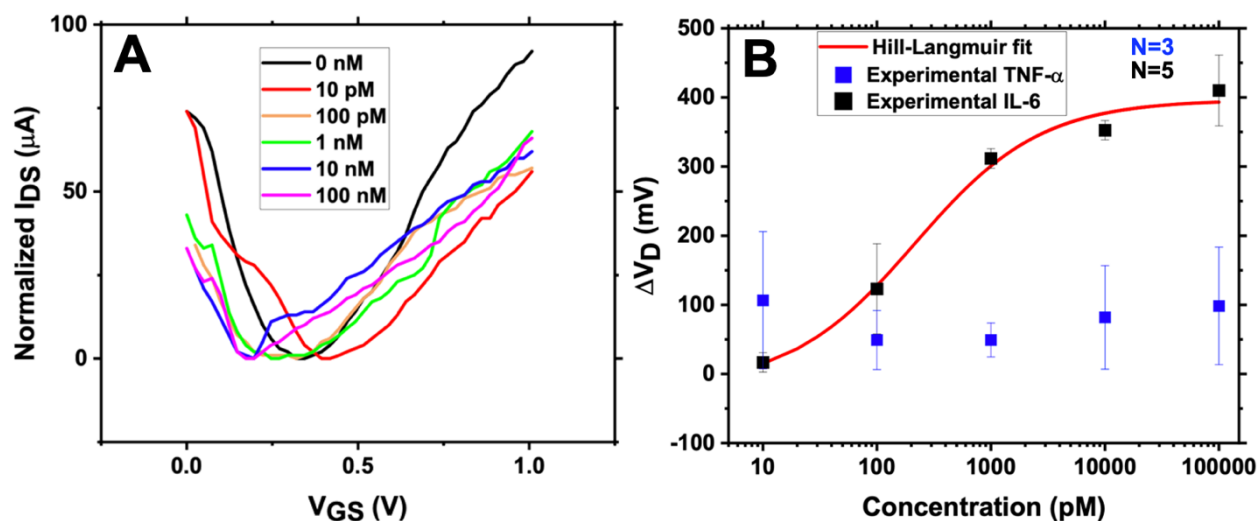


Figure 5.5: TNF- α selectivity static sensing with $0.01 \times$ PBS as liquid gate and $V_{DS} = 100$ mV. (A) Normalized transfer characteristic curves showing concentration independent change in Dirac voltage; (B) Calibration curve showing IL-6 change in Dirac voltage as a function of concentration with resulting Hill-Langmuir line of best fit and TNF- α change in Dirac voltage as a function of concentration.

Table 5.2: Average shift in Dirac voltage for TNF- α selectivity static sensing with $0.01 \times$ PBS as liquid gate and $V_{DS} = 100$ mV.

	Average shift in Dirac voltage (mV)
10 pM	106.580333
100 pM	49.151000
1 nM	49.198000
10 nM	81.943000
100 nM	98.385667

Figure 5.5 summarizes the results from the selectivity testing of the biosensor. While IL-6 does significantly change the Dirac voltage and specifically follows the Hill-Langmuir equation, the TNF- α proves to cause a relatively small shift in Dirac voltage. The average change in Dirac voltage was 106.58 mV, 49.151 mV, 49.198 mV, 81.943 mV, and 98.386 mV for increasing levels of TNF- α as displayed in Table 5.2. These changes, while small in comparison to the shift due to IL-6 introduction, are also random in magnitude. For example, in Figure 5.5(B) the largest shift in Dirac voltage due to TNF- α concentration is at 10 pM and the smallest shift is at 100 pM. Therefore, the shift in Dirac voltage is independent of the concentration of TNF- α that is introduced. These results conclude that the aptamers chosen are highly selective to the Interleukin-6 recombinant mouse protein. The error bars are generated with N = 3 devices and they represent one standard error for the TNF- α data in Figure 5.5(B).

The limit of detection (LoD) is the lowest analyte concentration which is likely to be reliably measured [70]. The limit of detection can be calculated for any given device using the equation presented below [23].

$$\text{Limit of Detection} = \frac{3.3 \times \text{standard deviation at the lowest concentration measured}}{\text{Slope of the calibration curve (at lowest concentration)}}$$

Using this equation, the GFET biosensor can be assessed for what the range of detection will be and the reliability of those results. The limit of detection is measured for both the case where the

liquid gate is the $0.01 \times$ PBS buffer and when the liquid gate is the target analyte. The limit of detection for these two cases are 14.7292 pM and 24.5399 pM respectively.

5.3.3. SENSING UNDER MECHANICAL STRESS

A wearable device needs to be able to withstand material deformations while its performance integrity stays intact. Other Mylar-based biosensors have proven to be able to withstand deformations such as substrate bending [6], [54], twisting, and stretching [10]. It is vital that the wearable sensor results are not impacted if the sensor is bent. While the bending of the substrate with bare graphene was tested to see if there was a resulting shift in Dirac voltage, it is even more crucial to investigate if the trend of the sensing results stands true even when the substrate is bent. The GFET device was placed on a substrate with a radius of 2.25 cm and the static sensing process was repeated as shown in Figure 5.6(A). The target analyte was used as the liquid gate and a drain-to-source voltage of 10 mV.

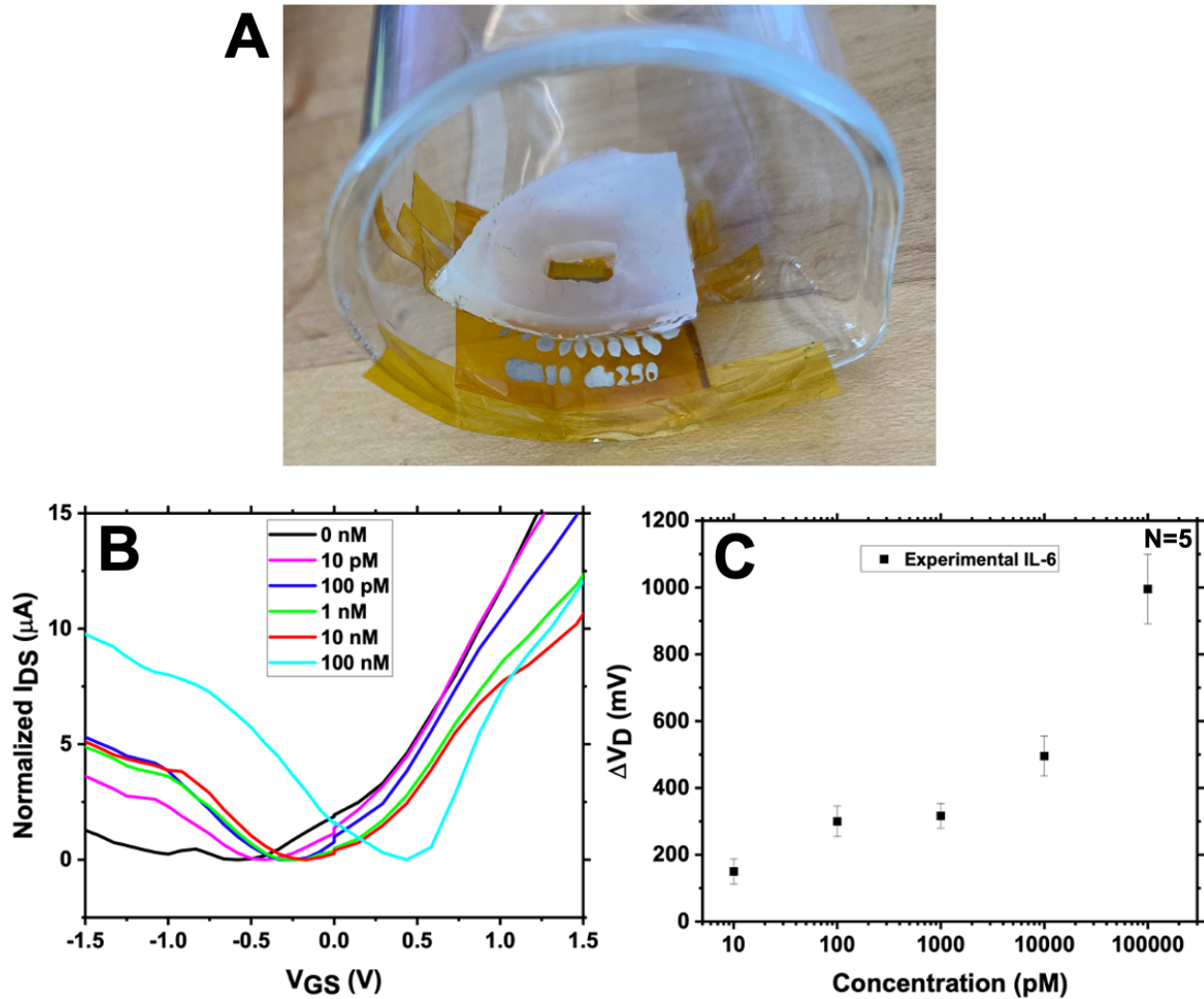


Figure 5.6: (A) k-GFET IL-6 static sensing results while substrate is bent at radius of 2.25 cm and $V_{DS} = 10$ mV; (B) Normalized transfer characteristic curves showing a right shift in Dirac voltage with respect to concentration; (C) Concentration calibration curve showing change in Dirac voltage as a function of concentration.

From Figure 5.6(B) and (C), the conclusion can be drawn that the GFET-based IL-6 sensor still performs reasonably well even under the mechanical stress of bending. Figure 5.6(B) shows the transfer characteristic curves while the device is bent, and it can be seen that the Dirac voltage shifts to the right as the concentration of IL-6 increases. Figure 5.6(C) displays that there is still a distinct change in the Dirac voltage that is proportional to the concentration of IL-6 that is introduced. The error bars are generated with $N = 5$ devices and they represent one standard error.

The results indicate that there is still a significant shift of almost 1 V throughout the duration of the experiment.

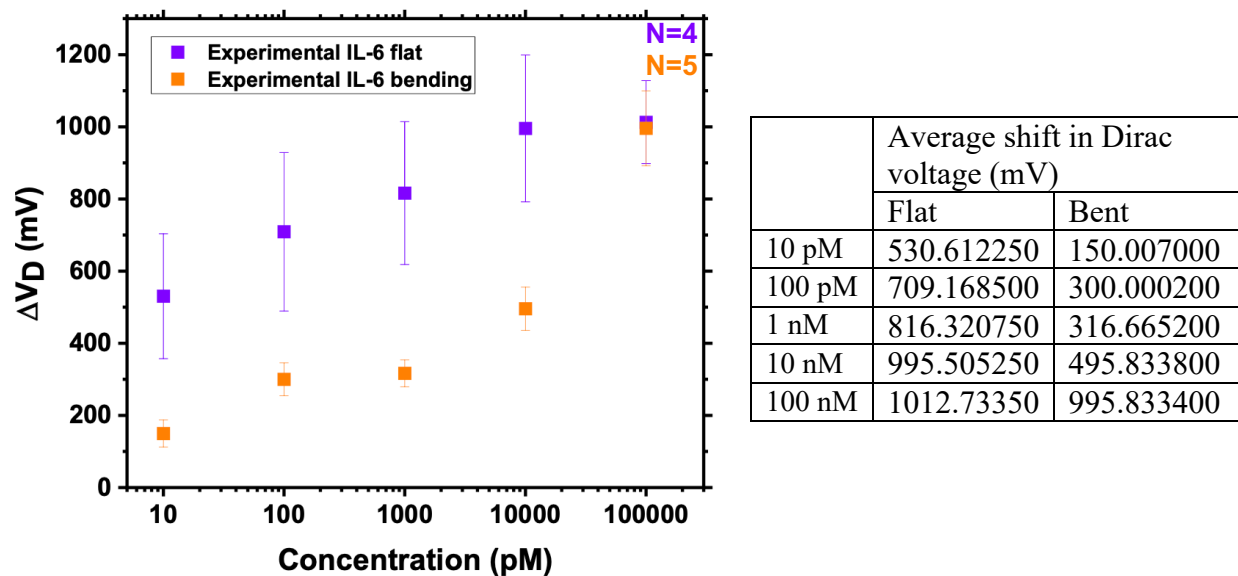


Figure 5.7: (A) Calibration curve with IL-6 sensing done with k-GFET on flat substrate (purple) and on bent substrate (orange); (B) Side by side comparison of flat versus bending shift in Dirac voltage as a function of concentration.

As shown in Figure 5.7(A), although the mechanical stress on the substrate does not cause inconsistencies with the general trend which is displayed during sensing, it does impact the individual changes in Dirac voltage. Figure 5.7(B) displays the average shift in Dirac voltage for each case. The case when the substrate is flat shows over double the shift in Dirac voltage except for at 100 nM where the measurements are almost identical. The error bars are generated with $N = 4$ devices and $N = 5$ devices for the flat and the bending cases, respectively, and they represent one standard error. The Dirac voltage shifts much less in the case when the substrate is bent in comparison to the flat substrate. Therefore, bending does impact the sensor sensitivity and can cause variation in the sensor data.

5.4. REAL-TIME SENSING

Real-time sensing and its implementation are key to the GFET biosensor being widely used in practical applications. Real-time sensing is essential as it will monitor the biomarker continuously through the use of a wearable device. The device is first functionalized in the same way as above, using the droplet method, and then the aptamers are attached. In real-time sensing the gate-to-source voltage is fixed, and the drain current is simply monitored versus time. Due to the relationship between Dirac voltage and concentration, by monitoring the drain current, the concentration of target protein IL-6 present can be determined. During real-time sensing, the gate-to-source voltage is fixed relative to the Dirac voltage. The Dirac voltage is determined after the attachment of PBASE and aptamers using the static method for observing the existing transfer characteristic curve. Once the Dirac voltage is determined, the gate-to-source voltage is chosen appropriately. Moreover, the gate-to-source voltage should be fixed approximately ± 500 mV from the Dirac voltage as it provides sufficient differences in the individual equilibrium currents for each of the target concentrations. In real-time sensing, a microfluidic channel is integrated in order to introduce analyte and buffer solutions continuously.

Microfluidic channels not only allow for the continuous introduction of protein samples, but also provide a plethora of other advantages over other common sensing methods. The droplet-based technique which is used for the static sensing mentioned throughout Section 5.3 is sufficient for initial measurements and proof of concept however, there are inconsistencies that can arise from this method which are effectively eliminated when implementing microfluidics. Evaporation is a common problem with the droplet-based technique. Throughout the static process each droplet incubates on the GFET surface for over 30 minutes. Such extensive time with the droplet sitting static on the device can lead to evaporation of the analyte and subsequent inconsistencies with how

much liquid is present in the liquid gate. By implementing a system like a microfluidic channel, the effects of evaporation are significantly lessened due to the complete enclosure of the liquid along with the slow yet constant flow rate [65].

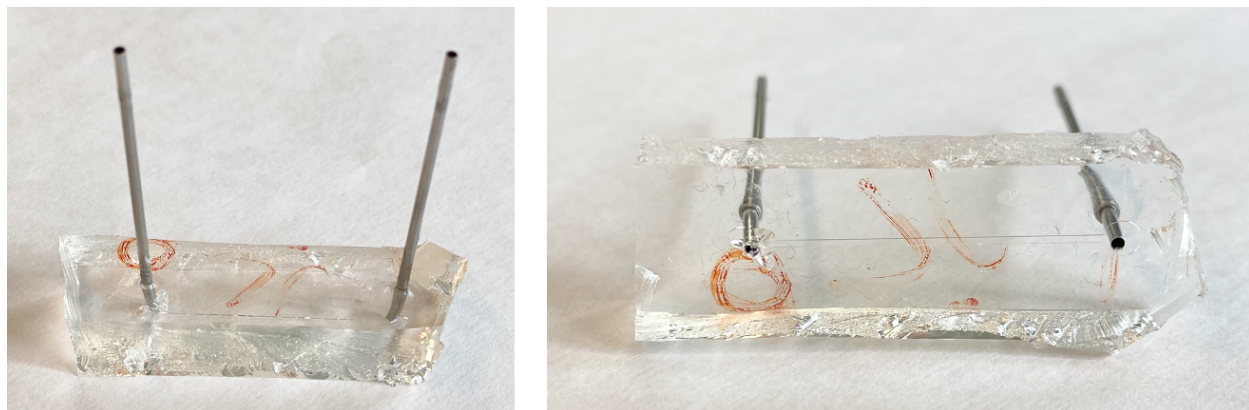


Figure 5.8: Microfluidic channel used in real-time sensing with dimensions of $600\ \mu\text{M}$ width and $100\ \mu\text{M}$ height.

Microfluidics allows for real-time sensing applications to be possible. This is because of the continuous fluid flow across the conduction channel. In this application, a microfluidic channel was fabricated using PDMS and the cast molding technique. The channel used in the application has a width of $600\ \mu\text{M}$ and a height of $100\ \mu\text{M}$. The preparation and method of fabrication of the microfluidic channel is directly outlined in the supplementary material from [23]. The microfluidic channel used in the real-time sensing applications is shown above in Figure 5.8.

The process for real-time sensing of IL-6 is similar to the static measurement process. In the real-time sensing LabVIEW VI, there are far fewer settings including only: compliance current for the maximum drain-source current, the drain-to-source voltage, and the data interval relating to how often samples should be taken. The gate-source voltage is fixed for real-time sensing and the external power supply is used to provide this voltage to the device. Once set up, the real-time monitoring can only track one out of five devices at a time so the most reliable one is selected and will be used for continuous sensing. The difference is that instead of introducing the sample or

buffer in a droplet form, it is introduced in the microfluidic channel and flowed through using a PHD Ultra syringe pump by Harvard Apparatus. The current is then monitored versus time and trends begin to form. Ideal measurements for the real-time sensing would look like the results drawn below in Figure 5.9.

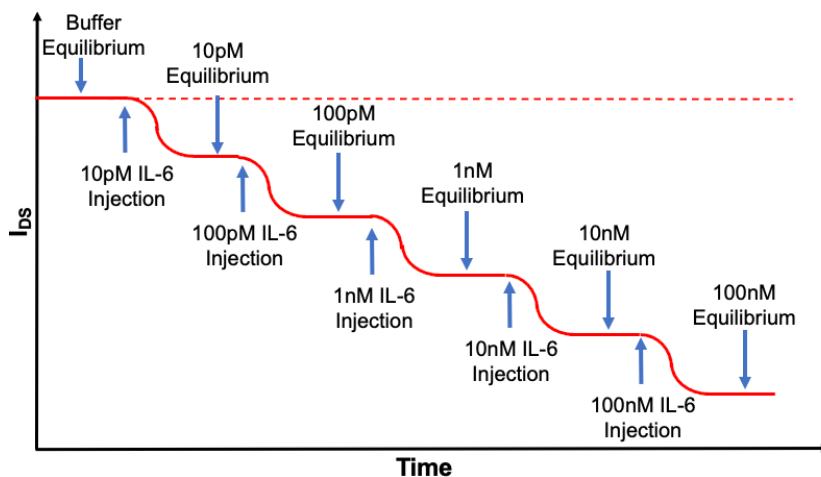


Figure 5.9: Ideal I_{DS} versus time graph with increasing protein concentration injections.

The model response for real-time measurements would begin with a buffer solution that is introduced to the system. The buffer continues to flow at a constant rate until an equilibrium current is reached. Once the equilibrium is reached and identified, the first concentration of Interleukin-6 is introduced. When the first concentration is introduced, which is 10 picomolar in this case, the current will drop quite rapidly once the proteins begin binding with the aptamers. Eventually the current will reach a new equilibrium current that is consistent with the new state of the device. After the new equilibrium current is reached, the same process will be followed again as the next highest concentration of IL-6 will be introduced until the next equilibrium current is reached. As each new concentration is introduced and each new equilibrium current is identified, the trend should follow the same as the static measurements, meaning that with increasing

concentrations of IL-6 introduced, there should be a proportional drop in equilibrium current of the device over time.

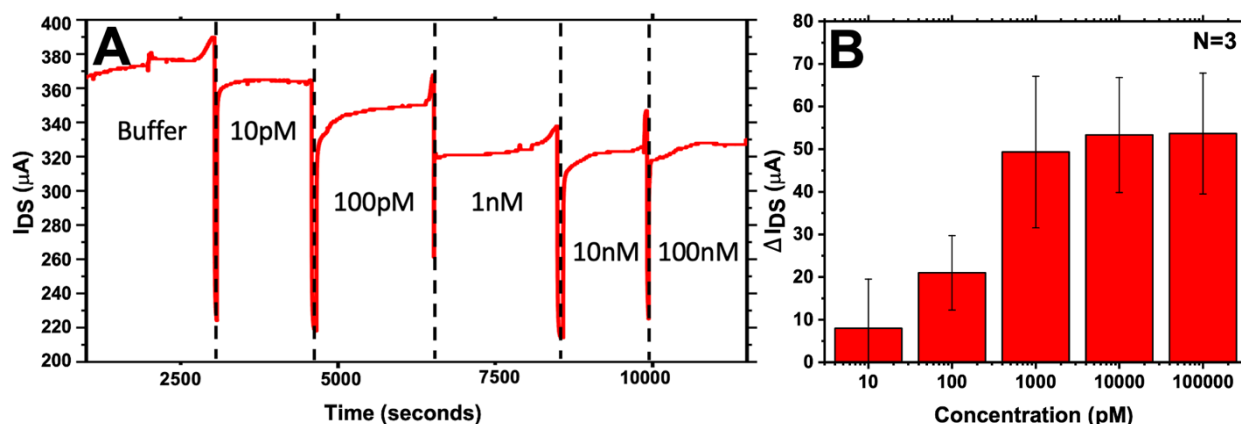


Figure 5.10: Real-time measurements. (A) I_{DS} versus time with various IL-6 injections; (B) Change in I_{DS} with respect to concentration.

It is observed during real-time sensing that the trend seen during static sensing holds true as exemplified in Figure 5.10. When a concentration of Interleukin-6 is introduced to the device, the current drops in response as predicted in the ideal scenario. When the next concentration of IL-6 is flowed, the same response is seen as more IL-6 proteins bind to the available aptamers on the graphene surface. Consistent with the results from static sensing, with the gate-to-source voltage fixed on the right side of the Dirac voltage, the current drops with each continuous injection of IL-6 as outlined in Figure 5.10(A). Figure 5.10(B) displays the average change in drain-to-source current during sensing for three devices. Figure 5.10(B) is generated by taking the difference in the buffer solution equilibrium current and the equilibrium current for each of the specified concentrations and plotting each against the concentration. The results are again consistent with the data presented in the static sensing section as with increasing concentration there is a proportional increase in the change in drain-to-source current that is recorded.

5.5. IMPLEMENTATION OF INTEGRATED CURRENT MEASUREMENT PLATFORM

In order for the biosensor to be a wearable device, the bulky source measurement unit, power supply, micromanipulator, and computer with the LabVIEW program must be removed from the design and replaced with a much smaller and portable device containing a power supply and the electrical measurement system. The miniature device was designed and implemented by Professor Md. Shaad Mahmud's research group at the University of New Hampshire, and it is able to measure the drain-to-source current in a small and compact design as shown in Figure 5.11.

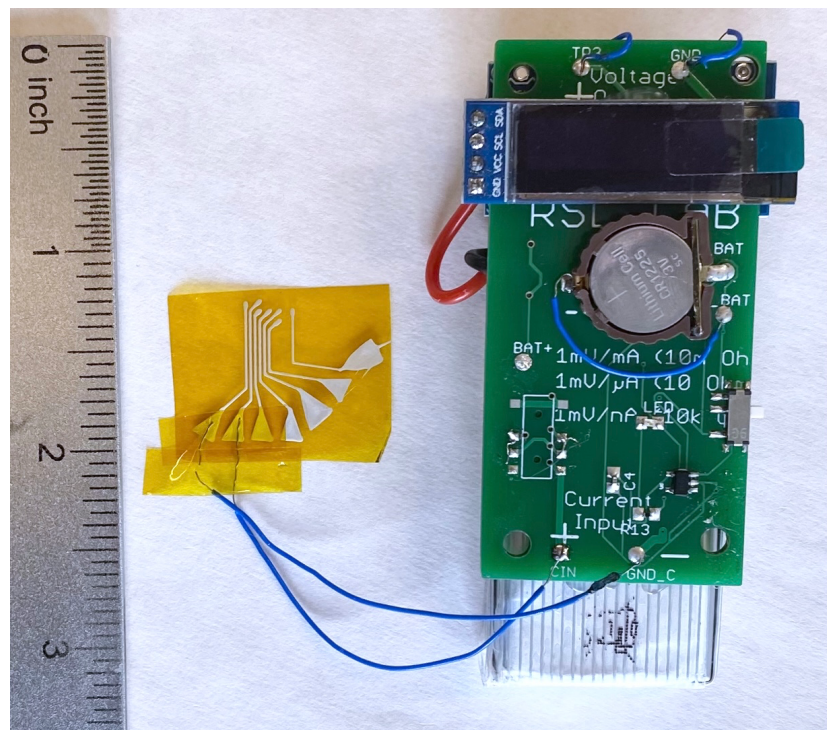


Figure 5.11: The k-GFET sensor shown with the integrated current measurement platform developed by Prof. Md. Shaad Mahmud's group.

One of the major problems when measuring a low voltage current in the micro or nano ampere range is burden voltage. Burden voltage is the voltage drop across a shunt resistor as current passes through. This can result in significant loss of resolution and accuracy. Prof. Mahmud's group

developed a custom made analog front end (AFE) using ultra-low offset ($<50\mu\text{V}$), low noise precision amplifier ($< -90\text{dBV}$). The AFE is operated with zero bias voltage, to continually correct for the DC offset voltage of the main amplifier. Afterward, the signal is fed into a 24-bit analog to digital converter with digital filtering. The output data rate is programmable, with the slowest speed (4.17 Hz) giving the lowest noise of 40 nV, which is negligible compared to other sources of noise. The device operates by simply recording the drain-to-source current overtime and taking samples every 500 msec. This portable measuring system records the data and currently sends it to a laptop computer via a USB cable. The first implementation of the wearable device was created on a rigid PCB substrate. The initial measurements are done to ensure integration is possible and that the device works as anticipated when paired with the GFET biosensor.

When implementing an integrated current measurement platform to the k-GFET device, it is vital that the data measured in this integrated platform closely matches that obtained with the Keysight source measure unit. In order to validate that the on-device measurement system is accurate, measurements of a k-GFET device were taken using the traditional method of the Keysight source measure unit and LabVIEW program at the same time as using the new integrated device. Because the devices are both measuring the drain-to-source current, the devices are simply connected in series at the source terminal. The two were then compared in order to ensure that they matched closely enough to conclude that it was working properly. Characterizations were obtained using an external voltage supply to the device while both the integrated platform and external measurement system recorded the drain-to-source current while the gate-to-source voltage was swept. Three FETs were characterized for three individual k-GFET devices giving a set of nine total measurements. As can be seen below in Figure 5.12, the current measured by the on-device

platform matches very closely to the measurements obtained with the Keysight instrument in connection with the LabVIEW program.

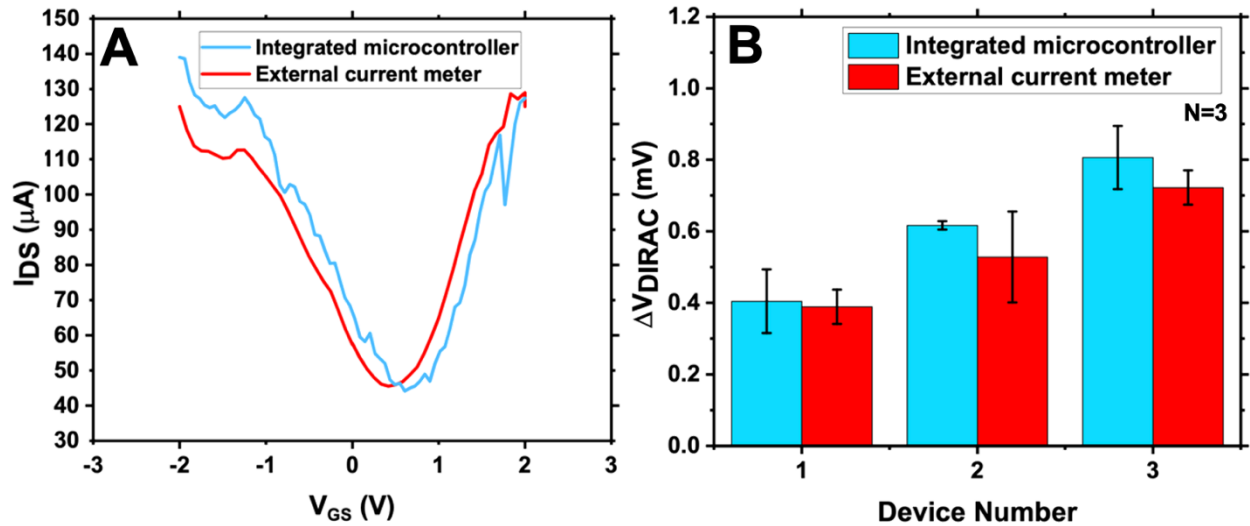


Figure 5.12: Comparison of integrated microcontroller measurements versus external current meter. (A) I_{DS} versus V_{GS} transfer characteristic curve; (B) Dirac voltage location with $N = 3$ reps per device.

Figure 5.12(A) displays one of the characterizations shown with both the integrated microcontroller and external current meter, that best displays the common differences between the two measuring systems. As shown in Figure 5.12(B), the Dirac voltage is very similar in when comparing all three devices. The integrated microcontroller, in all three cases, measured a Dirac voltage about 100 mV higher than the external current meter. Similar to Figure 5.12(A), Figure 5.12(B) also displays a small rightward shift in the case when the integrated microcontroller is used. The integrated controller also has a small offset in terms of the drain-to-source current that was measured. Finally, the integrated microcontroller does have a slightly higher noise and variation in the measurement compared to the conventional setup.

5.6. CHARACTERIZATION TECHNIQUES AND MEASUREMENT SETUP

Measurements for both static and real-time measurements were collected using a Micromanipulator (450 PM-B) probing station in combination with a Keysight precision source/measure unit (B2902A) and National Instruments LabVIEW FET measurement programs. LabView is a graphical programming language created by National instruments which allows for the creation of VIs or virtual instruments that can control a variety of different lab equipment. For this research two independent VIs were used; one for static measurements which swept the gate-to-source voltage and records the corresponding drain currents and another for real-time sensing which records the drain current over time. In the static VI, there are multiple different settings and choices to make before running the VI. The drain voltage must be set, the maximum and minimum sweeping voltage, compliance currents as well as the number of steps that the voltage will be swept in. For static measurements, the gate-to-source voltage was swept to a range dependent on the location of the Dirac voltage. In the majority of cases, the gate-to-source voltage was swept from -2 V to 3.5 V. The liquid gate in all scenarios consists of a liquid droplet of 180 μL and to ensure consistency an eco-flex rubber well was mounted to each device to contain the droplet. The leakage current at the gate electrode was monitored during all static sensing and remained less than 6 μA , 3 μA , and 0.9 μA for the bare graphene measurements, buffer liquid gate sensing, and analyte liquid gate sensing respectively. The leakage is considered negligible as the magnitude of the drain-to-source current in these applications were more than 50 times higher than each of the respective leakage currents.

The real-time measurements also utilize a GW Instek laboratory DC power supply, a 600 μm by 100 μm polydimethylsiloxane (PDMS) microfluidic channel, and a PHD Ultra syringe pump by Harvard Apparatus. For real-time measurements the gate-to-source voltage is set

dependent on the location of the Dirac voltage. It is set to approximately 1.3 V in this application along with the drain-to-source voltage set to 100 mV. The flow rate is set to 20 μL and each concentration is exposed to the graphene nano sensor for 45 minutes.

CHAPTER 6: CONCLUSION

In this work, the feasibility of a GFET-based wearable and flexible biosensor is investigated. The printable GFET device presented in this work is novel and opens the doors for low cost and easy fabrication of wearable biosensors. Using the Voltera V-One PCB printer for fabrication of a biosensor has been demonstrated in this work for the first time. This work has displayed the successful detection of Interleukin-6 using the printed k-GFET platform in both static and real-time measurements. The device is proven to be selective to the IL-6 target protein and shows a high tolerance to mechanical stress on the substrate. Finally, the k-GFET platform can easily be integrated with other miniaturized electronic components for current measurement. By incorporating the GFET-based biosensor with the integrated current measurement platform, the proposed device technology is just one step closer to being a truly wearable, stand-alone GFET-based biosensor.

FUTURE WORK

Although the basic implementation and feasibility have been demonstrated in this work, further research and development are needed before this technology can be used in real world applications. The integrated platform for measuring the current through the device is currently still being fabricated on a rigid PCB substrate. In the future, the integrated platform will be created on the same bendable Kapton substrate that the GFET biosensor is fabricated on. Furthermore, the integrated platform will conveniently send the measured data to the user's smartphone application via wireless Bluetooth connection for easy monitoring. This will allow the data to be available at the touch of a button, and therefore the measurements and the health information will be accessible

to the user at any time. Future work will also include creating a portable way to supply two individual voltages to the GFET platform, namely the drain-to-source voltage and the gate-to-source voltage. By fabricating the GFET, the power supply, and the current measurement system all on the same substrate, each component of the platform could be seamlessly integrated. With a unit that can supply voltages and measure currents worked into the device, the source/measure unit, the power supply, the desktop computer with LabVIEW program, and the Micromanipulator can be removed from the design and thus a compact and truly wearable system can be realized.

Possible work in the future will be extending this work into the field of stretchable electronics as the Dycotec ink for printing is bendable and stretchable. With a stretchable platform, the device could be fabricated on a stretchable substrate such as PDMS. Thus far, there has been little development on GFETs directly fabricated onto a PDMS substrate and therefore such work could lead to a new and innovative device platform.

Static measurements are vital to the beginning stages of research as it provides a proof of concept and the building blocks for the remainder of the work to be done including real-time sensing. Therefore, the static measurement LabVIEW program needs to be modified moving forward. The program, regardless of sweeping range, begins at 0 volts, sweeps to the maximum voltage in the half of the number of steps specified, then sweeps back to zero again in the other half of the number of steps, then from 0 to the minimum voltage and then back again. Because the program runs this way, it results in both a forward sweep and a backward sweep. The forward sweep is defined from the minimum voltage swept to the maximum voltage and the backward sweep is defined as the maximum voltage swept to the minimum voltage. For analysis however, we choose the backward sweep as in the way the program is currently defined it is continuous, where the forward sweep is broken into two parts as can be seen in Figure 6.1 below.

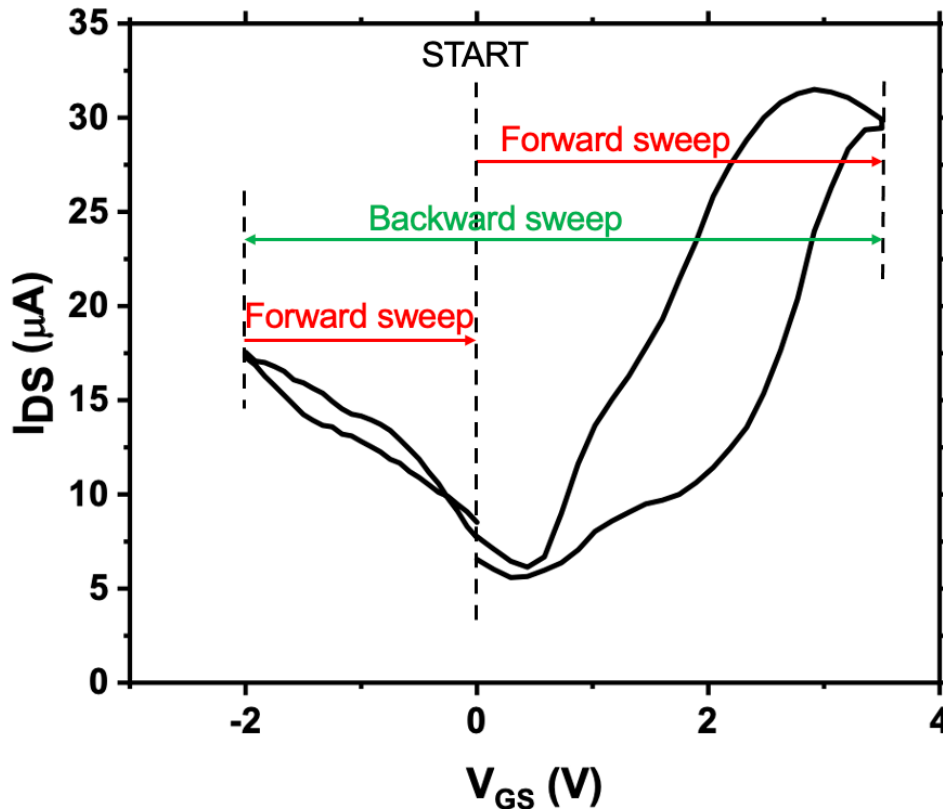


Figure 6.1: Full sweep from LabVIEW showing full backward sweep and two-part forward sweep.

In addition to the issue of a broken forward sweep, the program also does not evenly divide the number of steps across the entire sweeping voltage range but instead allots half of the steps of each sweep for above zero volts and half of the steps in each sweep for below zero volts. This can cause inconsistency as the step size can vary on either side of the sweep if the maximum and minimum sweeping values do not have the same absolute value.

Future work should also include a system in which truly identical GFET devices can be printed each time using the Voltera. When the devices are made, there is a large amount of human interaction and human dependency. During the Voltera printing of the device, while the pattern is identical each time, there is very little control over how thick or thin the line traces truly are. While KiCAD does allow for the line width to be selected, once Voltera begins to print it, there is a level

of uncertainty as the ink flow rate, printing speed, and printing height are all able to be controlled by the user and could result in differences. After printing of the device, the graphene is transferred onto the substrate. This is another place where there can be a small level of inconsistency device to device. The graphene comes in 1 cm-by-1 cm square films. This film is then cut into four approximately even sub-squares and one square is used per device. This can cause the graphene shapes to vary slightly. When the graphene is transferred onto the device itself it is also impossible to get the graphene to fall in the same place on the electrodes each time. With all these factors considered, currently there is still a high yield rate for the devices at approximately 75% of devices working with feasible Dirac voltages. With such promising results now, further advancements in reliability and wearability could make the proposed printed and fabricated GFET-based biosensors a technology of the future in the field of wearable health diagnostic platforms.

REFERENCES

- [1] Cai, B., Wang, S., *et al.* “Ultrasensitive Label-Free Detection of PNA-DNA Hybridization by Reduced Graphene Oxide Field-Effect Transistor Biosensor.” *ACS Nano* 2014 8 (3), 2632-2638 DOI: 10.1021/nm4063424
- [2] Das, Tanmoy, *et al.* “Graphene-Based Flexible and Wearable Electronics.” *Journal of Semiconductors*, vol. 39, no. 1, Jan. 2018.
- [3] de la Fuente, Jesus. “Properties of Graphene.” *Graphenea*, Graphenea, www.graphenea.com/pages/graphene-properties
- [4] Ghosh S, Khan NI, Tsavalas JG, Song E. “Selective Detection of Lysozyme Biomarker Utilizing Large Area Chemical Vapor Deposition-Grown Graphene-Based Field-Effect Transistor.” *Front Bioeng Biotechnol.* 2018 Mar 22;6:29. doi: 10.3389/fbioe.2018.00029. PMID: 29662878; PMCID: PMC5890177.
- [5] “Graphenea Monolayer Graphene Film ‘Easy Transfer.’” Mass., Cambridge, 2021. https://cdn.shopify.com/s/files/1/0191/2296/files/Graphenea_Easy_Transfer_Instructions_20210126.pdf?v=1611681633
- [6] Hao, Zhuang, *et al.* “Measurement of Cytokine Biomarkers Using an Aptamer-Based Affinity Graphene Nano Sensor on a Flexible Substrate toward Wearable Applications.” *Nanoscale*, Oct. 2018, pp. 21681–21688., doi:10.1039/c8nr04315a
- [7] Park YJ, Lee SK, Kim MS, Kim H, Ahn JH. "Graphene-based conformal devices." *ACS Nano.* 2014 Aug 26;8(8):7655-62. doi: 10.1021/nm503446f. Epub 2014 Aug 5. PMID: 25073058.
- [8] Gerald J. Kost, Nam K. Tran, and Richard F. Louie, *Encyclopedia of Analytical Chemistry*, (2008).
- [9] C. P. Price, *Br. Med. J.*, 322, 1285 (2001).
- [10] Wang, Ziran, *et al.* “An Ultraflexible and Stretchable Aptameric Graphene Nanosensor for Biomarker Detection and Monitoring.” *Advanced Functional Materials*, vol. 29, no. 44, 1 Nov. 2019.
- [11] Vainer, Noomi, *et al.* “Systematic Literature Review of IL-6 as a Biomarker or Treatment Target in Patients with Gastric, Bile Duct, Pancreatic and Colorectal Cancer.” *Oncotarget*, vol. 9, no. 51, 3 July 2018, pp. 29820–29841., doi:10.18632/oncotarget.25661.

- [12] J. Xia, F. Chen, J. Li, and N. Tao, “Measurement of the quantum capacitance of graphene,” *Nat. Nanotechnol.*, vol. 4, no. 8, Art. no. 8, Aug. 2009.
- [13] Syu, Yu-Cheng, et al. “Review—Field-Effect Transistor Biosensing: Devices and Clinical Applications.” *ECS Journal of Solid State Science and Technology*, vol. 7, no. 7, 13 June 2018, doi:10.1149/2.0291807jss.
- [14] “Global Health - Newsroom - Tuberculosis.” *Centers for Disease Control and Prevention*, Centers for Disease Control and Prevention, 6 Apr. 2020, www.cdc.gov/globalhealth/newsroom/topics/tb/index.html.
- [15] “Early Detection of Breast Cancer Information.” *MyVMC*, 31 Oct. 2018, www.myvmc.com/investigations/early-detection-of-breast-cancer/.
- [16] Chen, R. J., Zhang, Y., Wang, D., and Dai, H. (2001). Noncovalent sidewall functionalization of single-walled carbon nanotubes for protein immobilization. *J. Am. Chem. Soc.* 123, 3838–3839. doi:10.1021/ja010172b.
- [17] Impak. “What Is Mylar?” *SorbentSystems*, IMPAK, 2017, www.sorbentsystems.com/mylarinfo.html.
- [18] “DuPont™ Kapton® Polyimide Films.” *Dupont Electronic Solutions*, Dupont, 2021, www.dupont.com/electronic-materials/kapton-polyimide-film.html.
- [19] “Interleukin-6.” *Myriad*, Rules-Based Medicine, 2021, myriadrbm.com/products-services/biomarker-detail/?AnalyteID=1448/.
- [20] Z. Gao *et al.*, “Scalable Production of Sensor Arrays Based on High-Mobility Hybrid Graphene Field Effect Transistors,” *ACS Appl. Mater. Interfaces*, vol. 8, no. 41, pp. 27546–27552, Oct. 2016.
- [21] Santa Cruz, André, et al. “Interleukin-6 Is a Biomarker for the Development of Fatal Severe Acute Respiratory Syndrome Coronavirus 2 Pneumonia.” *Frontiers in Immunology*, vol. 12, 18 Feb. 2021, doi:10.3389/fimmu.2021.613422.
- [22] M. B. Lerner *et al.*, “Scalable Production of Highly Sensitive Nanosensors Based on Graphene Functionalized with a Designed G Protein-Coupled Receptor,” *Nano Lett.*, vol. 14, no. 5, pp. 2709–2714, May 2014.
- [23] Khan, Niazul I., et al. “An Integrated Microfluidic Platform for Selective and Real-Time Detection of Thrombin Biomarkers Using a Graphene FET.” *The Analyst*, vol. 145, no. 13, 6 May 2020, pp. 4494–4503., doi:10.1039/d0an00251h.
- [24] Henri, Justin, et al. “A Guide to Using Nucleic Acid Aptamers in Cell Based Assays.” *International Society on Aptamers*, 23 Nov. 2019, aptamersociety.org/breaking-news/a-guide-to-using-nucleic-acid-aptamers-in-cell-based-assays/.

- [25] Shukla, S.K., et al. “Polymeric Micellar Structures for Biosensor Technology.” *Advances in Biomembranes and Lipid Self-Assembly*, 2016, pp. 143–161., doi:10.1016/bs.abl.2016.04.005.
- [26] Nandanapalli, Koteswara Reddy, et al. “Functionalization of Graphene Layers and Advancements in Device Applications.” *Carbon*, vol. 152, 28 June 2019, pp. 954–985., doi:10.1016/j.carbon.2019.06.081.
- [27] Benihoud, K, et al. “Respective Roles of TNF- α and IL-6 in the Immune Response-Elicited by Adenovirus-Mediated Gene Transfer in Mice.” *Gene Therapy*, vol. 14, no. 6, 16 Nov. 2006, pp. 533–544., doi:10.1038/sj.gt.3302885.
- [28] Park, Jeho, et al. “Applications of Field-Effect Transistor (FET)-Type Biosensors.” *Applied Science and Convergence Technology*, vol. 23, no. 2, 30 Mar. 2014, pp. 61–71., doi:10.5757/asct.2014.23.2.61.
- [29] Qiao, Yancong, et al. “Graphene-Based Wearable Sensors.” *Nanoscale*, vol. 11, no. 41, 29 Aug. 2019, pp. 18923–18945., doi:10.1039/c9nr05532k.
- [30] Song, Shiping, et al. “Aptamer-Based Biosensors.” *TrAC Trends in Analytical Chemistry*, vol. 27, no. 2, 2008, pp. 108–117., doi:10.1016/j.trac.2007.12.004.
- [31] S. Tombelli, M. Minunni, M. Mascini, *Biomol. Eng.* 24 (2007) 191.
- [32] T. Hermann, D.J. Patel. *Science* (Washington, D. C.) 287 (2000) 820.
- [33] R.D. Jenison, S.C. Gill, A. Pardi, B. Polisky *Science* (Washington, D. C.), 263 (1994), p. 1425
- [34] A. Geiger, P. Burgstaller, H. von der Eltz, A. Roeder, M. Famulok *Nucleic Acids Res.*, 24 (1996), p. 1029
- [35] Iliuk, Anton B., et al. “Aptamer in Bioanalytical Applications.” *Analytical Chemistry*, vol. 83, no. 12, 2011, pp. 4440–4452., doi:10.1021/ac201057w.
- [36] BasePair Biotechnologies, Inc. “IL-6 Aptamer Data Sheet.” Pearland, Texas, 18 May 2021.
- [37] Lee, S.-K.; Kim, B. J.; Jang, H.; Yoon, S. C.; Lee, C.; Hong, B. H.; Rogers, J. A.; Cho, J. H.; Ahn, J.-H. Stretchable Graphene Transistors with Printed Dielectrics and Gate Electrodes. *Nano Lett.* 2011, 11, 4642–4646.
- [38] Lee, S.-K.; Jang, H. Y.; Jang, S.; Choi, E.; Hong, B. H.; Lee, J.; Park, S.; Ahn, J.-H. All Graphene-Based Thin Film Transistors on Flexible Plastic Substrates. *Nano Lett.* 2012, 12, 3472–3476.

- [39] Kohonen, Mika M., et al. "Debye Length in Multivalent Electrolyte Solutions." *Langmuir*, vol. 16, no. 13, 20 Mar. 2000, pp. 5749–5753., doi:10.1021/la991621c.
- [40] Yan, Chao, et al. "Graphene-Based Flexible and Stretchable Thin Film Transistors." *Nanoscale*, vol. 4, no. 16, 24 May 2012, p. 4870., doi:10.1039/c2nr30994g.
- [41] Chen, Maggie Y., et al. "Inkjet Printed Graphene-Based Field-Effect Transistors on Flexible Substrate." *Low-Dimensional Materials and Devices 2017*, 25 Aug. 2017, doi:10.1117/12.2280039.
- [42] Khan, Md Niazul Islam, "Nanoelectronic Devices for Sensitive Detection of Biomarkers in Healthcare Monitoring" (2021). Doctoral Dissertations. 2577.
- [43] Castro Neto, A. H., et al. "The Electronic Properties of Graphene." *Reviews of Modern Physics*, vol. 81, no. 1, 14 Jan. 2009, pp. 109–162., doi:10.1103/revmodphys.81.109.
- [44] N. Chauhan, T. Maekawa, and D. N. S. Kumar, "Graphene based biosensors—Accelerating medical diagnostics to new-dimensions," *J. Mater. Res.*, vol. 32, no. 15, pp. 2860–2882, Aug. 2017.
- [45] Velazquez-Salinas, Lauro, et al. "The Role of Interleukin 6 During Viral Infections." *Frontiers in Microbiology*, vol. 10, 10 May 2019, doi:10.3389/fmicb.2019.01057.
- [46] Guo Y, Xu F, Lu T, Duan Z, Zhang Z. Interleukin-6 signaling pathway in targeted therapy for cancer. *Cancer Treat Rev.* 2012; 38:904–910.
- [47] Lippitz BE, Harris RA. Cytokine patterns in cancer patients: a review of the correlation between Interleukin 6 and prognosis. *Oncoimmunology.* 2016; 5:1093722.
- [48] Ferlay J, Soerjomataram I, Dikshit R, Eser S, Mathers C, Rebelo M, Parkin DM, Forman D, Bray F. Cancer incidence and mortality worldwide: sources, methods and major patterns in GLOBOCAN 2012. *Int J Cancer.* 2015; 136:e359–386.
- [49] Johnson DE, O’Keefe RA, Grandis JR. Targeting the IL-6/ JAK/STAT3 signaling axis in cancer. *Nat Rev Clin Oncol.* 2018; 15:234–48.
- [50] Koca YS, Bulbul M, Barut I. The Diagnostic Roles of Cytokines in Hepatobiliary Cancers. *Biomed Res Int.* 2017; 2017: 2979307.
- [51] Koscielny, Maurice Tubiana. "The Rationale for Early Diagnosis of Cancer: The Example of Breast Cancer." *Acta Oncologica*, vol. 38, no. 3, 8 July 1999, pp. 295–303., doi:10.1080/028418699431357.
- [52] Ulrich, H.; Martins, A.H.; Pesquero, J.B. RNA and DNA aptamers in cytomics analysis. *Cytom. A* 2004, 59, 220–231.

- [53] Roy, Dhruvajyoti, et al. “The Potential of Aptamer-Mediated Liquid Biopsy for Early Detection of Cancer.” *International Journal of Molecular Sciences*, vol. 22, no. 11, 25 May 2021, p. 5601., doi:10.3390/ijms22115601.
- [54] Huang, Cong, et al. “An Integrated Flexible and Reusable Graphene Field Effect Transistor Nanosensor for Monitoring Glucose.” *Journal of Materiomics*, vol. 6, no. 2, 5 Feb. 2020, pp. 308–314., doi:10.1016/j.jmat.2020.02.002.
- [55] Liang, Yiran, et al. “High Mobility Flexible Graphene Field-Effect Transistors and Ambipolar Radio-Frequency Circuits.” *Nanoscale*, vol. 7, no. 25, 28 May 2015, pp. 10954–10962., doi:10.1039/c5nr02292d.
- [56] “Plasma Modified Polymeric Materials for Biosensors/Biodevice Applications.” *Non-Thermal Plasma Technology for Polymeric Materials: Applications in Composites, Nanostructured Materials, and Biomedical Fields*, by Sabu Thomas et al., Elsevier, 2019, pp. 409–437.
- [57] Jang, H.; Lee, W.; Won, S. M.; Ryu, S. Y.; Lee, D.; Koo, J. B.; Ahn, S.-D.; Yang, C.-W.; Jo, M. H.; Cho, J. H.; et al. Quantum Confinement Effects in Transferrable Silicon Nanomembranes and Their Applications on Unusual Substrates. *Nano Lett.* 2013, 13, 5600–5607.
- [58] Wang, Ziran, et al. “A Wearable and Deformable Graphene-Based Affinity Nanosensor for Monitoring of Cytokines in Biofluids.” *Nanomaterials*, vol. 10, no. 8, 31 July 2020, p. 1503., doi:10.3390/nano10081503.
- [59] Bhansali, Shekhar, and Abhay Vasudev. *MEMS for Biomedical Applications*. Woodhead Pub., 2012.
- [60] Wu, Shuying, et al. “Novel Electrically Conductive Porous PDMS/Carbon Nanofiber Composites for Deformable Strain Sensors and Conductors.” *ACS Applied Materials & Interfaces*, vol. 9, no. 16, 17 Jan. 2017, pp. 14207–14215., doi:10.1021/acsami.7b00847.
- [61] Matsuhisa, Naoji, et al. “Printable Elastic Conductors by in Situ Formation of Silver Nanoparticles from Silver Flakes.” *Nature Materials*, vol. 16, no. 8, 15 May 2017, pp. 834–840., doi:10.1038/nmat4904.
- [62] Liu, Chao-Xuan, and Jin-Woo Choi. “Analyzing Resistance Response of Embedded PDMS and Carbon Nanotubes Composite under Tensile Strain.” *Microelectronic Engineering*, vol. 117, 2014, pp. 1–7., doi:10.1016/j.mee.2013.11.013.
- [63] Z. Hao et al., “Real-Time Monitoring of Insulin Using a Graphene Field-Effect Transistor Aptameric Nanosensor,” *ACS Appl. Mater. Interfaces*, vol. 9, no. 33, pp. 27504–27511, Aug. 2017.

- [64] S. Xu *et al.*, “Real-time reliable determination of binding kinetics of DNA hybridization using a multi-channel graphene biosensor,” *Nat. Commun.*, vol. 8, p. 14902, Mar. 2017.
- [65] X. Wang, Z. Hao, T. R. Olsen, W. Zhang, and Q. Lin, “Measurements of aptamer–protein binding kinetics using graphene field-effect transistors,” *Nanoscale*, vol. 11, no. 26, pp. 12573–12581, Jul. 2019.
- [66] Y. Zhu *et al.*, “A graphene-based affinity nanosensor for detection of low-charge and low-molecular-weight molecules,” *Nanoscale*, vol. 8, no. 11, pp. 5815–5819, Mar. 2016.
- [67] Kim, Beom Joon, et al. “High-Performance Flexible Graphene Field Effect Transistors with Ion Gel Gate Dielectrics.” *Nano Letters*, vol. 10, no. 9, 12 Aug. 2010, pp. 3464–3466., doi:10.1021/nl101559n.
- [68] Y. Ohno, K. Maehashi, Y. Yamashiro, K. Matsumoto, *Nano Lett.* 2009, 9, 3318.
- [69] J. Xia, F. Chen, J. Li, N. Tao, *Nat. Nanotechnol.* 2009, 4, 505.
- [70] Armbruster, David A, and Terry Pry. “Limit of Blank, Limit of Detection and Limit of Quantitation.” *The Clinical Biochemist. Reviews*, The Australian Association of Clinical Biochemists, 29 Aug. 2008, www.ncbi.nlm.nih.gov/pmc/articles/PMC2556583/.
- [71] A K Geim 2012 *Phys. Scr.* 2012 014003
- [72] Randviir, Edward P., et al. “A Decade of Graphene Research: Production, Applications and Outlook.” *Materials Today*, vol. 17, no. 9, Nov. 2014, pp. 426–432., doi:10.1016/j.mattod.2014.06.001.
- [73] Bilton, Nick. “Graphene: Strongest & Thinnest Material Known to Exist, May Be the next Wonder Material.” *The Economic Times*, 14 Apr. 2014, economictimes.indiatimes.com/graphene-strongest-thinnest-material-known-to-exist-may-be-the-next-wonder-material/articleshow/33737042.cms?from=mdr.
- [74] Bhuyan, Md. Sajibul, et al. “Synthesis of Graphene.” *International Nano Letters*, vol. 6, no. 2, 9 Feb. 2016, pp. 65–83., doi:10.1007/s40089-015-0176-1.
- [75] S. Mao *et al.*, “Two-dimensional nanomaterial-based field-effect transistors for chemical and biological sensing,” *Chem. Soc. Rev.*, vol. 46, no. 22, pp. 6872–6904, Nov. 2017.
- [76] J. Lin *et al.*, “Gating of single-layer graphene with single-stranded deoxyribonucleic acids,” *Small Weinh. Bergstr. Ger.*, vol. 6, no. 10, pp. 1150–1155, May 2010.
- [77] A. Béraud, M. Sauvage, C. M. Bazán, M. Tie, A. Bencherif, and D. Bouilly, “Graphene field-effect transistors as bioanalytical sensors: design, operation and performance,” *Analyst*, Nov. 2020.

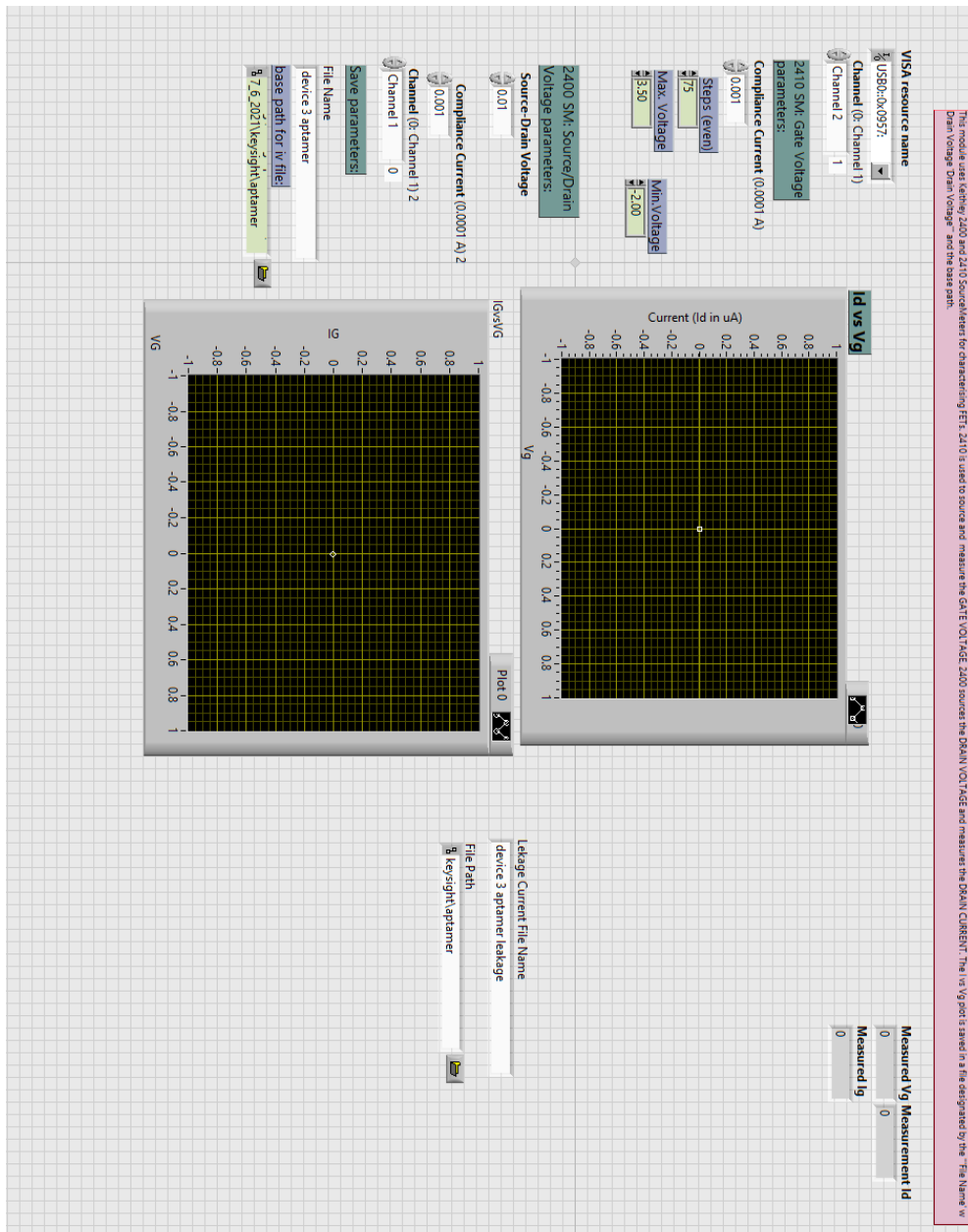
- [78] I. Novodchuk, M. Bajcsy, and M. Yavuz, “Graphene-based field effect transistor biosensors for breast cancer detection: A review on biosensing strategies,” *Carbon*, vol. 172, pp. 431–453, Feb. 2021.
- [80] Bandyopadhyay, M, et al. “Study of Graphene Field Effect Transistor (GFET) for Chemical Sensing Application.” *Journal of Physics: Conference Series*, vol. 1797, no. 1, 2021, p. 012045., doi:10.1088/1742-6596/1797/1/012045.
- [81] Hao, Zhuang, et al. “Graphene-Based Fully Integrated Portable Nanosensing System for on-Line Detection of Cytokine Biomarkers in Saliva.” *Biosensors and Bioelectronics*, vol. 134, 1 June 2019, pp. 16–23., doi:10.1016/j.bios.2019.03.053.
- [82] Hao, Zhuang, et al. “Sensitive Detection of Lung Cancer Biomarkers Using an Aptameric Graphene-Based Nanosensor with Enhanced Stability.” *Biomedical Microdevices*, vol. 21, no. 3, 4 July 2019, doi:10.1007/s10544-019-0409-6.
- [83] Reiner-Rozman, Ciril, et al. “Graphene-Based Liquid-gated Field Effect Transistor for Biosensing: Theory and Experiments.” *Biosensors and Bioelectronics*, vol. 70, 7 Mar. 2015, pp. 21–27., doi:10.1016/j.bios.2015.03.013.
- [84] “Nanosensors: Definition, Applications and How They Work.” *AZoNano.com*, AZoNano, 19 Aug. 2019, www.azonano.com/article.aspx?ArticleID=1840.
- [85] Horowitz, Mark. “Transistor Models.” *Computer Systems*. 2021, Standford, Stanford University.
- [86] Lu, Ganhua, et al. “Semiconducting Graphene: Converting Graphene from Semimetal to Semiconductor.” *Nanoscale*, vol. 5, no. 4, 10 Dec. 2012, p. 1353., doi:10.1039/c2nr32453a.
- [87] Grumezescu, Alexandru Mihai. *Fullerenes, Graphenes and Nanotubes: a Pharmaceutical Approach*. William Andrew, an Imprint of Elsevier, 2018.
- [88] Gianchandani, Yogesh B., et al. *Comprehensive Microsystems*. Elsevier, 2008.

APPENDIX

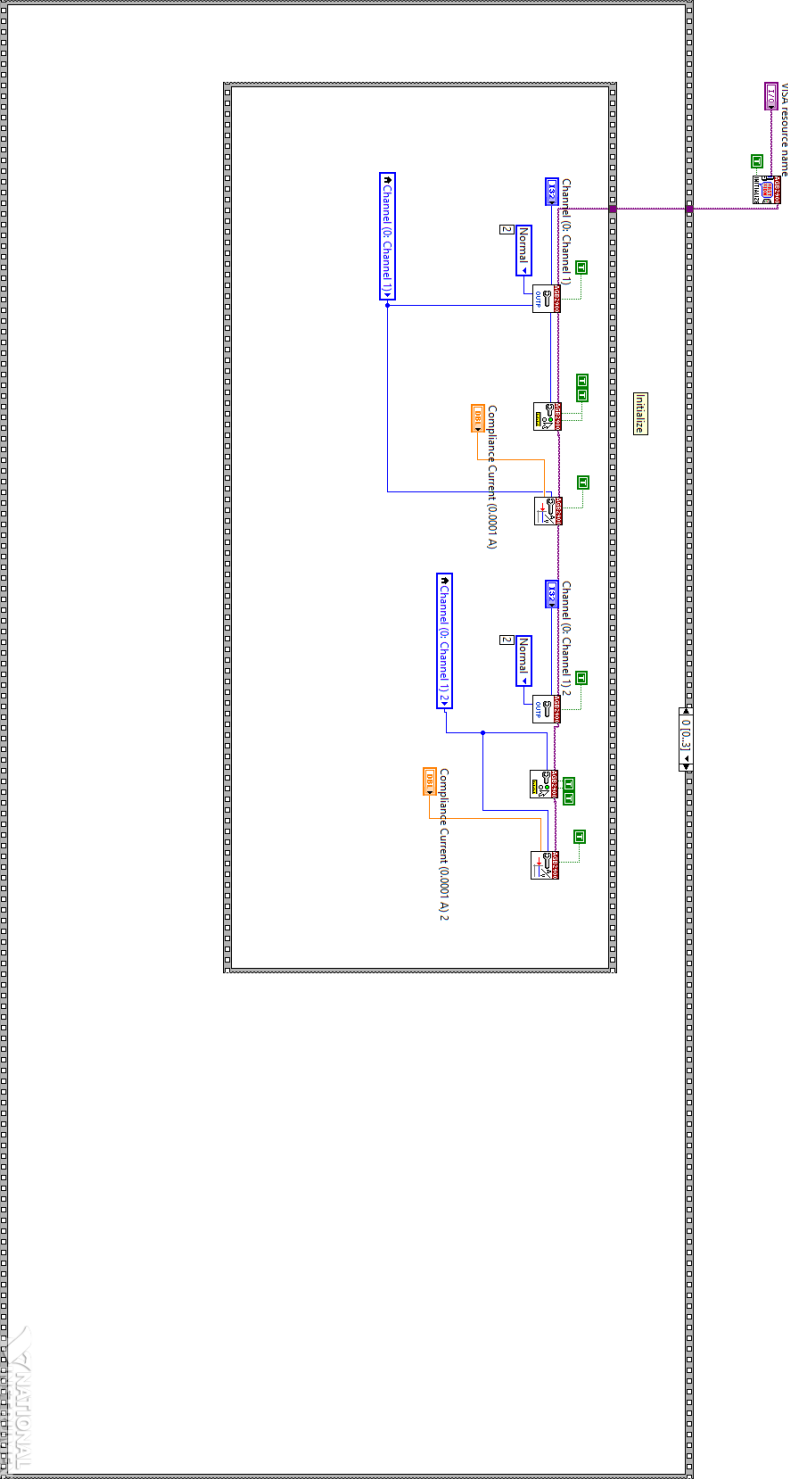
LabVIEW code:

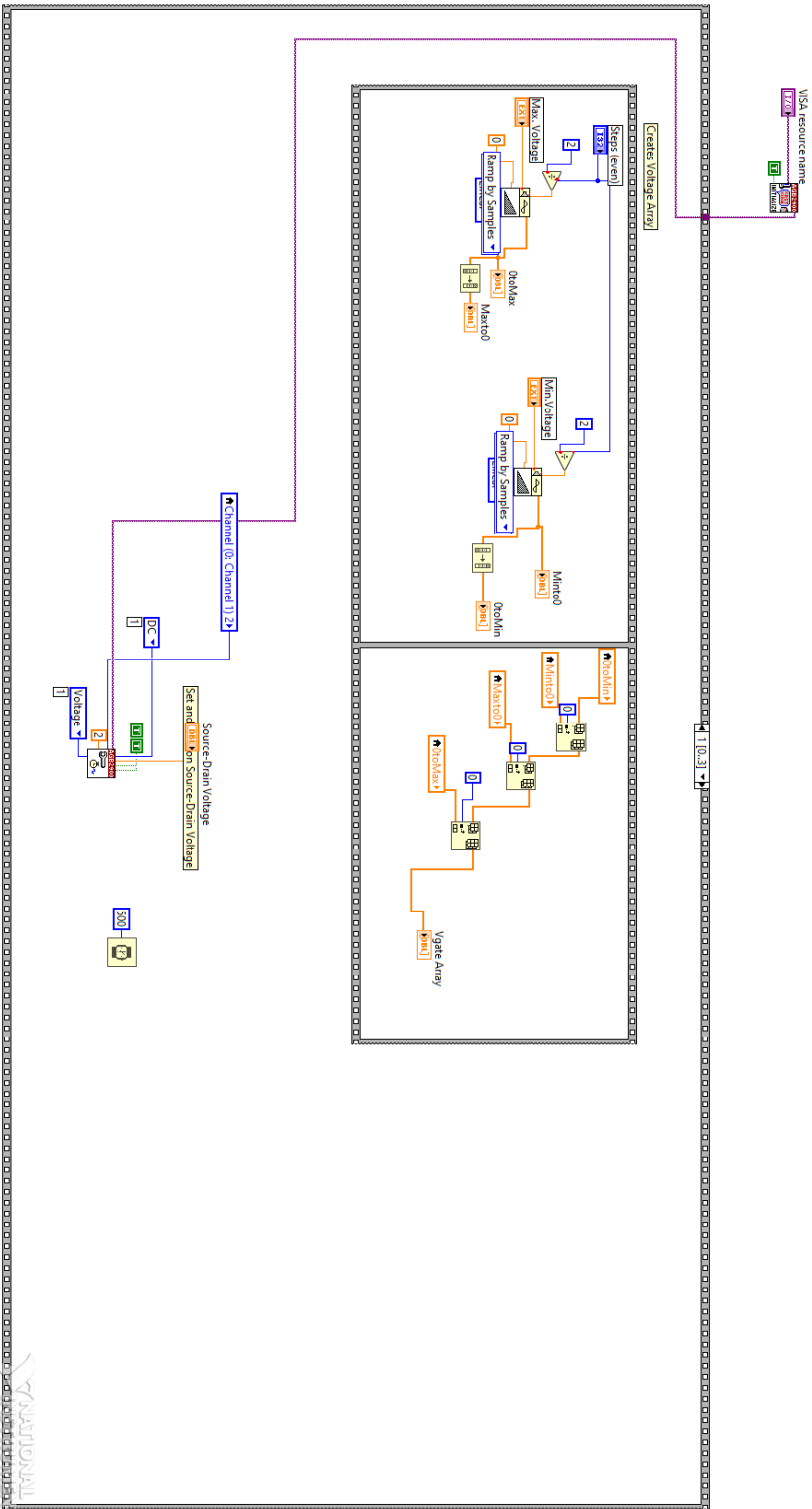
Every LabVIEW code consists of both a front panel and a block diagram.

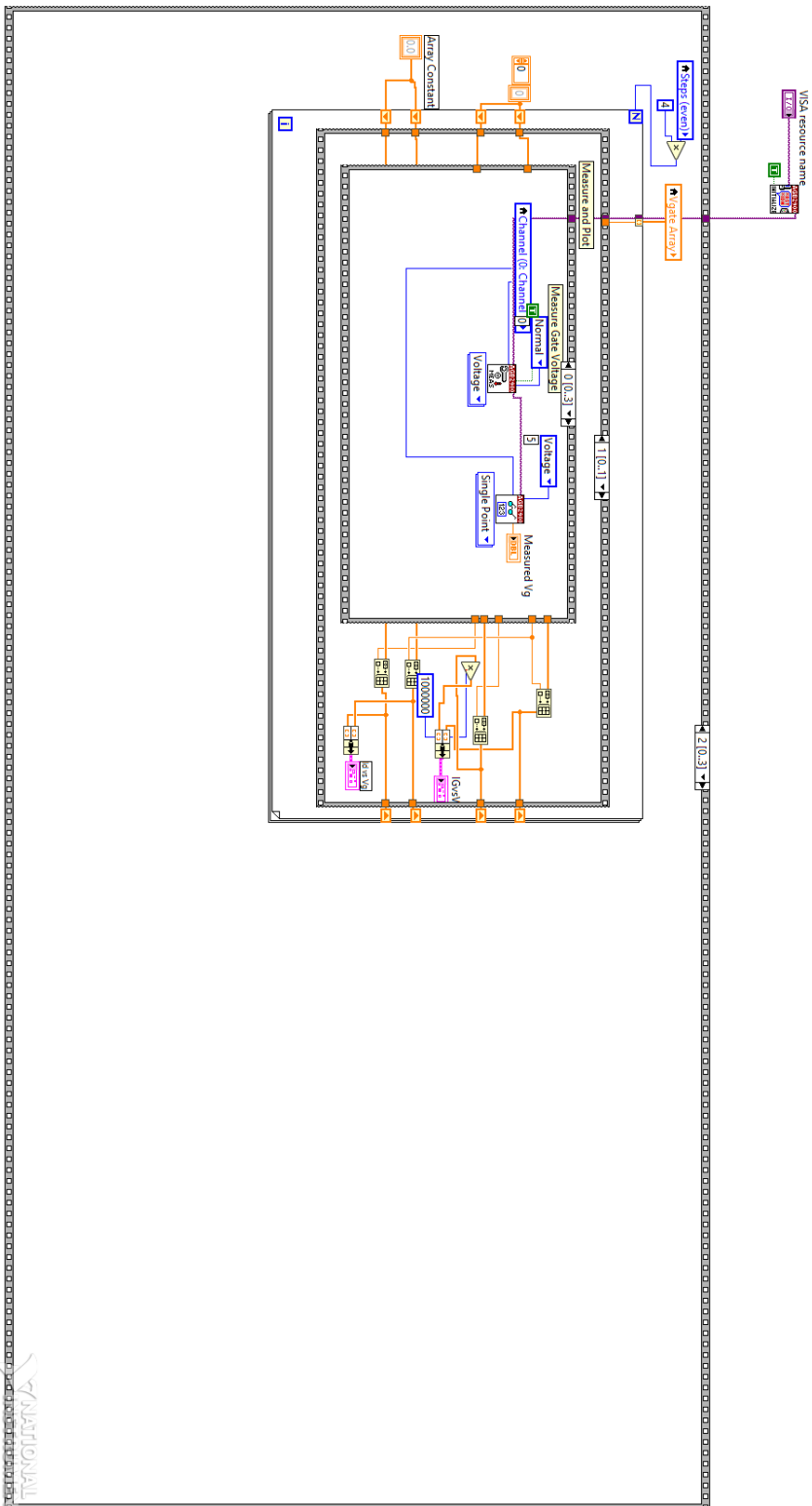
Static sensing file: front panel

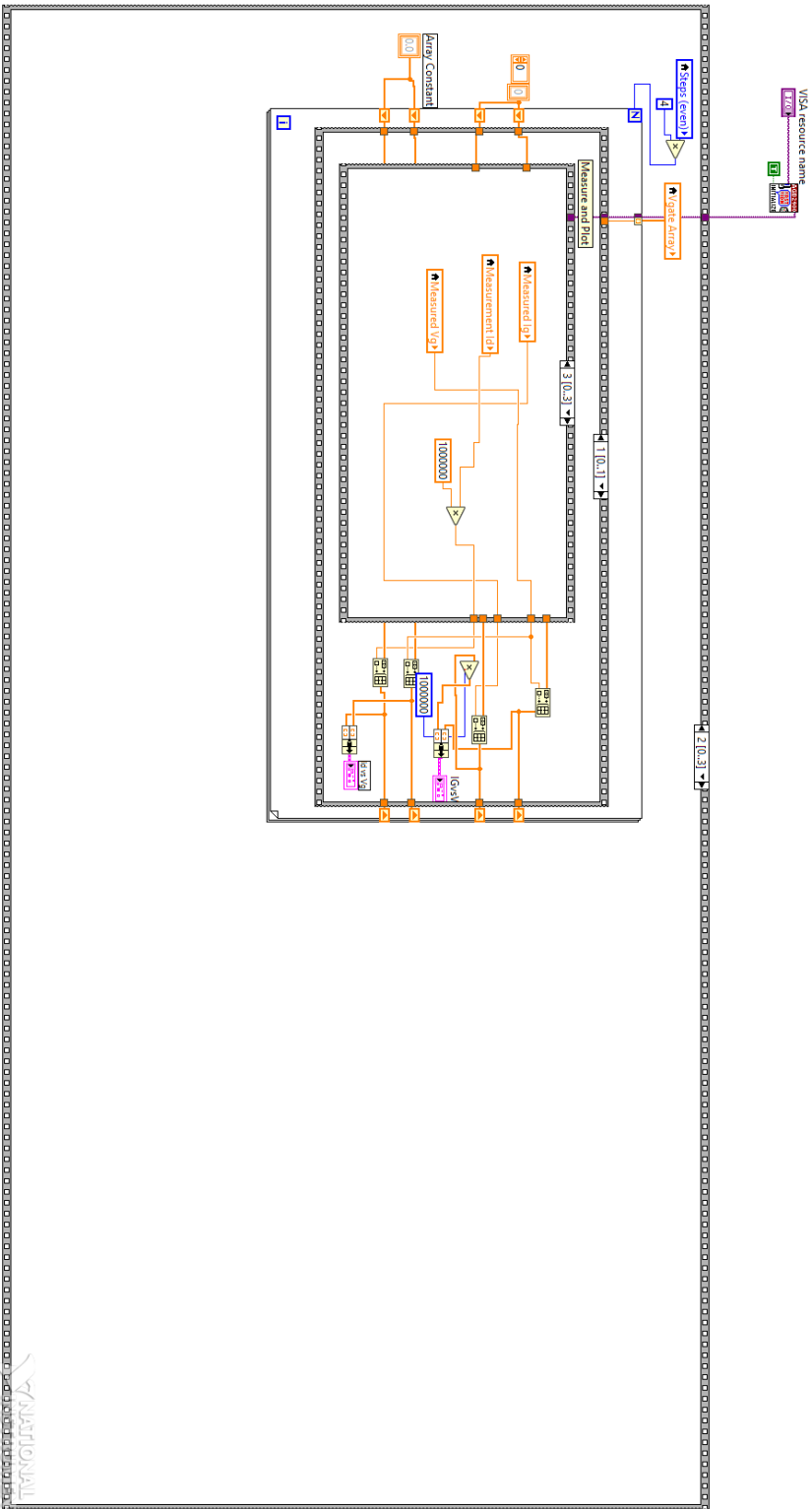


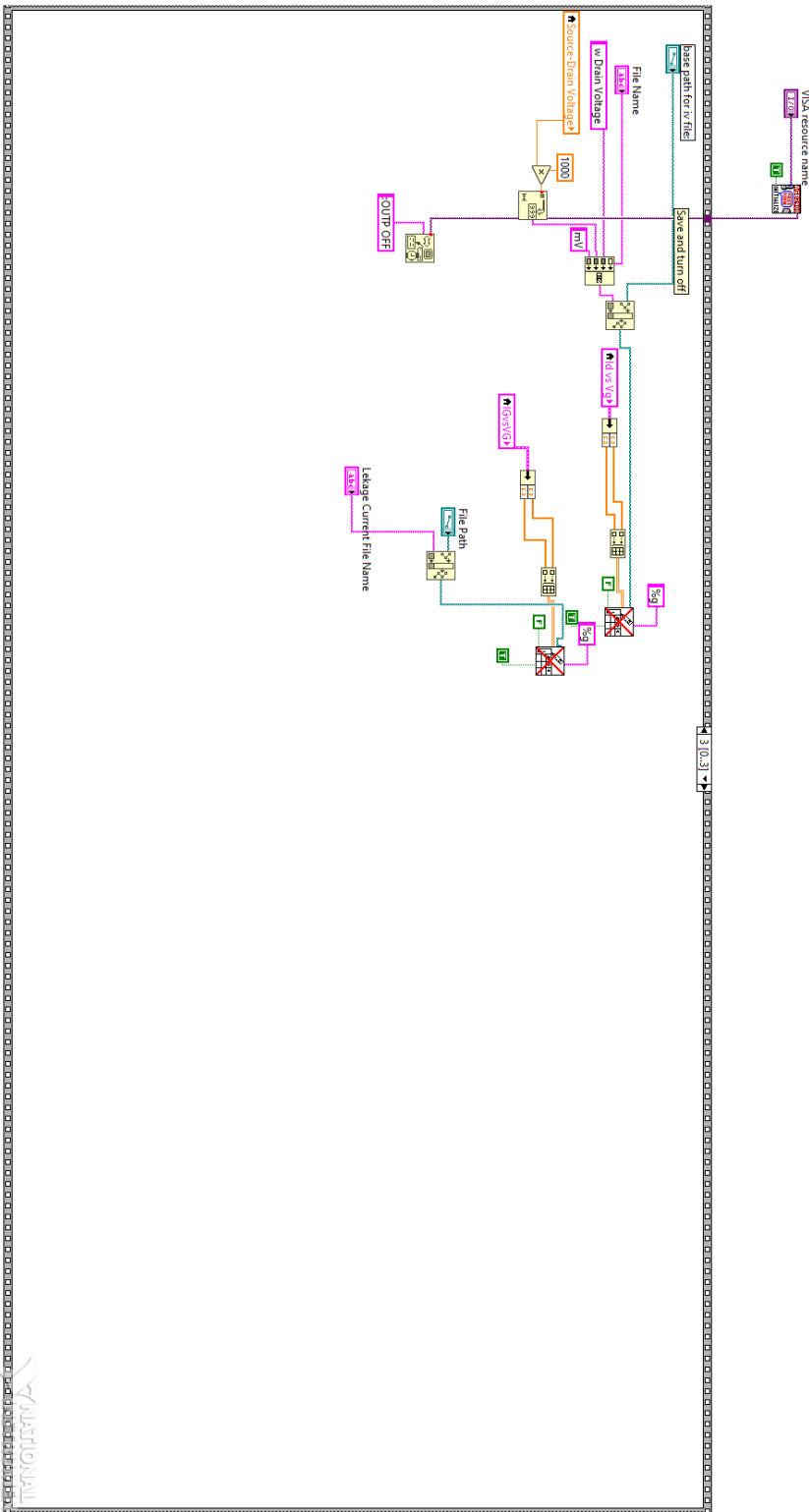
Static sensing file: block diagram



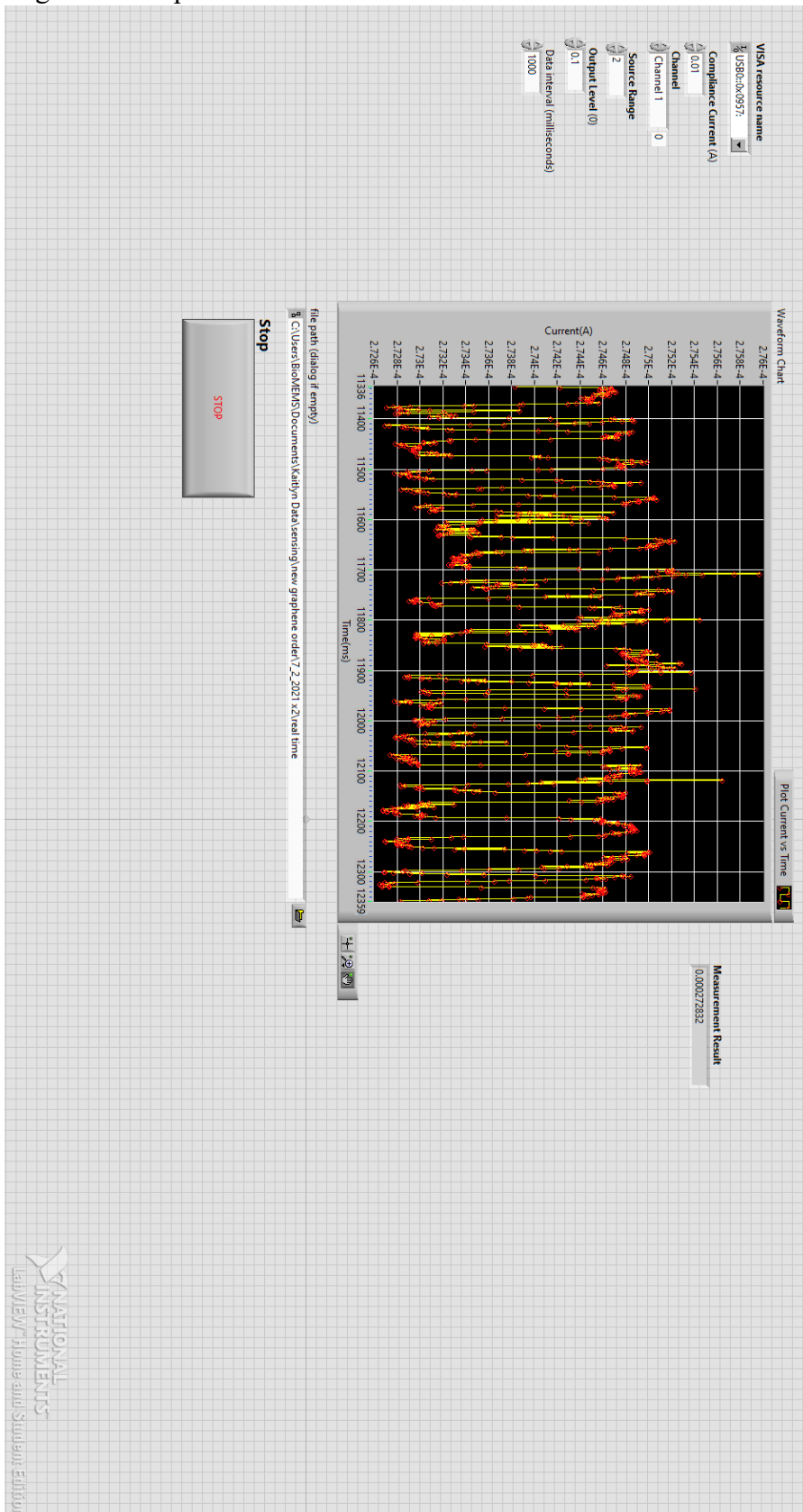




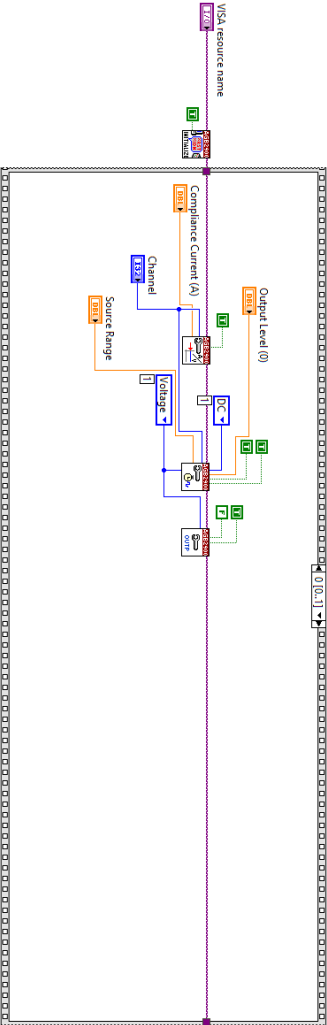


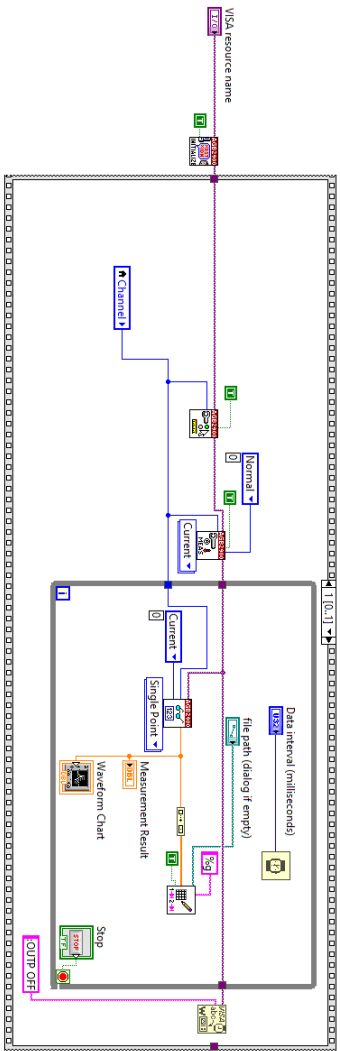


Real-time sensing file: front panel



Real-time sensing file: block diagram





Voltera printing procedure:

Voltera outlines the printing procedure and walks the user simply through each of the steps to print a design. All steps are outlined below and are as follows for this application:

1. Open Voltera software which brings the user to the front page. Select print.
2. Voltera allows for two different printing processes

Simple: Printing design on a blank substrate

Aligned: Printing design on a substrate with existing features

For this application, simple printing is used.

3. Choose the ink which is being used for the application. Currently Voltera only allows selection of Voltera brand inks, however this selection is only used to automatically select the temperature and time of curing at the end of the process. Therefore, other commercially available inks can be used and manually cured at the end using the heat function of the Voltera.
4. Load in the file that is to be printed (from KiCAD).
5. Quality check ensures success during the printing process. This includes making sure that the calibration pad does not have dried ink on it or that the nozzle tip is bent or broken.
6. The substrate is secured into place on the Voltera stage using the provided clamps. In this case, the Kapton substrate is too thin to be securely anchored to the stage using the clamps so a small amount of Kapton tape is used.
7. Mount the probe tip to the Voltera. The Voltera comes with two 'pens' one of which is for the conductive ink and the other which is the probe (green top).
8. Position the circuit to align properly with the secured substrate. The user estimates where the substrate is on the Voltera stage from the software. From there after selecting the 'outline' button, the Voltera probe will hover over the Voltera stage and outline the area where circuit design will

print. If the estimate of the substrate location is accurate then the user proceeds to the next step. If not, the user simply adjusts the positioning on the Voltera software until the probe properly outlines the substrate.

9. After proper positioning, the probe measures the substrate height. This is a critical step as the Voltera print height is not set from the stage height, but rather is set to be relative from the surface of the substrate to be printed on.

10. Priming the conductor consists of the user turning the gear on the top of the conductor until ink begins to come out the nozzle. After the ink comes out, the gear is turned back about a $\frac{1}{4}$ of a turn and then the nozzle is whipped clean and placed onto the Voltera.

11. Calibration of the conductor ensures proper printing during the next step. During calibration, a standard 4 serpentine and 4 straight line pattern is printed. The user watches as this pattern is printed to ensure that the ink is coming out at a proper rate and that the print height is appropriate. If the calibration pattern is not printed properly or to the users liking, it can simply be wiped away and repeated until it is acceptable. This step is encouraged to be repeated as many times as necessary to ensure that the final design only needs to be printed once, thus saving time and materials.

12. Print the pattern using the conductive ink. During this step, the entire design can be printed, or just certain sections making touchups extremely easy.

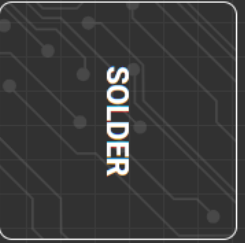
13. Lastly, heating is done in order to cure the ink. If the proper ink is selected during step three, the heating function at the end of the printing process is acceptable to use. If this is not the case, the user can close the printing function and select the heating function from the front page. The heat function has a manual mode which allows for the user to select both the temperature and duration of the ink curing



Connected
25.5°C
X: 0.00 Y: 0.00 Z: 0.00

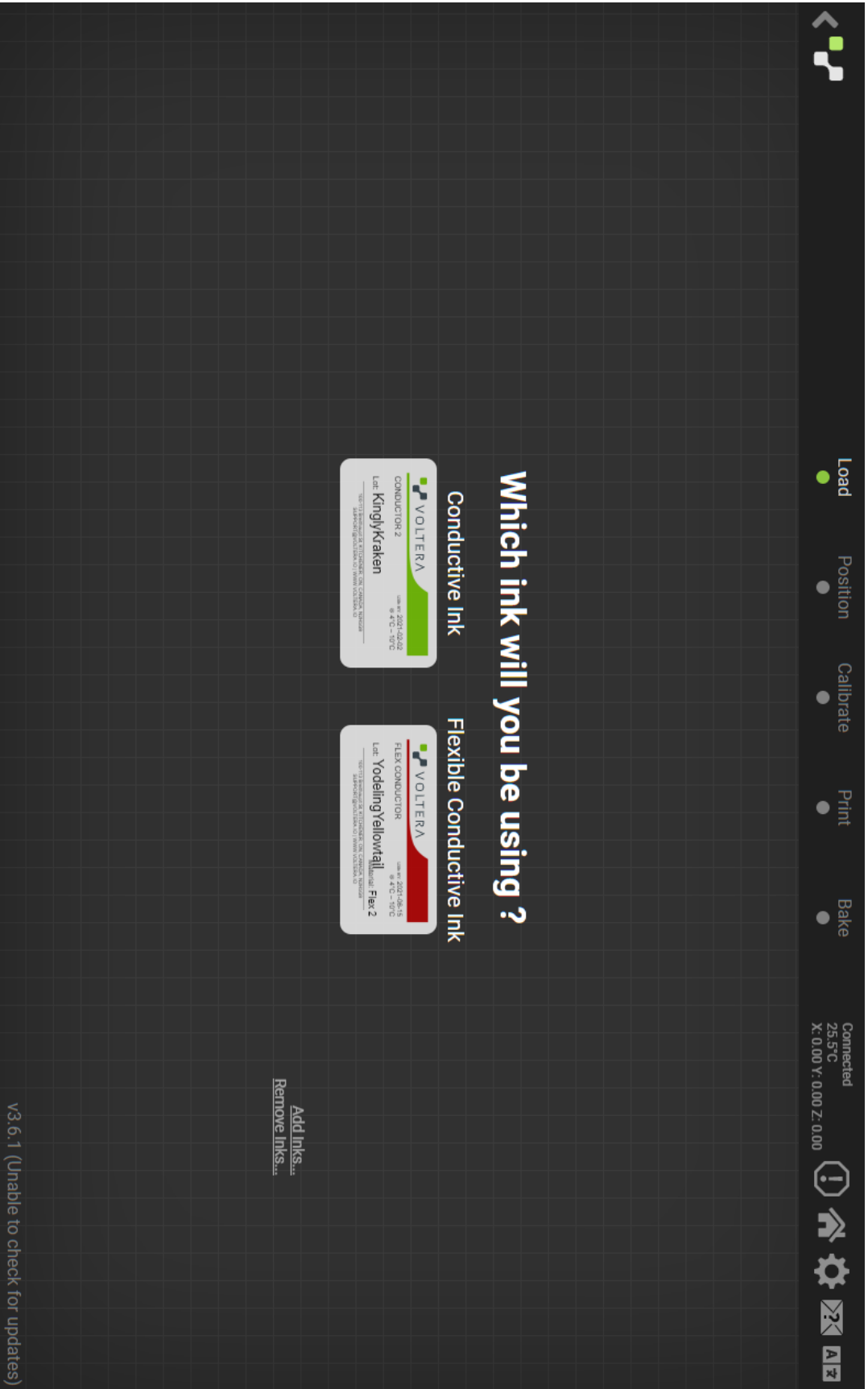


VOLTERA



v3.6.1 (Unable to check for updates)

The screenshot shows a software interface for PCB design. At the top, there is a status bar with several indicators: a green square icon, a 'Load' indicator with a green dot, 'Position', 'Calibrate', 'Print', and 'Bake' indicators with grey dots. On the right side, there is a 'Connected' status with '25.5°C' and coordinates 'X: 0.00 Y: 0.00 Z: 0.00'. Below this are icons for an information symbol, a home icon, a gear (settings), an envelope (mail), and a keyboard icon. The main area features a dark grid background with two large white-bordered boxes. The left box is labeled 'SIMPLE' and is associated with the text 'For blank boards' and a 'Learn More...' link. The right box is labeled 'ALIGNED' and is associated with the text 'Board has existing features' and a 'Learn More...' link. At the bottom left, there is a version and update status: 'v3.6.1 (Unable to check for updates)'.



YodelingYellowtail

Load

Position

Calibrate

Print

Bake

Connected
25.5°C
X: 0.00 Y: 0.00 Z: 0.00

BACK

NEXT

Load Circuit

Select your Gerber files below or get started with the [Hello World tutorial](#)

LOAD LAST CIRCUIT

Ink: GFET_design_lm350_dis250
flare_top_extended_electrodes
wider_pads_F_Cu.gbr

Holes: Choose File...

lm350 dis250

v3.6.1 (Unable to check for updates)

YodelingYellowtail

Load ●

Position ●

Calibrate ●

Print ●

Bake ●

Connected
 25.5°C
 X: 0.00 Y: 0.00 Z: 0.00

◀ BACK
NEXT ▶

Quality Checklist

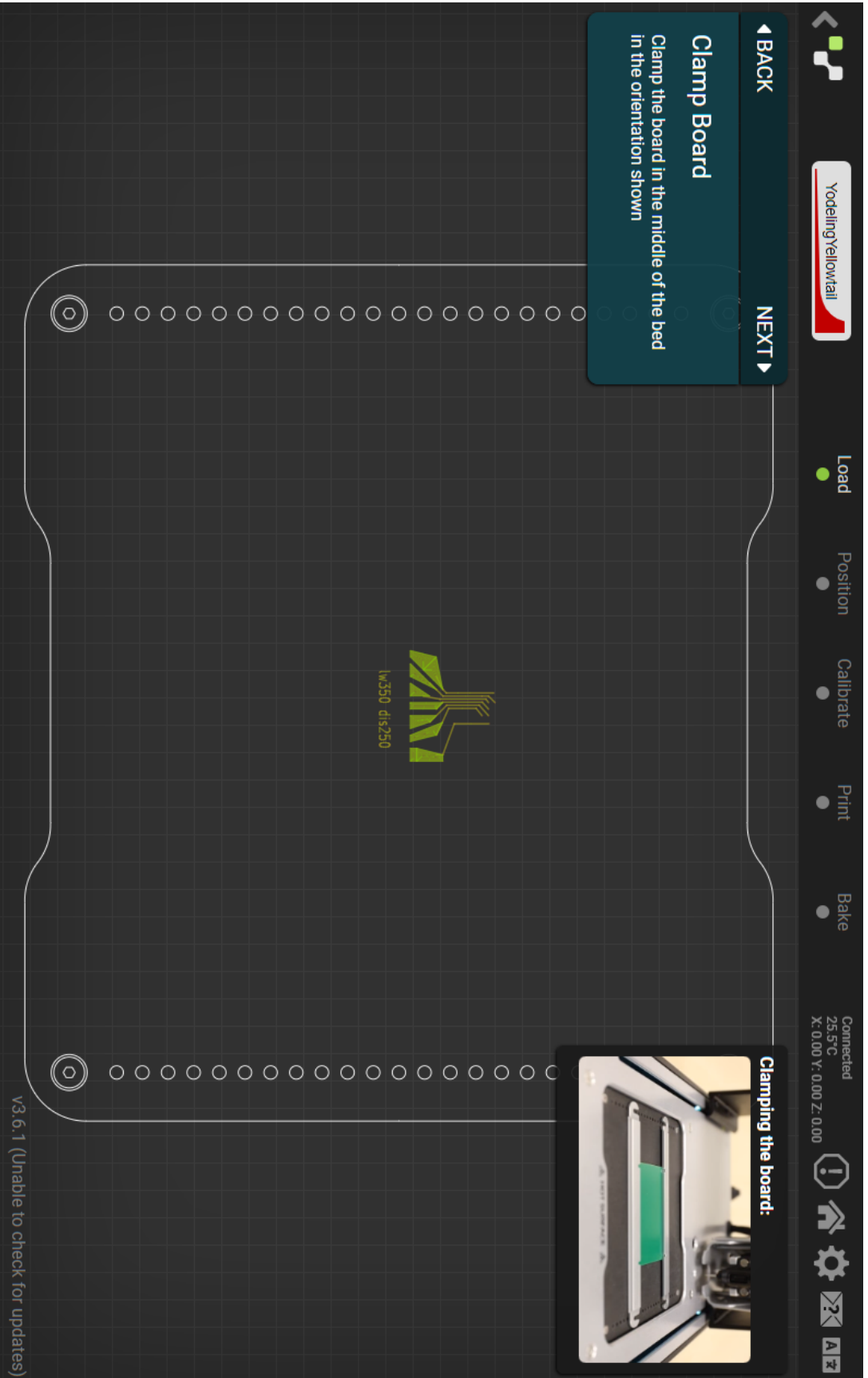
Ensure that:

- Calibration switches are clean
- Ink has been allowed to warm to room temperature for 15 minutes
- Dispenser nozzle is not damaged

Cleaning calibration switches:

Inspecting nozzle:

v3.6.1 (Unable to check for updates)



YodelingYellowtail

Load Position

Calibrate Print Bake

Connected
25.5°C
X: 0.00 Y: 0.00 Z: 0.00

Mount Probe
Mount the probe on the printer carriage

BACK NEXT

lv350 dis250

Mounting the probe:
Ensure the pins make contact

v3.6.1 (Unable to check for updates)

YodelingYellowtail

Load Position Calibrate Print Bake

Connected
25.5°C
X: 0.00 Y: 0.00 Z: 0.00

Outlining the board:
[Learn More...](#)

Position Circuit

Click and drag the on-screen circuit to match the location of the clamped board

Click **Outline (Alt+O)** to show where the circuit will be printed

OUTLINE

v3.6.1 (Unable to check for updates)

YodelingYellowtail

Load

Position

Calibrate

Print

Bake

Connected
25.5°C
X: 0.00 Y: 0.00 Z: 0.00

BACK

Measure Height

Click Probe to measure the surface height

PROBE

NEXT

V3.6.1 (Unable to check for updates)



YodelingYellowtail

Load

Position

Calibrate

Print

Bake

Connected
25.5°C
X: 0.00 Y: 0.00 Z: 11.26



◀ BACK

Prime Conductor

Prime the conductive ink dispenser

1. Turn the gear **counter-clockwise** slowly until ink barely comes out
 2. Confirm ink is coming out
 3. Turn the gear **clockwise** 1/4 turn
 4. Gently wipe the nozzle tip
- ⚠ Ink must stop leaking after step 3.**

NEXT ▶



Priming the dispenser:

[Learn More...](#)

v3.6.1 (Unable to check for updates)

YodelingYellowtail

Load

Position

Calibrate

Print

Bake

Connected
 25.5°C
 X: 0.00 Y: 0.00 Z: 11.26

◀ BACK
NEXT ▶

Calibrate Conductor

1. Click **Calibrate**
2. Use **-** and **+** to adjust ink flow while printing
3. **Wipe board**, and repeat calibration until the printed horizontal lines **do not overlap**

Click **Calibrate** to begin

Z: 0.01mm

-

+

CALIBRATE

Advanced...

Learn More...

Selected
 Not Selected

v3.6.1 (Unable to check for updates)

YodelingYellowtail

Connected
25.5°C
X: 0.00 Y: 0.00 Z: 12.72

Load

Position

Calibrate

Print

Bake

ⓘ

🏠

⚙️

📧

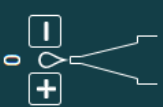
🔍

◀ BACK

Print Conductive

Click **Start** to begin


Z: 0.01mm



START

Advanced...

NEXT ▶



lv350 dis250

ⓘ

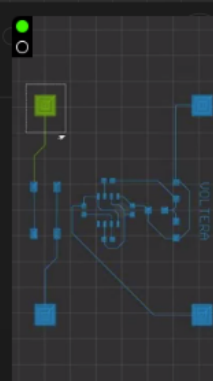
🏠

⚙️

📧

🔍

You can re-print a portion of the circuit



Use Shift or Ctrl to tune your selection

[Learn More...](#)

ⓘ

🏠

⚙️

📧

🔍

Selected

Not Selected

v3.6.1 (Unable to check for updates)



YodelingYellowtail

Load

Position

Calibrate

Print

Bake

Connected
 25.5°C
 X: 0.00 Y: 0.00 Z: 12.72



◀ BACK

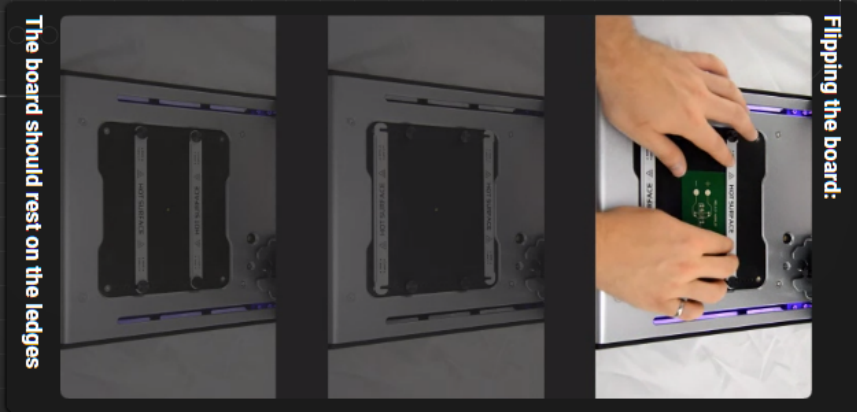
Flip Board

⚠ Ink is wet, handle with care!

Flip the board so it rests on the baking ledges:

1. Loosen the screws and remove all boards
2. Swap the clamps and slide them under the screws
3. Place the board on the clamp ledges
4. Squeeze the clamps together and tighten them
5. Flip the board. Place it on the baking ledges

NEXT ▶



v3.6.1 (Unable to check for updates)